The MicroBooNE Single-Photon Low-Energy Excess Search Public Note 1087

The MicroBooNE Collaboration

June 30, 2020

Abstract

MicroBooNE is a short baseline neutrino experiment at Fermilab designed to address the low energy excess observed by the MiniBooNE experiment. This note describes and presents preliminary results for the MicroBooNE analysis developed to address this excess as a single photon plus one or zero protons in the final state. The analysis assumes neutrino neutral current Δ resonance production followed by Δ radiative decay on argon (NC $\Delta \to N\gamma$) as the "signal model"; event reconstruction and selection have been developed and optimized in order to maximize efficiency and reduce cosmogenic and other beam-related backgrounds to the NC $\Delta \to N\gamma$ signal. We present the analysis methodology and validation checks performed on limited-statistics open data sets, corresponding to 5×10^{19} protons on target (POT), following a blind analysis, as well as the projected sensitivities for testing the Standard Model (SM) predicted rate for the NC $\Delta \to N\gamma$ process and for testing the interpretation of the previously observed MiniBooNE low energy excess as NC $\Delta \to N\gamma$ events, using the full anticipated MicroBooNE data set of 12.25×10^{20} POT.

Contents

1 Introduction

The MiniBooNE experiment reported its first observation of an anomalous excess of "low-energy" ν_e charged current quasi-elastic (CCQE)-like events in 2008 [1]. Since then, additional data collected by the MiniBooNE collaboration in both neutrino and antineutrino running mode have revealed an increasing (in significance) discrepancy between data and the null hypothesis prediction, over the range of 200-475 MeV in neutrino energy reconstructed assuming ν_e CCQE scattering. Despite becoming more significant with more data and improved analysis, the observed excess has not been definitively attributed to sterile neutrino oscillations or any other interpretation. One of the still-viable interpretations for this excess is that it is contributed by neutral current (NC) single-photon production in neutrino scattering on carbon, where events are generally reconstructed at lower energies and in MiniBooNE contribute as irreducible background. Such process can be either a Standard Model (SM) process that may have been mis-estimated (underestimated) in the MiniBooNE analysis, or a new process involving exotic physics.

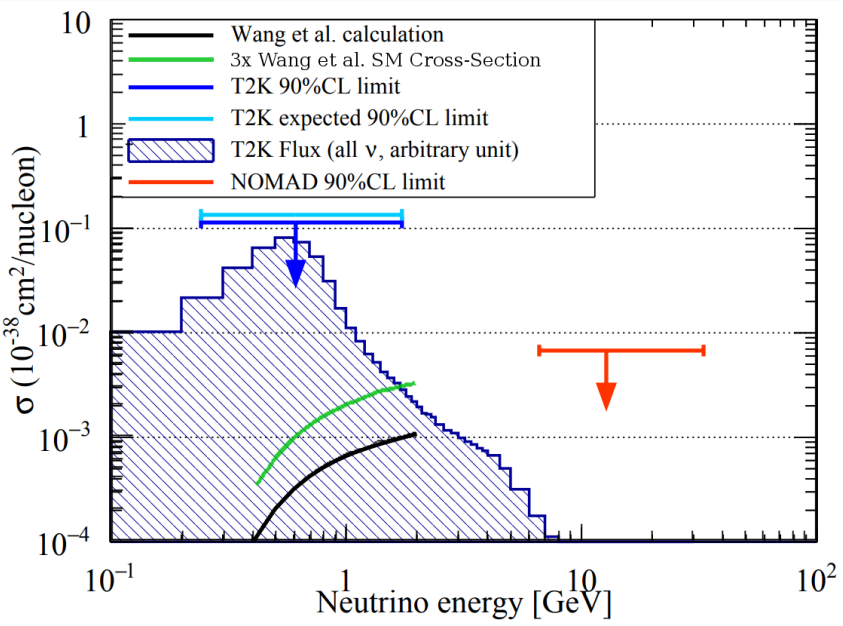

Figure 1: *The current world's best bound on the NC Δ radiative cross-section at O(1GeV) energy by T2K [2]. Shown also in green is the Wang et al. Standard Model (SM) cross-section scaled up by a factor of 3, which is what would be needed to explain the observed MiniBooNE low-energy excess [3].*

The analysis presented in this note aims to test the single-photon interpretation of the MiniBooNE low-energy excess under the explicit hypothesis that the excess is contributed by the SM process of NC Δ baryon resonance production, followed by Δ radiative decay (NC $\Delta \rightarrow N\gamma$, where N is a nucleon). MiniBooNE considered contributions from this process to their background prediction, and constrained the overall background rate by tying its branching fraction to the more dominant π^0 decay mode of the Δ, which was measured in MiniBooNE *in situ*. However, as the rate of the NC Δ resonance production followed by radiative decay has never been directly measured in neutrino scattering, there is motivation to explicitly test this hypothesis with a dedicated MicroBooNE search. Current limits on this process from the T2K experiment [2] only constrain its rate to the level of <100 times the SM prediction at 90% confidence level (CL), as shown in Fig. 1, while a factor of three (3) enhancement of the predicted SM rate can account for the observed MiniBooNE excess [3]. For reference, the uncertainty on the NC Δ radiative decay rate in the MiniBooNE analysis was 12.5% [4], constrained by an in situ measurement of the NC π^0 rate.

1.1 The MicroBooNE Detector

MicroBooNE is sitting in the same neutrino beam as MiniBooNE, the Fermilab Booster Neutrino Beam (BNB), and is a liquid argon time projection chamber (LArTPC) [5] combining the advantages of high spatial resolution of neutrino interactions, as well as excellent calorimetry, leading to strong particle identification capabilities. The detector consists of a 2.56m $\times$ 2.32m $\times$ 10.36m TPC filled with 85 tones liquid argon (active mass) serving as both the bulk target mass and for charge detection, and an array of 32 photomultiplier tubes (PMTs) [6] that detect scintillation light for triggering, timing, and reconstruction purposes.

Ionization charge deposited in the liquid argon volume is drifted horizontally by a large -70 kV drift voltage, corresponding to a drift field of 273 V/cm. At the edge of the TPC, on the anode side, are three sets of wire planes which are used to read out for reconstruction purposes [7].

Broadly, objects in LArTPC's can be split into two categories, "tracks" in which the reconstructed ionization charge forms continuously connected lines, most often due to underlying muons, charged pions and protons; and "showers" in which an electromagnetic cascade is formed from an electron or photon undergoing a cascade of bremsstrahlung, pair production, annihilation and Compton scattering.

For a more detailed description of the MicroBooNE detector, see Ref. [5].

2 Analysis Overview

This analysis builds and significantly expands upon past efforts [8, 9] to develop an efficient and pure selection of events with a topology consistent with neutrino-induced NC $\Delta \rightarrow N\gamma$ events. Two primary final-state-based topologies are examined: one with a single photon and a single proton in the final state and no other tracks or showers reconstructed as part of the interaction ($1\gamma 1p$), and one with a single photon and zero protons in the final state and no other tracks or showers reconstructed as part of the interaction ($1\gamma 0p$). These samples are isolated using reconstruction utilizing the Pandora multi-algorithm approach to automated pattern recognition [10]. The selection methodology and preliminary results, following a blind analysis, are presented in Sec. 3. Throughout the development of this selection, it has consistently been observed that the largest background (at final selection stage) is that of NC π^0 events, where one of the two daughter photons of the π^0 is not reconstructed as such due to (a) leaving the detector, (b) overlapping with the primary shower, (c) pair-converting a significant distance away and thus failing to be associated with the primary neutrino interaction, or (d) failing to reconstruct due to it having too low energy. To make sure that these crucial backgrounds are well understood, two separate (and mutually exclusive) π^0 rich selections are developed. One targeting one proton and two photons and no other tracks/showers ($2\gamma 1p$), and one targeting zero proton and two photons and no other tracks/showers ($2\gamma 0p$). These are discussed in Sec. 4. The NC π^0-targeting selections provide high-statistics samples for data to Monte Carlo comparisons without compromising our signal blindness criteria, which are useful for validating the analysis (including simulation, reconstruction, and event selection), and for directly constraining the rate and potentially shape of the NC π^0 background distribution to the single photon selection.

Final fits to a potential NC $\Delta \rightarrow N\gamma$ signal are performed with a simultaneous fit to all four selections, considering statistical and systematic uncertainties and systematic correlations, as described in Sec. 6. Systematic uncertainties and correlations are evaluated as described in Sec. 5.

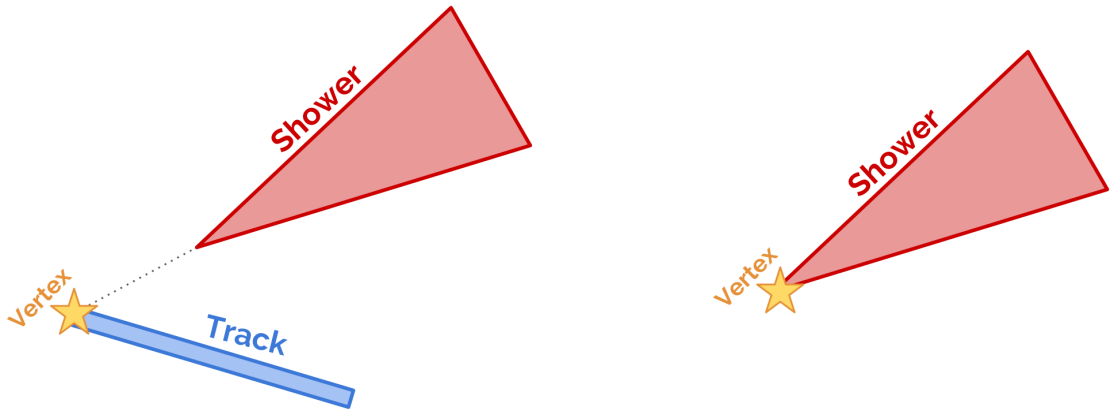

Figure 2: *Cartoon illustrations of the two topological signatures of NC $\Delta \rightarrow N\gamma$ events targeted by the single-photon low-energy excess search. Left: $1\gamma 1p$; right: $1\gamma 0p$. A simulated example of what the $1\gamma 1p$ topology looks like in a LArTPC readout wire plane image is shown in Fig. 3.*

3 Single Photon Selection

3.1 Topological selection and pre-selection

NC Δ radiative selection begins with Pandora-reconstructed information. Specifically, per MicroBooNE recorded event, a candidate neutrino interaction vertex is selected and reconstructed by the Pandora algorithms. Both the $1\gamma 1p$ and $1\gamma 0p$ selections specifically focus on reconstructed vertices which match the corresponding signal topology definitions. These topological selections are defined as:

- $1\gamma 1p$ - requiring exactly one reconstructed shower and one reconstructed track associated to the candidate vertex;
- $1\gamma 0p$ - requiring exactly one reconstructed shower associated to the candidate vertex.

Cartoon representations of what these topologies look like are shown in Fig. 2. An event display showing a Monte Carlo simulation of a $1\gamma 1p$ event with a clear proton track and photon shower in the MicroBooNE LArTPC is provided in Fig. 3. In this standard event display, color indicates the amount of charge detected as a function of collection plane wire number (equivalent to distance along the beam direction) on the horizontal axis and time (equivalent to beam-transverse horizontal distance) on the vertical axis.

Topological selection efficiencies for signal are provided in Tab. 1. For the purposes of comparing how the $1\gamma 1p$ and $1\gamma 0p$ selections change as we step through the analysis, two representative distributions have been chosen to highlight at each stage. For the $1\gamma 1p$, where we have reconstructed both a proton and photon candidate of the Δ baryon decay, we show the reconstructed invariant mass of the parent Δ which for true NC Δ radiative events should be centered on the Δ mass of 1,232 MeV. In the case of $1\gamma 0p$, however, we have no reconstructed information of the escaping neutron and only have access to the photon candidate, so we instead plot the selected photon's reconstructed calorimetric energy. These two distributions, after topological selection, are shown in Fig. 4 for the $1\gamma 1p$ (left) and $1\gamma 0p$ (right) selection. The distributions compare Run 1 unblinded data to simulated predictions. The Run 1 dataset corresponds to approximately 5×10^{20} POT, or $< 5\%$ of the total MicroBooNE data set for Runs 1-5, although after data-quality cuts the available POT that we compare on subsequent plots is closer to 4.1×10^{20} POT. The simulated predictions are broken down according to truth information; the corresponding number of events in the simulation, normalized to the data POT in each distribution, is shown in the legend.

As we utilize the same plotting style and legends as is in Fig. 4 for all comparisons between data and simulation in this note, we here briefly describe the breakdown of the various categories. Data points are shown in black, corresponding to the total POT exposure as described on the plot. The remaining histograms are stacked on top of each other and make up the total simulated expectation normalized to the same exposure. Our signal that we search for is the NC Δ radiative decay, and is included both as the standard model expected rate in GENIE as well as an additional factor of 2 enhancement, which would be needed to explain the MiniBooNE LEE. The various categories including NC 1 π^0 Coherent, NC π^0 Non-Coherent, NC 2+ π^0, CC ν_μ π^0 and CC $\nu_e/\overline{\nu}_e$ intrinsic all represent particular sub-components of the total BNB interactions in the MicroBooNE cryostat that we highlight explicitly as they are particularly important backgrounds for this search. All remaining BNB interactions within the cryostat that do not fit into the above 6 definitions are grouped together and referred to as "BNB Other", the majority of which are CC ν_μ events with no exiting π^0. The Dirt category represents all BNB neutrino induced backgrounds that originate outside the cryostat (in the surrounding concrete, steel and dirt) but scatter inside the TPC and produce reconstructable charge. The final histogram is the cosmogenic backgrounds, labeled "cosmic data", as they are explicitly extracted from MicroBooNE data measured in situ during running, but out of time with the BNB neutrino spills. Simulation error bars include flux and cross-section systematic uncertainty as well as inherent Monte-Carlo statistical uncertainty, with the error bars on the data being their corresponding Poisson errors. Although detector systematics have been evaluated for the purposes of the final sensitivities (see Sec. 5), unless mentioned directly they are omitted from distributions.

After topological selection, a series of pre-selection cuts are applied in order to reduce both any obvious and clear backgrounds as well as the number of selected events with reconstruction failures. For the $1\gamma 1p$ topology, the pre-selection cuts include:

- **Shower Energy Cut:** The reconstructed calorimetric shower energy must be at least 40 MeV.
- **Track Mean dE/dx Cut:** The "truncated mean dE/dx" of the track must be above 2 MeV/cm. The truncated mean is an average of dE/dx along the track, truncating values further than 1 sigma away from a rolling mean, reducing the effects of spurious outliers.
- **Angle between Track and Shower Cut:** The absolute value of the cosine of the angle formed from the track direction and shower direction must be < 0.99. The shower direction is taken to be the direction from the reconstructed vertex to the reconstructed shower start point.

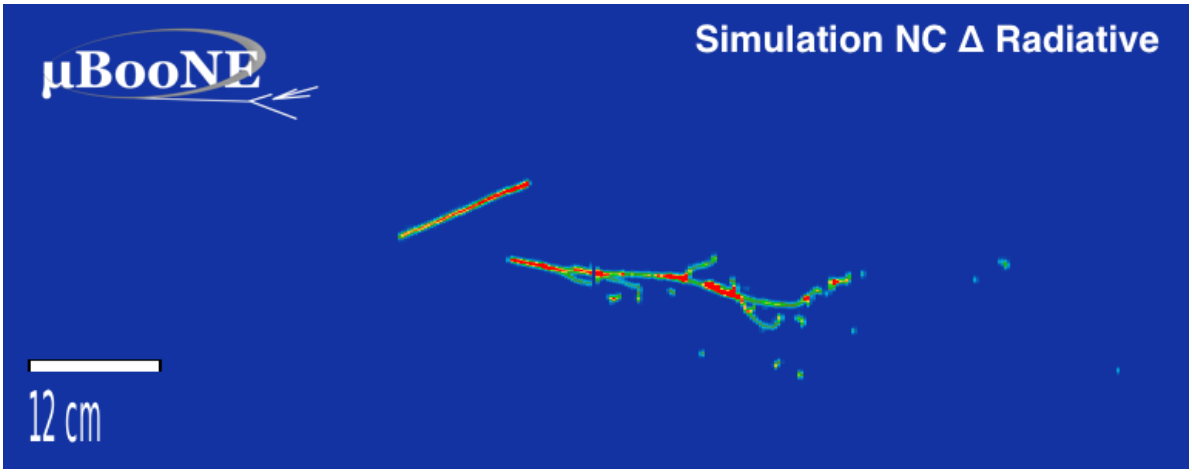

Figure 3: *A example simulated $\Delta^+ \to p\gamma$ event, showing a short proton track with Bragg peak, as well as non-zero conversion distance of the photon before pair-producing into an e^+e^- pair that subsequently forms an electromagnetic shower in the liquid argon. This event represents a classic example of the topology we are searching for with the $1\gamma 1p$ selection.*

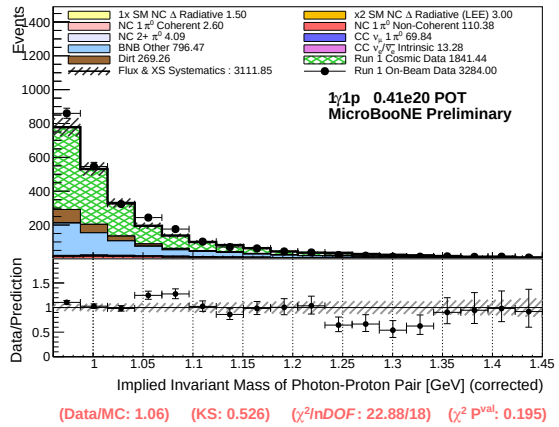

(a) $1\gamma 1p$ *Selection at Topological Stage*

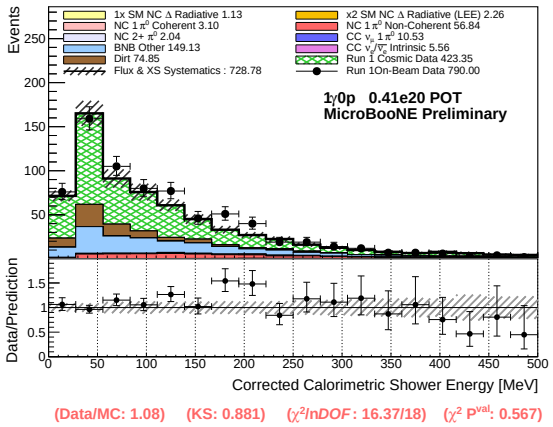

(b) $1\gamma 0p$ *Selection at Topological Stage*

Figure 4: $1\gamma 1p$ *and* $1\gamma 0p$ *Monte Carlo predicted distributions after the topological selection stage. Predictions are scaled to and compared to the open Run 1 data set corresponding to* 4.1×10^{19} *POT. Here, the dominant backgrounds are cosmogenic backgrounds, in green (labeled "cosmic data", as they are directly extracted from MicroBooNE data measured in situ when the BNB is off), followed by "BNB other" and dirt induced backgrounds, in light blue. Overall, reasonable data to Monte Carlo agreement is observed, within statistical and systematic uncertainties. Note: detector systematic uncertainties have been evaluated but are omitted in these distributions.*

- **Shower Fiducial Volume Cut:** The reconstructed shower start must be 7 cm from the wire cell space charge boundary. The "wire cell space charge boundary" (SCB) represents the effective active TPC volume [11].
- **Track Calorimetric Energy Cut:** The calorimetric kinetic energy (KE) of the track, estimated based on the track's deposited energy, must be < 400 MeV. This forms a consistency check with the previous length-based cut.
- **Track Containment Cut:** The reconstructed track start and end must both be at least 2 cm from the SCB.
- **Vertex Fiducial Volume Cut:** The reconstructed vertex must be at least 2 cm from the SCB.
- **Track Length-Based Energy Cut:** The reconstructed KE of the track, estimated based on the length of its travel path in argon under the hypothesis that the track is a proton, must be < 500 MeV.

The signal efficiency of these cuts is shown in Tab. 2 (quoted specifically for "well-reconstructed" signal events in which the reconstructed shower and track were correctly matched to the true photon and proton in the interaction). Shown also are the efficiencies for two of our primary backgrounds: (1) mis-identified cosmogenic backgrounds, which are extracted directly from MicroBooNE data taken out-of-time with the BNB spills during Run 1[1], and (2) mis-identified NC $1\pi^0$ events. This demonstrates the significant background reduction achieved with these cuts. Figure 5 shows the effect of these cuts on the signal spectra (red) as well as the measured cosmogenic background spectra (green) and other BNB background spectra (blue). The resulting $1\gamma 1p$ distribution, following pre-selection, is provided in Fig. 6, left.

In parallel to the $1\gamma 1p$ pre-selection, the following cuts are applied for the $1\gamma 0p$ pre-selection:

- **Fiducial Volume Cut:** The reconstructed shower start must be at least 2cm from the SCB.

[1]These are also often referred to as BNB-external data.

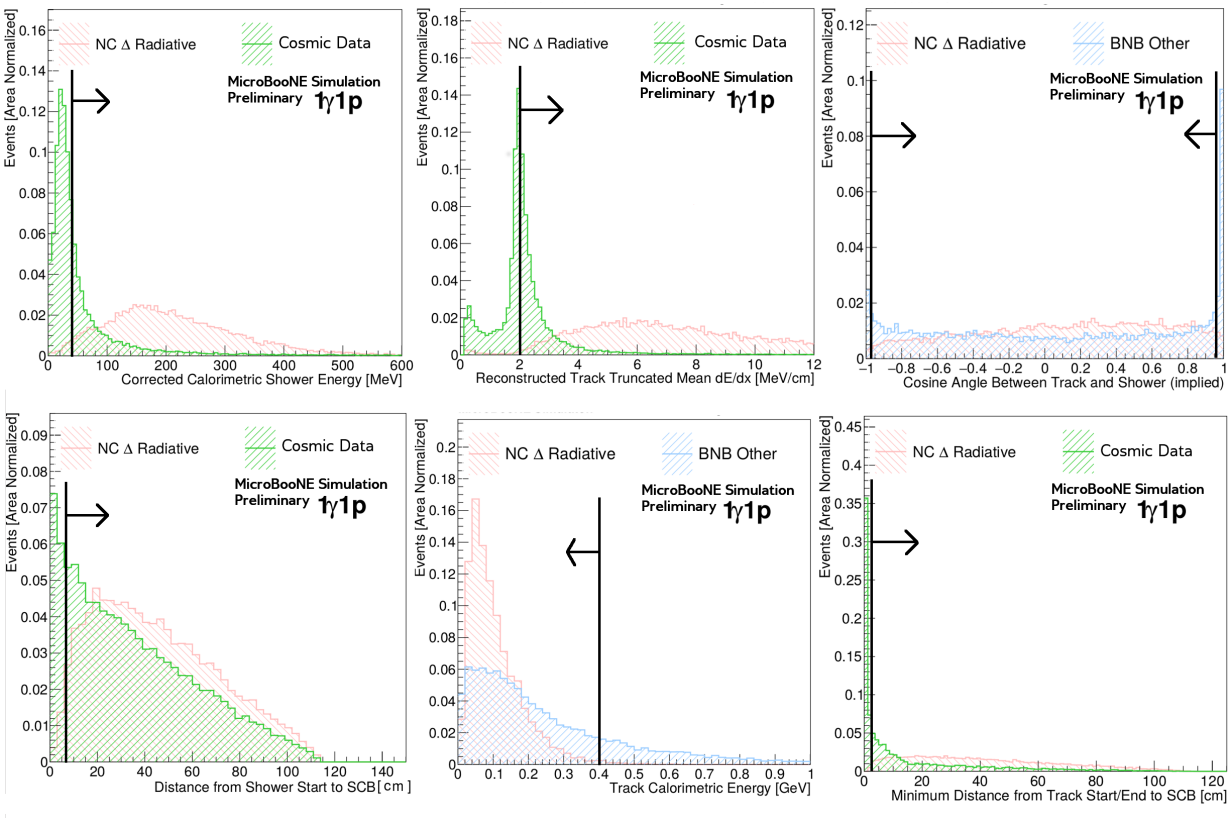

Figure 5: *The positions of 6 of the primary precuts used in the $1\gamma1p$ selection, highlighted by showing the distributions of the NC Δ signal (red) as well as Cosmic (green) and BNB other (blue) distributions as well as the cut position.*

Sample	**ν Candidate**	$1\gamma Xp$	$1\gamma0p$	$1\gamma1p$	$2\gamma Xp$	$2\gamma0p$	$2\gamma1p$
BNB All	43.0%	8.1%	0.7%	2.9 %	2.9 %	0.4%	0.8%
NC π^0	41.9%	16.5%	3.8%	7.1 %	12.4%	3.6%	5.3%
NC Δ_{Rad} (All)	62.5%	38.1%	12.8%	17.5 %	9.3%	3.0%	3.8%
NC Δ_{Rad} ($1\gamma1p$ Signal)	72.5%	47.1%	9.63%	28.9 %	8.6%	2.3%	4.1%
NC Δ_{Rad} ($1\gamma0p$ Signal)	64.3%	40.1%	20.6%	11.6 %	10.9%	4.3%	4.0%
BNB ν_e	79.7%	40.3%	6.5%	16.2%	17.4%	2.9 %	6.1%
Cosmic Data	15.0%	3.0%	0.37%	1.68%	0.61%	0.13%	0.27%
Dirt	22.8%	3.0%	0.49%	1.77%	0.52%	0.14%	0.24%

Table 1: *Summary table of showing the percentages of total events that fall into each topological category for various samples used in this analysis. The first column shows the overall percentage of events that contain a candidate neutrino vertex, which varies from almost 80% for intrinsic ν_e events to 15% for cosmogenic backgrounds. Here, BNB All refers to the entire BNB induced ν_μ and ν_e (as well as $\overline{\nu}_\mu$ and $\overline{\nu}_e$) interactions in the MicroBooNE cryostat. "Dirt" refers to beam-induced backgrounds which originate outside the cryostat volume; those are described in further detail in Sec. 3.4. Here Xp refers to any number of reconstructed tracks, including 0. Note that the analysis considers only 0 and 1 tracks; however expansion in the future to include $X > 1$ tracks could potentially lead to signal efficiency enhancement in the overall analysis.*

- **Shower Energy Cut:** The calorimetric reconstructed shower energy must be at least 30 MeV.

The combined efficiency of these two pre-selection cuts on the $1\gamma 0p$ signal is greater than 95% relative to the topological stage, while 34.6% of cosmogenic backgrounds are removed. These topological efficiencies for the $1\gamma 0p$ selection are given in Table 1. The resulting $1\gamma 0p$ distribution, following pre-selection, is provided in Fig. 6, right.

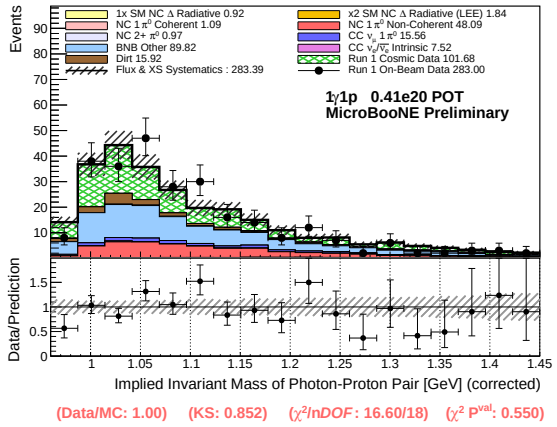

(a) $1\gamma 1p$ *Selection at Pre-selection Cut Stage.*

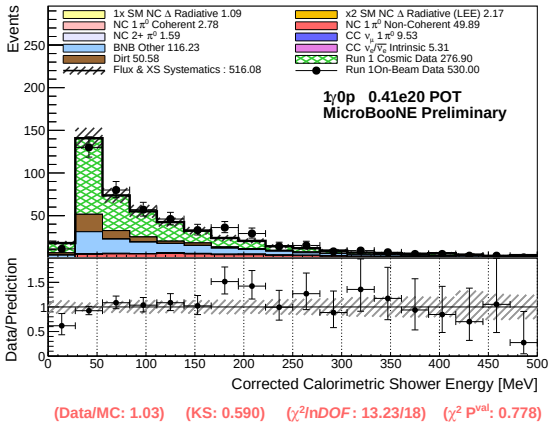

(b) $1\gamma 0p$ *Selection at Pre-selection Cut Stage.*

Figure 6: $1\gamma 1p$ *(left) and* $1\gamma 0p$ *(right) Monte Carlo predicted distributions after the pre-selection cut stage. Predictions are scaled to and compared to the open Run 1 data set. At this stage, cosmogenic backgrounds have been reduced significantly, to the extent that while they still are the largest single contributing background, they are smaller than the total sum of all BNB-driven backgrounds in the* $1\gamma 1p$ *selection. Reasonable data to Monte Carlo prediction agreement is observed, within statistical and systematic uncertainties. Note: detector systematic uncertainties have been evaluated but are omitted in these distributions.*

Cut	**Signal (Truth Matched)**	**Cosmic Data**	**NC$1\pi^0$**
Vertex Fiducial Volume	99.8%	63.9%	88.1%
Track Containment	100.0%	34.3%	79.6%
Shower Start Fiducial Volume	97.4%	79.8%	87.0%
Shower Energy	97.6%	39.2%	80.3%
Track Length-Based Energy	98.6%	53.0%	92.0%
Track Calorimetric Energy	99.3%	73.6%	96.2%
Track Mean dE/dx	95.1%	51.5%	73.3%
Angle between Track and Shower	99.5%	85.8%	96.5%
Combined	**89.0%**	**5.59%**	**44.3%**

Table 2: *Signal and background efficiencies of* $1\gamma 1p$ *pre-selection cuts. Efficiencies are defined relative to the* $1\gamma 1p$ *topological selection.*

3.2 Final Selection

After topological and pre-selection cuts, the signal purity for the $1\gamma 1p$ topology is still $< 1\%$ of total selected events. The challenge of the final selection stage is therefore to reject the overwhelming number of remaining backgrounds, while preserving signal events. This is achieved with an ensemble of five separate multivariate Boosted Decision Trees (BDT's) that each target a different background topology. All vertices which pass the topological selection and pre-selection cuts are passed into these five independent BDT's: cosmic, ν_e, NC π^0, second shower veto (SSV) further targeting NC π^0 backgrounds, and then a final BDT that is trained on all remaining BNB neutrino backgrounds that are not directly targeted by the previous three BDTs; this is referred to as the "BNB Other BDT". The BDT's are trained separately, based on topological and calorimetric information tailored to the specific background they are targeting. For example, the ν_e BDT cut makes use of the dE/dx at the start of the shower, while the SSV BDT makes use of the conversion distance of a second candidate 2D reconstructed shower (which fails 3D reconstruction).

Examples of the top training variables for each BDT in the $1\gamma 1p$ selection are provided in Figs. 7 and 8. Figure 7a, for example, shows the ratio of the shower impact parameter to the shower conversion distance used in the Cosmic BDT. The impact parameter indicates how close the back-projected shower direction comes to the vertex, whereas the conversion distance gives the distance from the shower start to the vertex regardless of the shower direction. If the impact parameter is small relative to the conversion distance, meaning a ratio of approximately 0, that indicates that the shower direction points back well to the vertex and therefore is more likely to be a correctly reconstructed event, whereas events where the shower is incorrectly associated to a vertex do not point back well, and tend to pile up at 1. Figure 7b shows the track truncated mean dE/dx. Given that cosmogenic backgrounds usually contain μ tracks whereas the signal must have a p track, this is a useful training variable.

Figure 7c shows the shower dE/dx where the start of the shower (the trunk) has been fit using a Kalman fitting algorithm, used in the ν_e BDT. Default behavior is to use the collection plane, but if the shower was not reconstructed on this plane, the plane induction plane with most hits is used instead. Given the e/γ separation power of shower dE/dx it makes sense that this variable ranks highly for discriminating ν_e backgrounds. Figure 7d shows the logarithm of shower conversion distance, which is also expected to perform well as a training variable given that e backgrounds should not have a gap between the vertex and the shower start unlike the γ signal. Here we see two peaks, corresponding to attached and un-attached showers with majority of signal having a non-zero conversion distance.

Figure 7e shows the reconstructed shower energy, used in the NC π^0 BDT. As both the majority of π^0 photons and radiative single-photons come from a Δ resonance, the overall energy available is similar. As in the case of the π^0 there are two resulting photons for the same available energy, radiative decay single photons tend to have on average higher energy than NC π^0. Figure 7f shows the Photon Transverse Momentum, assuming that the photon originated at the reconstructed vertex. NC π^0 events in which one photon is missed tend to have a larger transverse (Y-X) momentum spread in the one reconstructed photon, especially when compared to the radiative single photon.
All distributions show good data to MC agreement at this stage.

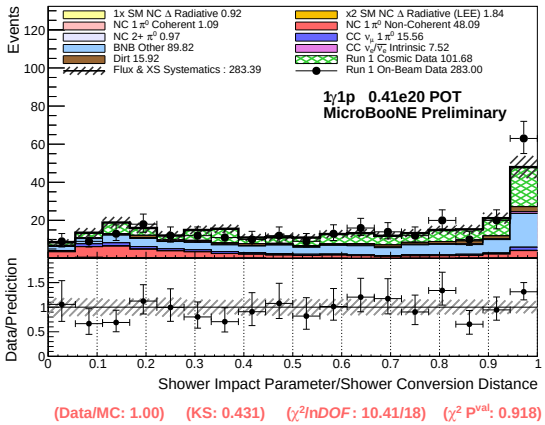

(Data/MC: 1.00) (KS: 0.431) (χ^2/nDOF: 10.41/18) (χ^2 P^{val}: 0.918)

(a) Ratio of Shower Impact Parameter to Shower Conversion Distance

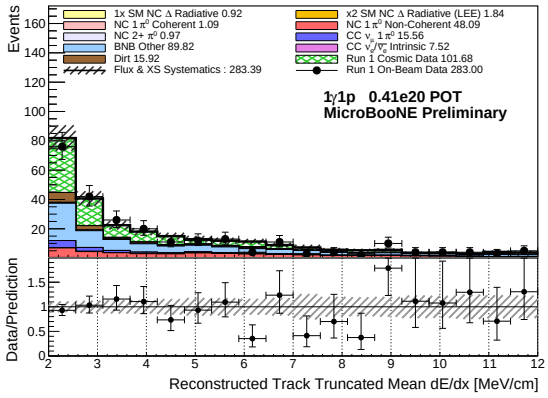

(Data/MC: 1.00) (KS: 0.997) (χ^2/nDOF: 14.76/18) (χ^2 P^{val}: 0.678)

(b) Track Truncated Mean dE/dx

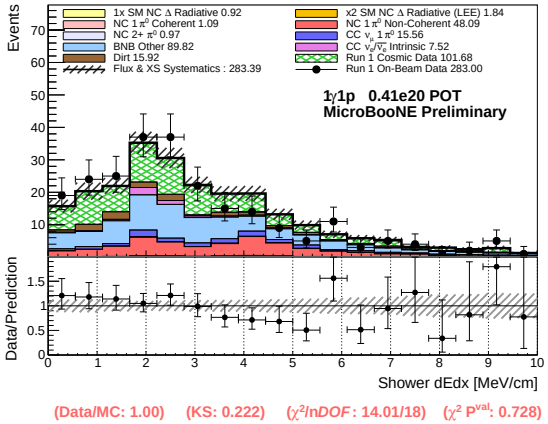

(Data/MC: 1.00) (KS: 0.222) (χ^2/nDOF: 14.01/18) (χ^2 P^{val}: 0.728)

(c) Reconstructed Shower dE/dx

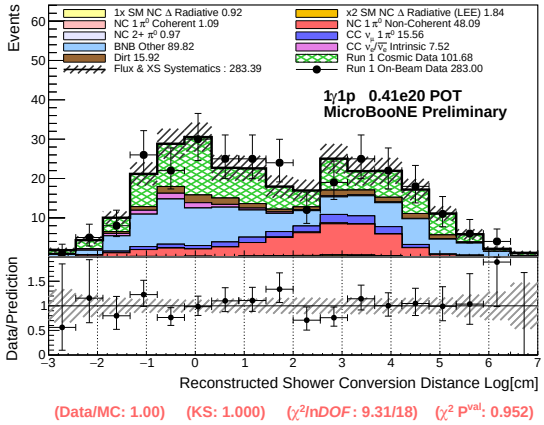

(Data/MC: 1.00) (KS: 1.000) (χ^2/nDOF: 9.31/18) (χ^2 P^{val}: 0.952)

(d) Photon Conversion Distance

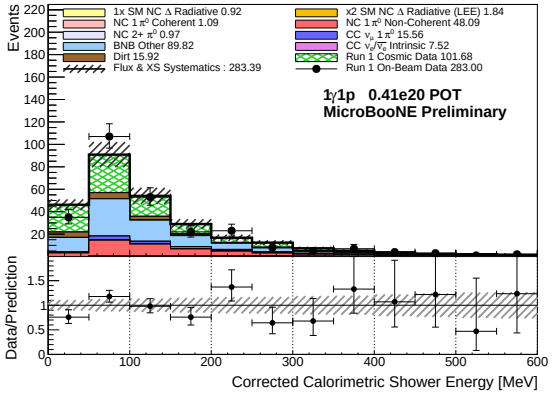

(Data/MC: 1.00) (KS: 0.973) (χ^2/nDOF: 8.85/12) (χ^2 P^{val}: 0.715)

(e) Reconstructed Shower Energy

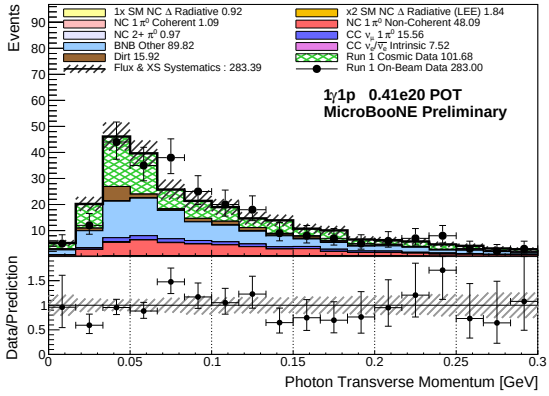

(Data/MC: 1.00) (KS: 0.759) (χ^2/nDOF: 12.66/18) (χ^2 P^{val}: 0.811)

(f) Photon Transverse Momentum

Figure 7: *Monte Carlo prediction to data comparisons for some of the top training variables used for the 1γ1p BDT's, in terms of the total gain, shown at the pre-selection cut stage. Note: detector systematic uncertainties have been evaluated but are omitted in these distributions.*

Figure 8a shows the second shower search closest 2D candidate conversion distance, used in the SSV BDT, while Fig. 8b shows the angle of the 3D second shower search candidate which points back best to the reconstructed vertex, with respect to the primary shower. Clusters which peak at 1 correspond to a small-opening angle between the candidate 3D cluster and the selected reconstructed shower, which means they are quite co-linear with the reconstructed shower. Combining this information with conversion distance can separate out cases of a second shower and cases where it is a fragment of the primary shower incorrectly clustered.

Figure 8c shows the log of the maximum distance from a 3D space point that is clustered into the selected reconstructed track to a linear fit to all of the space points in the track, used in the BNB Other BDT. This is a metric of how straight and clean the track is. Figure 8d shows the Pandora shower score assigned to all reconstructed showers, also used in the BNB Other BDT, with 0 corresponding to very shower-like and 0.5 to less shower-like. Here we see that the signal events tend towards low score whereas the backgrounds span the full range of scores.

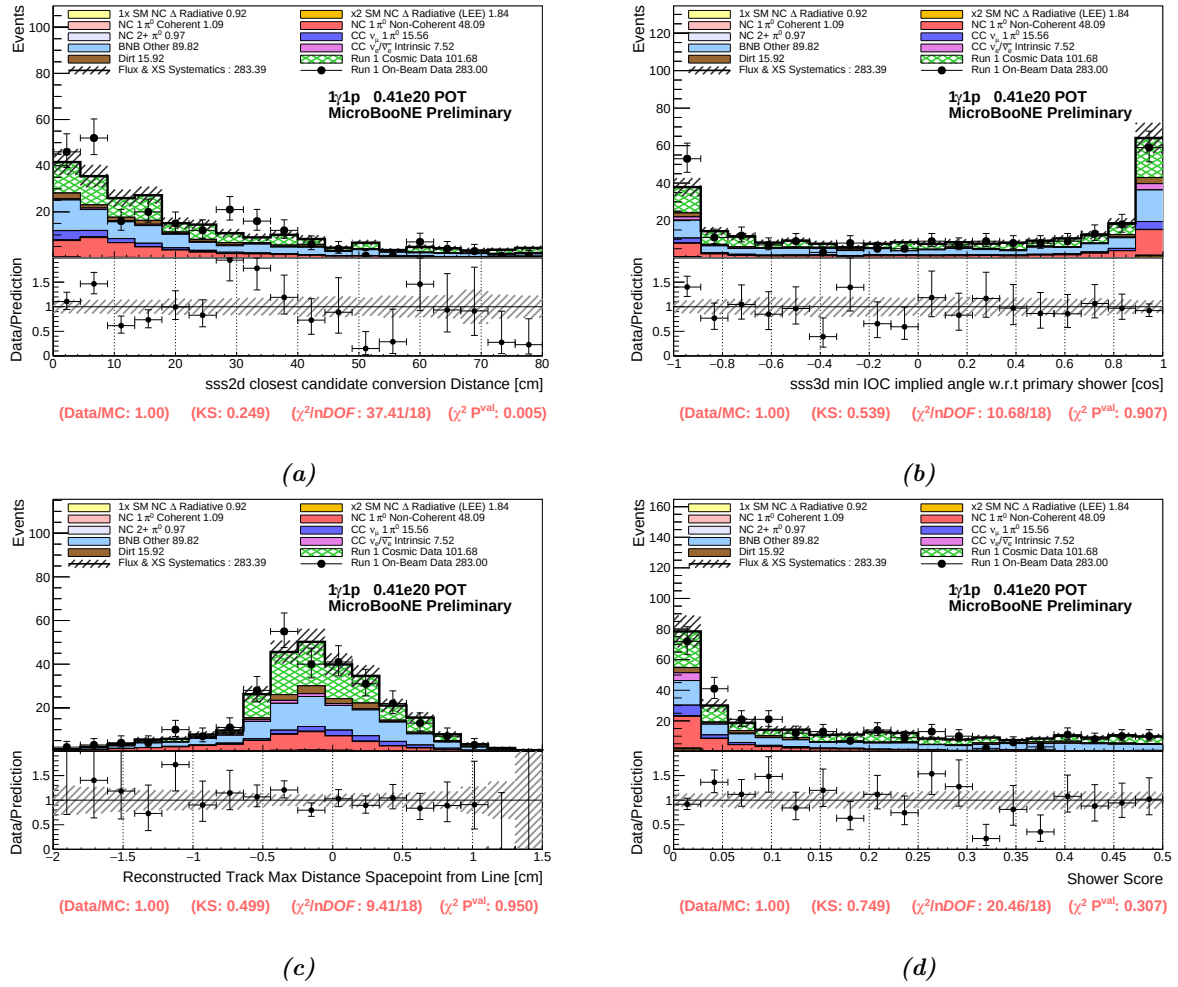

Figure 8: *Monte Carlo prediction to data comparisons for some of the top training variables used for the 1γ1p BDT's, in terms of the total gain, shown at the pre-selection cut stage. Note: detector systematic uncertainties have been evaluated but are omitted in these distributions.*

Similarly, several BDT training variables are shown for the $1\gamma 0p$ selection in Fig. 9. Figure 9a shows the reconstructed photon transverse momentum, a top training variable for the BNB BDT, which shows good data-MC agreement at this stage. Figure 9b shows the Pandora neutrino score, a top training variable for the cosmic BDT, which also shows good agreement and as expected we see that true showers like those from the ν_e and π^0 backgrounds peak at low shower score. Variable importance here is defined in terms of the variable's "gain" which is a measure of the improvement in accuracy of a model when the variable in question is used in a BDT branch. Figure 9c shows the ratio of the shower energy to geometric size, also used in the cosmic BDT. If the ratio is large, this indicates that the energy is high relative to the size of the reconstructed shower which is useful for removing tracks mis-reconstructed as showers or highly energetic cosmogenic showers. Finally, Fig. 9d shows the dE/dx calculated with the Kalman track fitter and all planes, used in the BNB BDT.

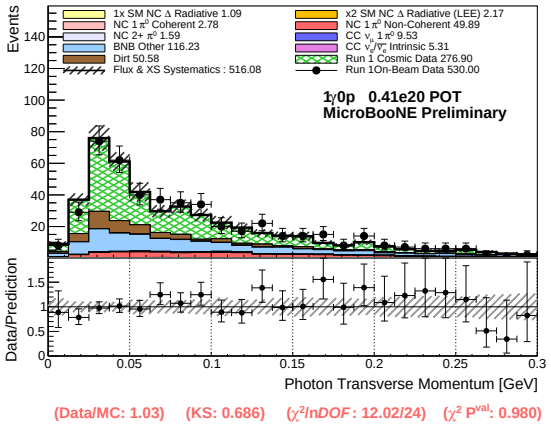

(a) Reconstructed Photon Transverse Momentum

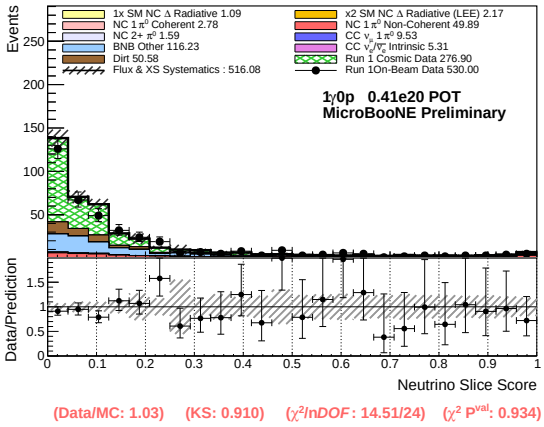

(b) Pandora Neutrino Score

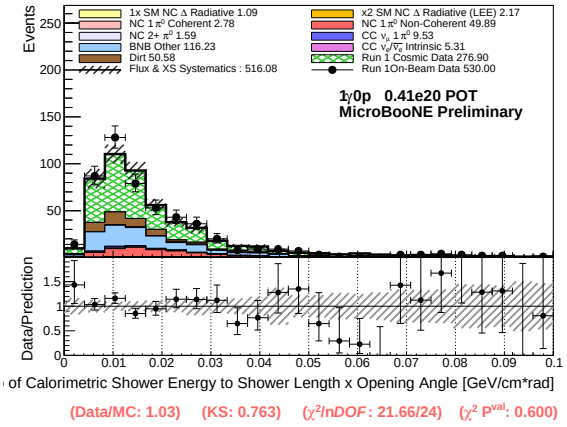

(c) Ratio of Shower Energy to Geometric Size

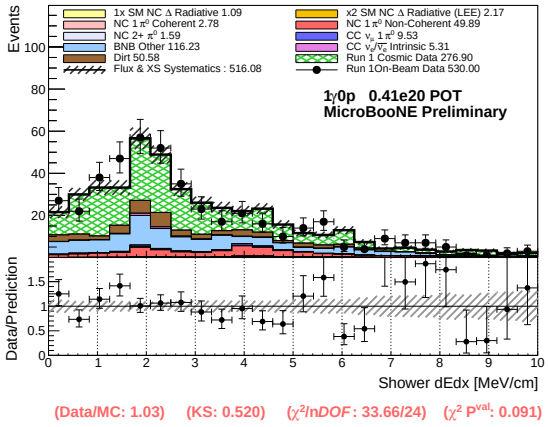

(d) Shower dE/dx

Figure 9: *Monte Carlo prediction to data comparisons for some of the training variables for the* $1\gamma 0p$ *BDT's, shown at the pre-selection cut stage. Note: detector systematic uncertainties have been evaluated but are omitted in these distributions.*

After training, the BDT cuts are optimized simultaneously on the final selected sample ($1\gamma 1p$ or $1\gamma 0p$), in order to maximize signal to background. Distributions of the BDT responses, after training, are provided in Figs. 10 and 11 for $1\gamma 0p$ and $1\gamma 1p$, respectively. As can be seen in several of these BDT responses, the NC Δ signal events, while generally peaking at high BDT score response as expected, also has smaller peaks at low BDT score. This is primarily due to the fact that the Δ radiative histogram is showing all events in which a NC Δ radiative scattering took place, regardless of whether or not the reconstructed shower and/or track candidates are reconstructed well. We break this down for the Cosmic BDT further in Fig. 12, where we split the NC Δ radiative sample into five categories. In this breakdown it can be seen that over 93% of the well-reconstructed events that are defined to have one visible proton and photon have a cosmic BDT response score above 0.95. The flatness of the signal BDT response for NCπ^0 and SSV BDT, is partially due to this same effect, but also stresses the fact that kinematically a certain fraction of NC π^0 decays in which one shower is missed look almost indistinguishable from our signal, meaning separation is extremely difficult.

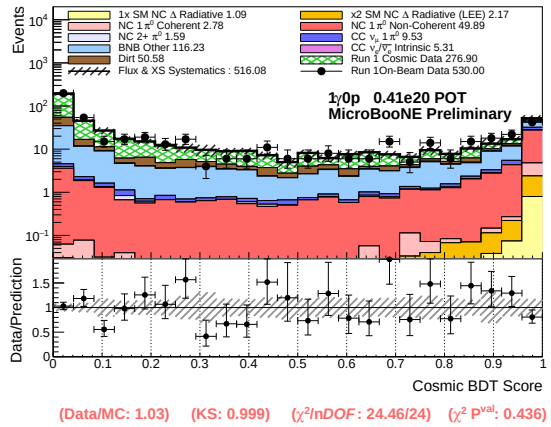

(a) $1\gamma 0p$ *Cosmic BDT Response*

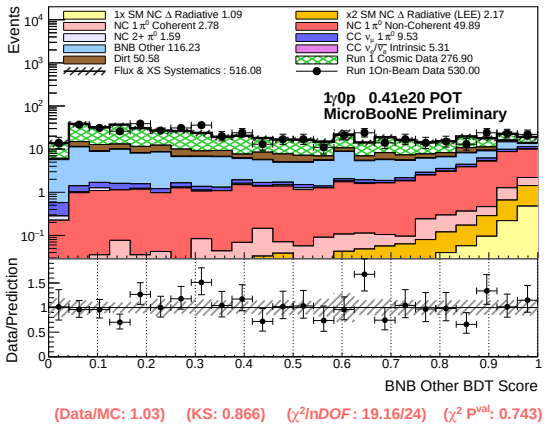

(b) $1\gamma 0p$ *BNB Other BDT Response*

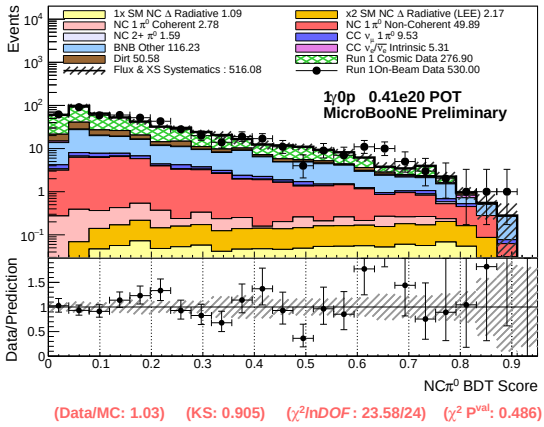

(c) $1\gamma 0p$ *NC* π^0 *BDT Response*

Figure 10: *BDT response distributions for the* $1\gamma 0p$ *selection. The Monte Carlo predictions are scaled to* $5{\times}10^{19}$ *POT, and compared to corresponding data from Run 1. The data and Monte Carlo agree reasonably within statistical and systematic uncertainties, and each BDT is capable of providing noticeable signal to background differentiation. Note: detector systematic uncertainties have been evaluated but are omitted in these distributions.*

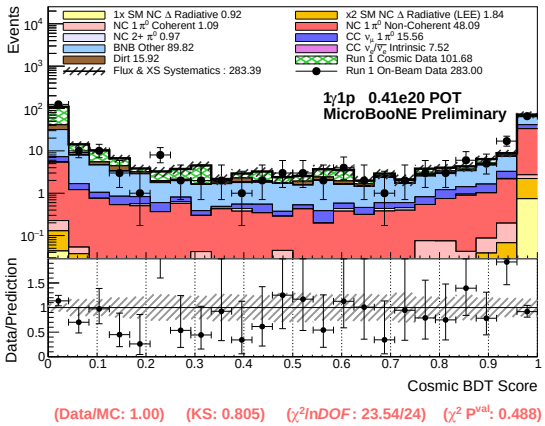

(Data/MC: 1.00) (KS: 0.805) (χ^2/nDOF: 23.54/24) (χ^2 P^{val}: 0.488)

(a) $1\gamma1p$ *Cosmic BDT Response*

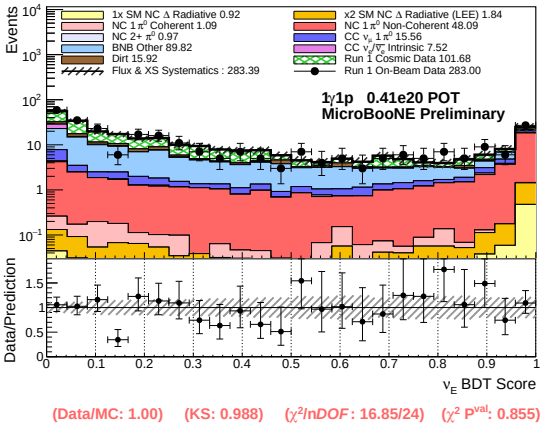

(Data/MC: 1.00) (KS: 0.988) (χ^2/nDOF: 16.85/24) (χ^2 P^{val}: 0.855)

(b) $1\gamma1p$ ν_e *BDT Response*

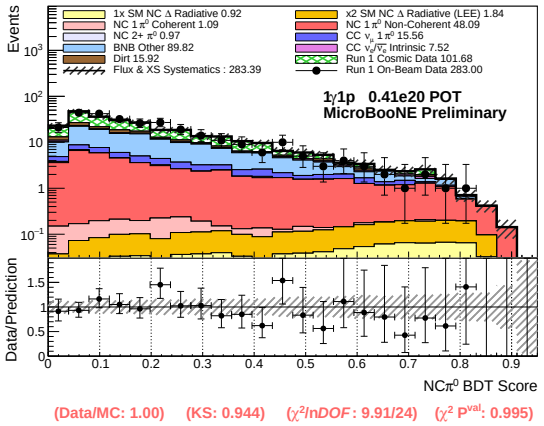

(Data/MC: 1.00) (KS: 0.944) (χ^2/nDOF: 9.91/24) (χ^2 P^{val}: 0.995)

(c) $1\gamma1p$ *NC* π^0 *BDT Response*

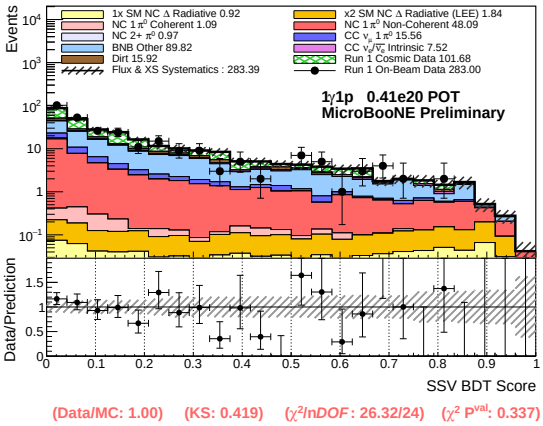

(Data/MC: 1.00) (KS: 0.419) (χ^2/nDOF: 26.32/24) (χ^2 P^{val}: 0.337)

(d) $1\gamma1p$ *SSV BDT Response*

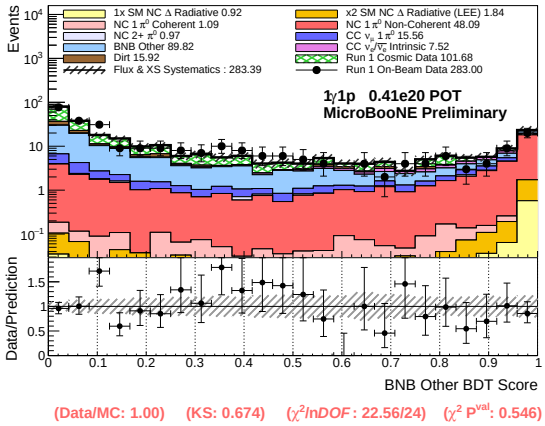

(Data/MC: 1.00) (KS: 0.674) (χ^2/nDOF: 22.56/24) (χ^2 P^{val}: 0.546)

(e) $1\gamma1p$ *BNB Other BDT Response*

Figure 11: *BDT response distributions for the* $1\gamma1p$ *selection. The Monte Carlo predictions are scaled to* 4.1×10^{19} *POT, and compared to corresponding data from Run 1. The data and Monte Carlo agree reasonably within statistical and systematic uncertainties, and each BDT is capable of providing noticeable signal to background differentiation. Note: detector systematic uncertainties have been evaluated but are omitted in these distributions.*

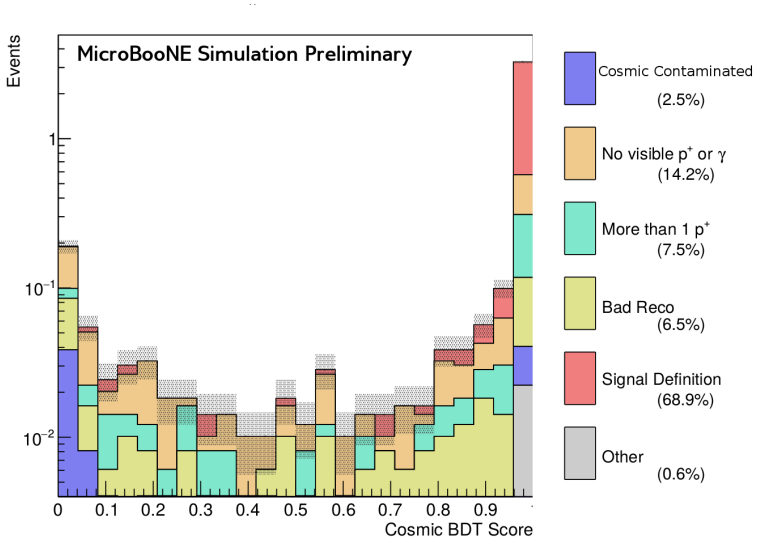

Figure 12: *A breakdown of the NC Δ Radiative MC sample's cosmic BDT response, as shown in yellow and orange stacked histograms in Fig. 11a. For the purposes of counting visibility, protons and photons must have greater than 20 MeV KE (e.g, protons with $<$ 20 MeV are counted as 0 proton events) and cosmic contamination is defined as an event in which either the track or shower contains more than 50% of its hits coming from cosmic events. Bad reconstruction ("Bad reco") is an event where the track or shower are not matched to the Δ decay proton or photon respectively. Note the logarithmic scale on the y axis. In this breakdown it can be seen that over 93% of the well-reconstructed signal events that are defined to have one visible proton and photon have a cosmic BDT response score above 0.95.*

The effect of each BDT score cut, applied independently on pre-selected events, is shown in Figs. 13 and 14 for $1\gamma 0p$ and $1\gamma 1p$, respectively. Final selection is performed with the optimized BDT cuts provided in Tab. 3.

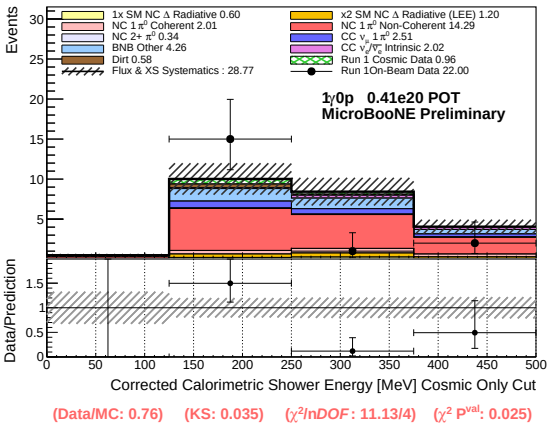

(a) After Pre-selection and Cosmic BDT >0.988

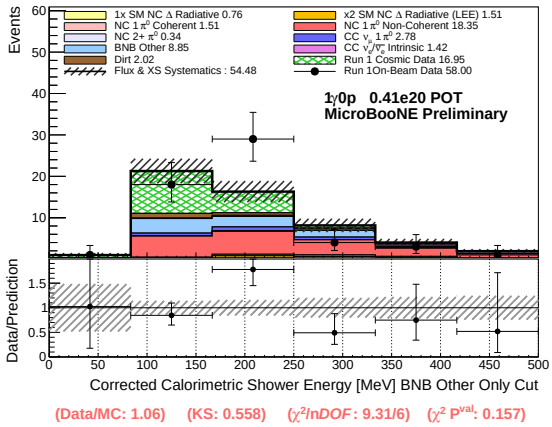

(b) After Pre-selection and BNB Other BDT > 0.893.

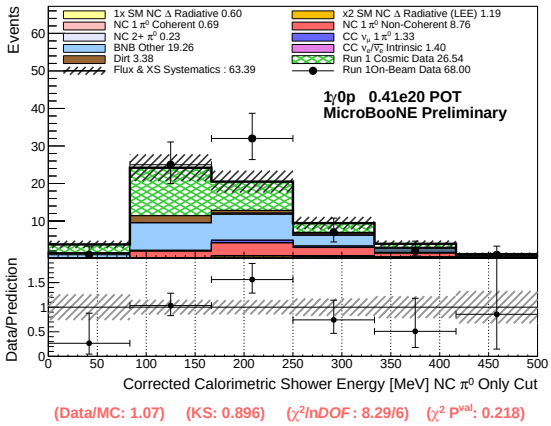

(c) After Pre-selection and NC π^0 BDT > 0.429.

Figure 13: *$1\gamma 0p$ predicted distributions and comparisons to Run 1 open data after pre-selection cuts and each optimized BDT cut applied as indicated on each sub-figure caption. Reasonable data to Monte Carlo agreement is observed for all distributions. Note: detector systematic uncertainties have been evaluated but are omitted in these distributions.*

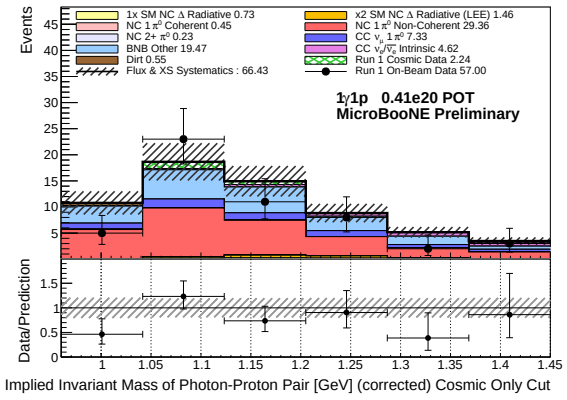

(a) After Pre-selection and Cosmic BDT >0.975

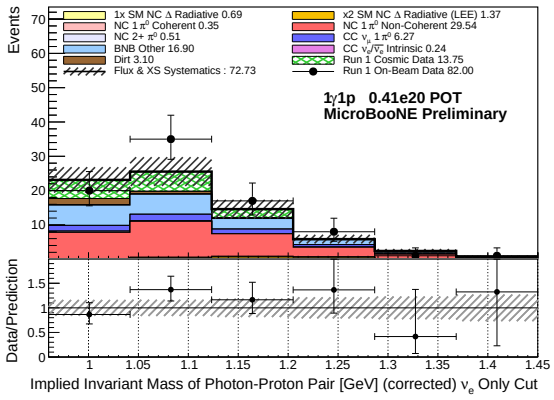

(b) After Pre-selection and ν_e BDT >0.571.

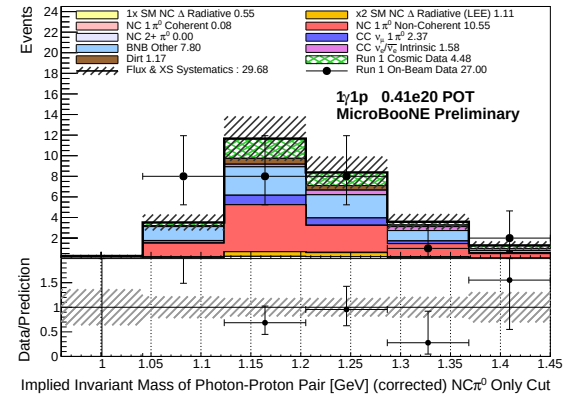

(c) After Pre-selection and NC π^0 BDT >0.467

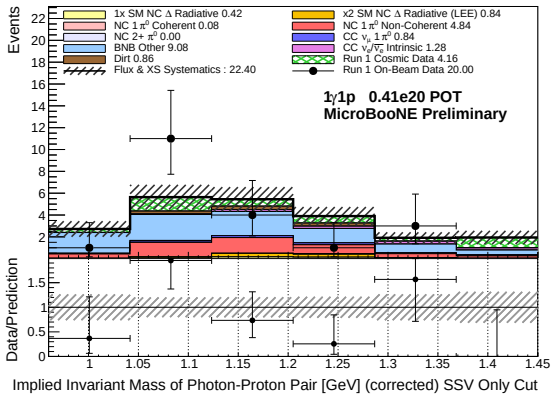

(d) After Pre-selection and SSV BDT >0.522

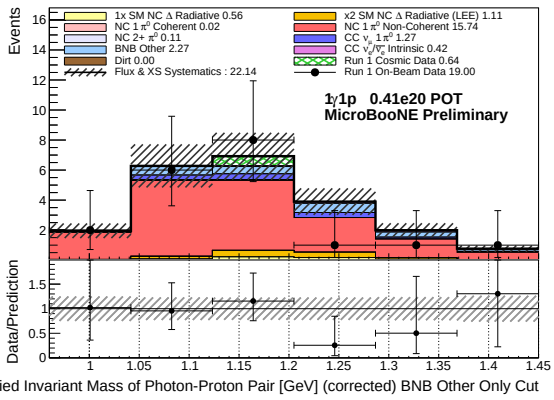

(e) After Pre-selection and BNB Other BDT >0.963

Figure 14: *1γ1p predicted distributions and comparisons to Run 1 open data after pre-selection cuts and each optimized BDT cut applied as indicated on each sub-figure caption. Reasonable data to Monte Carlo agreement is observed for all distributions. Note: detector systematic uncertainties have been evaluated but are omitted in these distributions.*

	Cosmic BDT	BNB Other BDT	NC π^0 BDT	ν_e BDT	SSV BDT
$1\gamma 1p$ **Selection**					
Score cut:	0.975	0.963	0.467	0.571	0.522
Signal efficiency:	18.9%	15.5%	14.7%	17.9%	23.5%
$1\gamma 0p$ **Selection**					
Score cut:	0.988	0.893	0.429	-	-
Signal efficiency:	55.3%	69.6%	47.4%	-	-

Table 3: *Summary of optimized BDT score cuts applied to each selection, $1\gamma 1p$ and $1\gamma 0p$, and corresponding signal efficiencies.*

The resulting distributions for both the $1\gamma 1p$ and the $1\gamma 0p$ selections are shown in Figs. 15 and 16, respectively. The resulting number of events, at final selection stage, is provided in Tab. 12. The two data events passing final selection, from the $1\gamma 1p$ sample, are shown in Fig. 17 and two representative events from the $1\gamma 0p$ selection are shown in Fig. 18. The distributions are provided for the currently unblinded data sample from Run 1, corresponding to a bit less than 5×10^{19} POT agyer data quality cuts. This corresponds to $< 5\%$ of the total collected data by MicroBooNE. The corresponding predicted distributions projected to the full available data set, corresponding to 12.25×10^{20} POT, are shown in the right panels of Figs. 15 and 16.

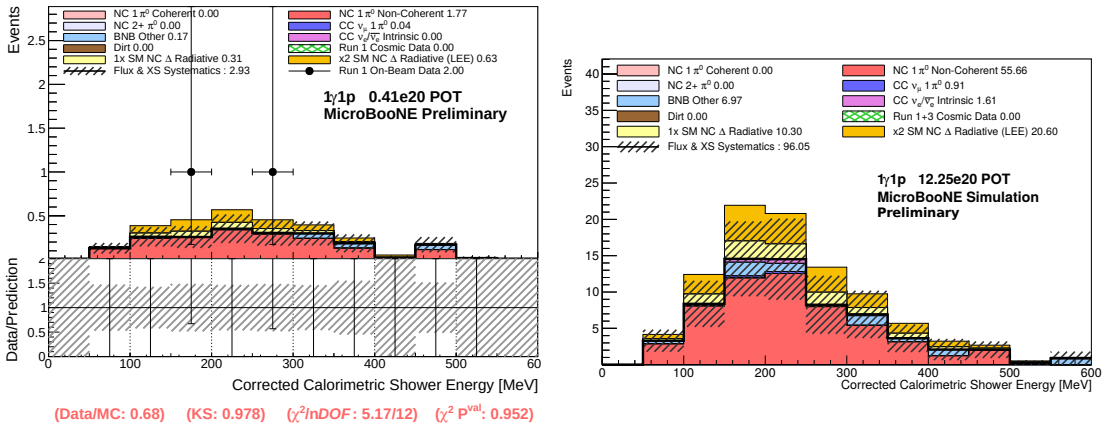

Figure 15: *$1\gamma 1p$ final selection with all cuts applied. On the left is the reconstructed shower energy for Run 1 open data showing 2 surviving data events in the selection, with an expectation of ~ 3 Monte Carlo events. On the right is the same predicted distribution for the full MicroBooNE data set of 12.25×10^{20} POT. The shaded band corresponds to the combined flux, cross-section and statistical (due to finite statistics) uncertainty on the Monte Carlo. Note: detector systematic uncertainties have been evaluated but are omitted in these distributions.*

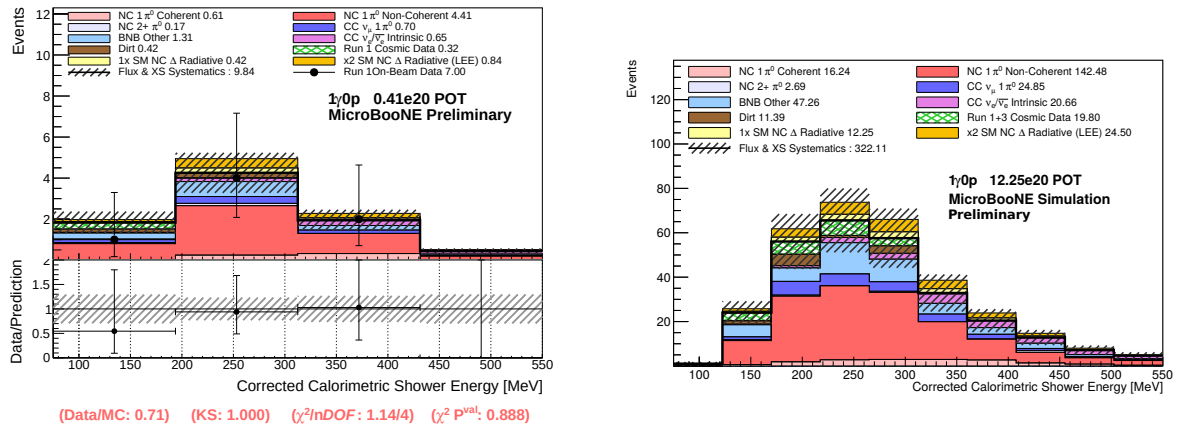

Figure 16: *1γ0p final selection with all cuts applied. The top figure shows reconstructed shower energy for Run 1 open data showing 7 surviving data events in the selection, with an expectation of* ~ 9.8 *Monte Carlo events. The bottom figure shows the predicted distribution for the full MicroBooNE data set of* 12.25×10^{20} *POT. The shaded band corresponds to the combined flux, cross-section and statistical (due to finite statistics) uncertainty on the Monte Carlo. Note: detector systematic uncertainties have been evaluated but are omitted in these distributions.*

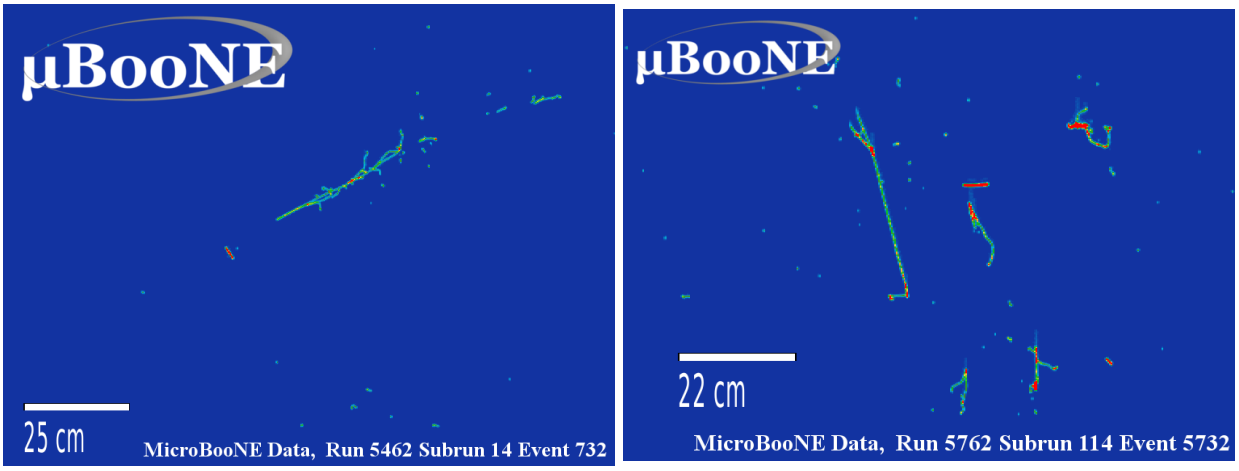

Figure 17: *The two data events passing the final* $1\gamma 1p$ *selection in the open Run 1 data sample. Left: The first event showing clean conversion distance and no strong evidence of a secondary shower that would be suggestive of it being NC* π^0 *in origin. Although based on our simulation it is most likely a NC* π^0*, it highlights a data event that matches out signal extremely well. Right: Here, the highly ionizing track in the center is reconstructed as the proton, with the three electromagnetic showers at the bottom being reconstructed as a single photon candidate. The rightmost shower, as well as the multiple tracks on the left were reconstructed in a separate slice. This is an example of a* π^0 *event that due to reconstruction failures is a clear background to the selection.*

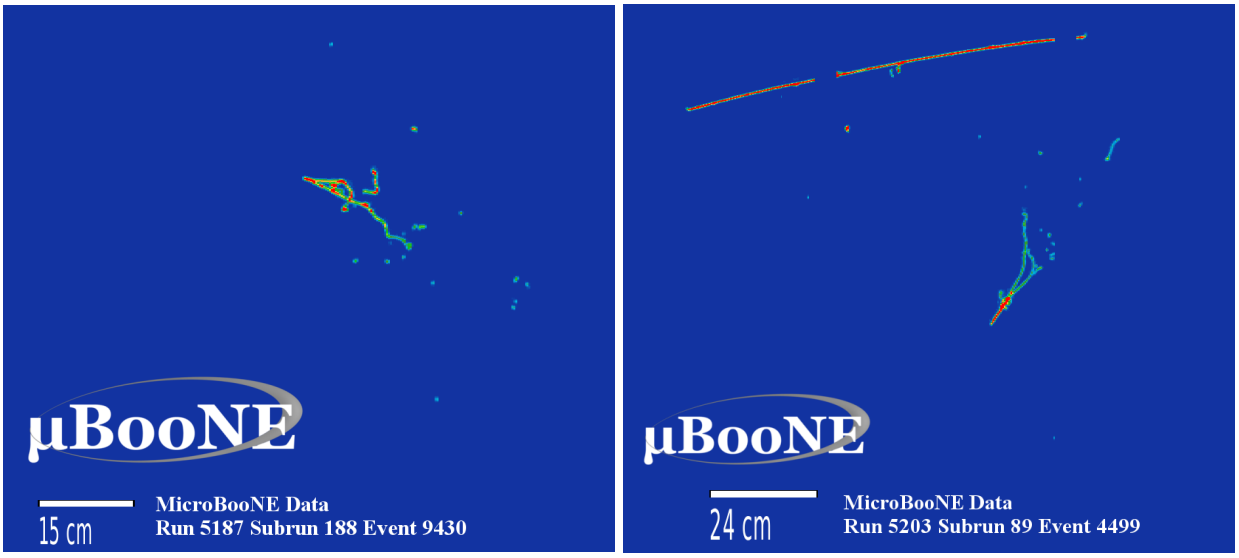

Figure 18: *Two example data events passing the final* $1\gamma 0p$ *selection in the open Run 1 data sample. Both showers show a large dE/dx at the shower start, with the characteristic* e^+e- *pair production 'V' shape.*

3.3 Sideband Validation

The single photon analysis is performed as a blind analysis, whereby the reconstruction, selection, and final fits are finalized with statistics-limited data sets, which provide negligible sensitivity to an enhanced rate of NC Δ radiative decay events. After the analysis is finalized, and prior to signal unblinding, higher statistics "sideband boxes," comprising events which are topologically similar to our 1γ signal but signal-blind, are studied. This allows us to confirm that our backgrounds are correctly predicted and reconstructed in our analysis.

Three mutually exclusive $1\gamma1p$ sideband boxes have been defined in terms of inverse optimized BNB Other and NC π^0 BDT cuts. The sideband "boxes" are defined to be exclusive of the signal-inclusive box (box A):

- Box B is defined as events passing the optimized NC π^0 BDT cut but failing the optimized BNB Other BDT cut.
- Box C is defined as events failing both the optimized NC π^0 BDT cut and the optimized BNB Other BDT cut.
- Box D is defined as events failing the optimized NC π^0 BDT cut but passing the optimized BNB Other BDT cut.

Since NC π^0 mis-identified events are the primary background, the boxes explicitly target at least one high-statistics sideband sample which is NC π^0 pure, as well as others which target other backgrounds more holistically. The resulting distributions are shown in in Figs. 19 through 21 for the currently open 5×10^{19} POT data set from Run 1, showing reasonable data to Monte Carlo agreement (all $p-$values $>$ 5%). In order to preserve blindness to electron-like interpretations of the MiniBooNE low energy excess, as analyses targeting such interpretations are currently ongoing by the MicroBooNE collaboration [12, 13], we utilize the ν_e rejection BDT as shown in Fig. 11 and pre-apply a cut removing 92.5% of intrinsic ν_e events for all sideband boxes. Processing of Run 1-3 data through sideband selection is ongoing to provide higher-statistics comparisons prior to signal unblinding.

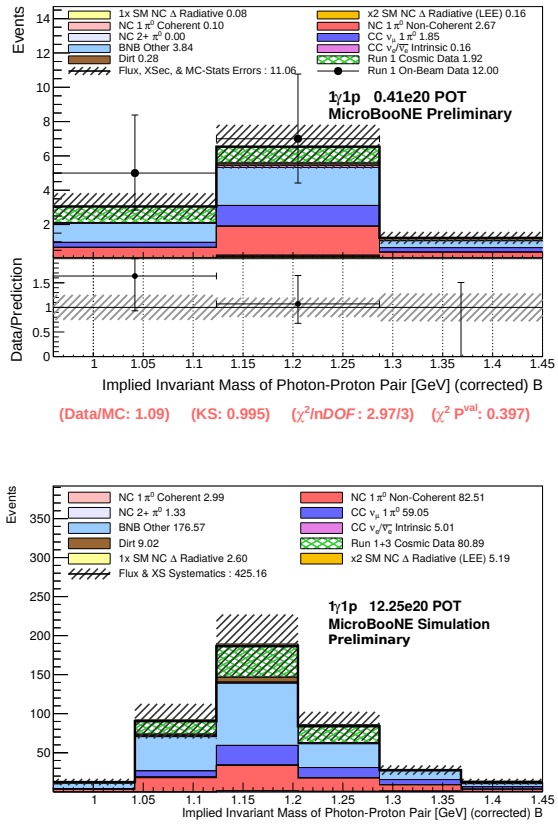

Figure 19: *The reconstructed Δ invariant mass distribution for (far sideband) box B, defined as passing the optimized NC π^0 BDT cut but failing the optimized BNB Other BDT cut. Top: Run 1 open data, in comparison with MC prediction. Bottom: MC prediction for 12.25×10^{20} POT, corresponding to the full data set for Runs 1-5. Note: detector systematic uncertainties have been evaluated but are omitted in these distributions.*

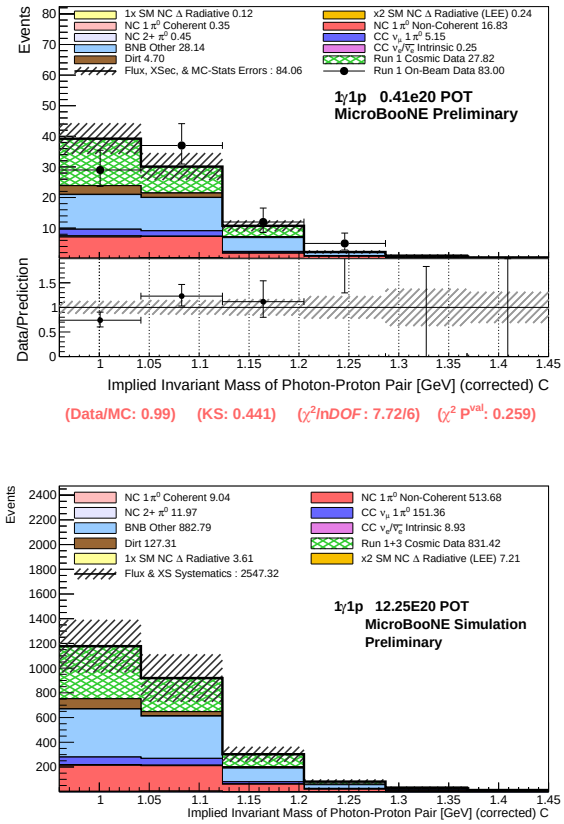

Figure 20: *The reconstructed Δ invariant mass distribution for (far sideband) box C, defined as failing both the optimized NC π^0 BDT cut and the optimized BNB Other BDT cut. Top: Run 1 open data, in comparison with MC prediction. Bottom: MC prediction for 12.25×10^{20} POT, corresponding to the full data set for Runs 1-5. Note: detector systematic uncertainties have been evaluated but are omitted in these distributions.*

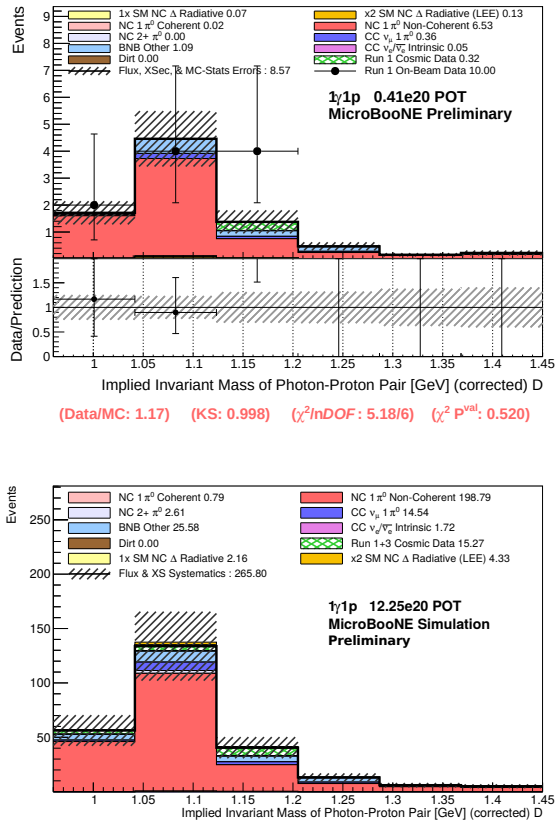

Figure 21: *The reconstructed Δ invariant mass distribution for (far sideband) box D, defined as failing the optimized NC π^0 BDT cut but passing the optimized BNB Other BDT cut. Top: Run 1 open data, in comparison with MC prediction. Bottom: MC prediction for 12.25×10^{20} POT, corresponding to the full data set for Runs 1-5. Note: detector systematic uncertainties have been evaluated but are omitted in these distributions.*

3.4 Validation of "Dirt" Backgrounds

In early stages of the analysis, a particularly concerning background, which was large in the MiniBooNE search for ν_e CCQE-like events, has been "dirt" events. These are neutrino-beam-induced events which originate outside the active detector volume, but whose final state products make it through the active volume and are mis-reconstructed and mis-identified as single-photon events.

As such, a targeted selection was developed to isolate a dirt-rich sample in MicroBooNE, and verify data to Monte Carlo agreement, thus building confidence that this type of background is accurately predicted and accounted for in the single photon analysis. The number of predicted dirt events, scaled to a data set corresponding to 12.25×10^{20} POT, is shown for each successive $1\gamma1p$ and $1\gamma0p$ selection stage (starting with topological selection and ending with final selection) in Figs. 22 and 23. The contribution to the $1\gamma1p$ final selected sample is negligible. However, as expected, it's harder to reject dirt events in the $1\gamma0p$ selection, as shown by the non-negligible background in Fig. 23. This is because for the $1\gamma0p$ case there is no reconstructed track to provide information about the vertex position. The ability to accurately reconstruct the neutrino vertex using these tagged protons is an excellent demonstration of the power of topological reconstruction in a LArTPC.

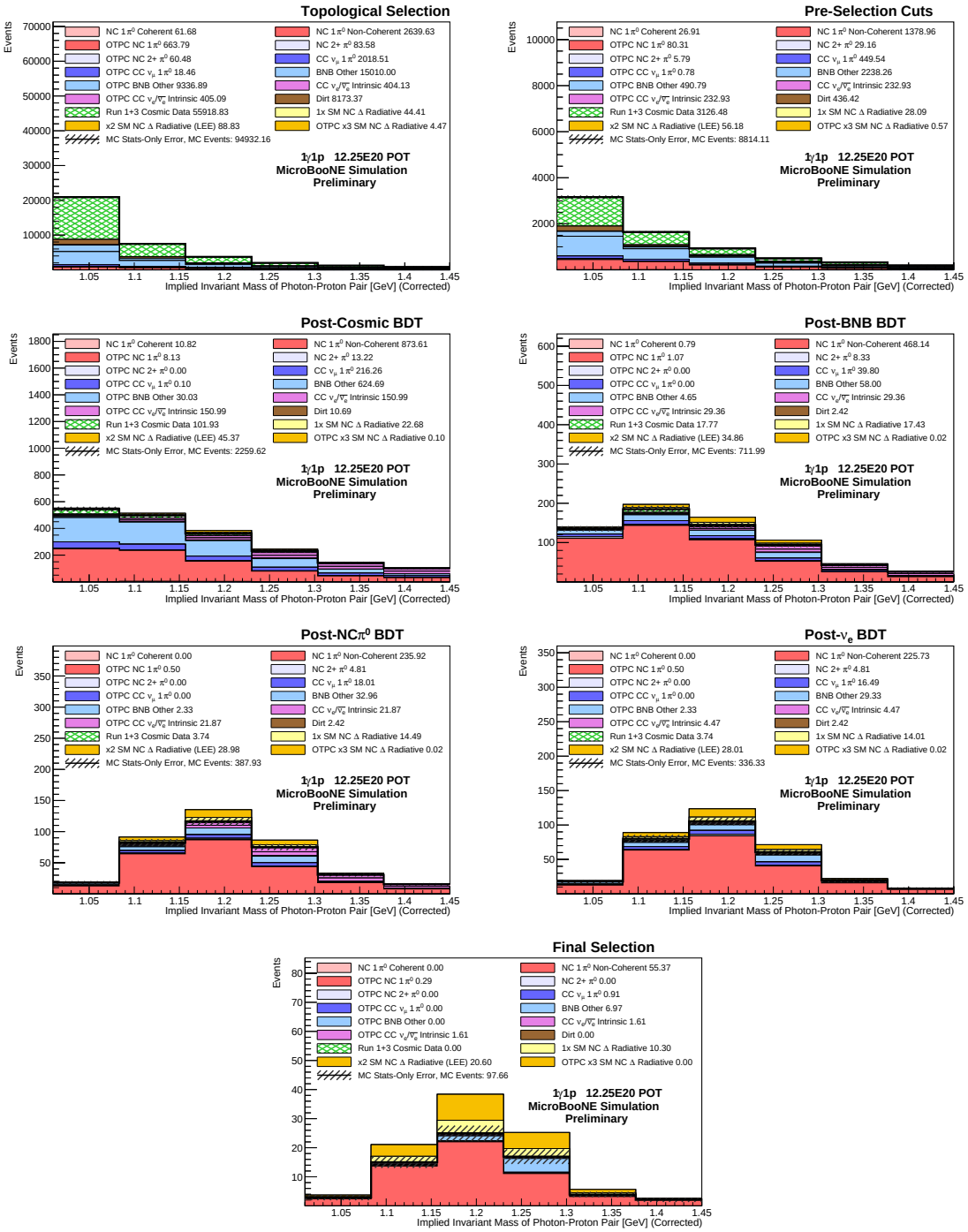

Figure 22: *The 1γ1p sample, starting with topological selection stage (top left), and as a function of subsequent selection stages, showing contribution from "dirt" events, in brown. From left to right, and top to bottom: topological selection stage, preselection stage, cosmic BDT, BNB BDT, NC π^0 BDT, BNB ν_e BDT, and SSV BDT (final selection) stage. OTPC signifies the true neutrino interaction took place outside of the active TPC volume, but inside of the cryostat, and is another source of "dirt" events. By final selection stage, the number of predicted dirt events in the final selected sample is small, but non-negligible. The distributions are scaled to 12.25$\times 10^{20}$ POT, corresponding to MicroBooNE Runs 1-5. Shown are only Monte Carlo intrinsic statistical uncertainties.*

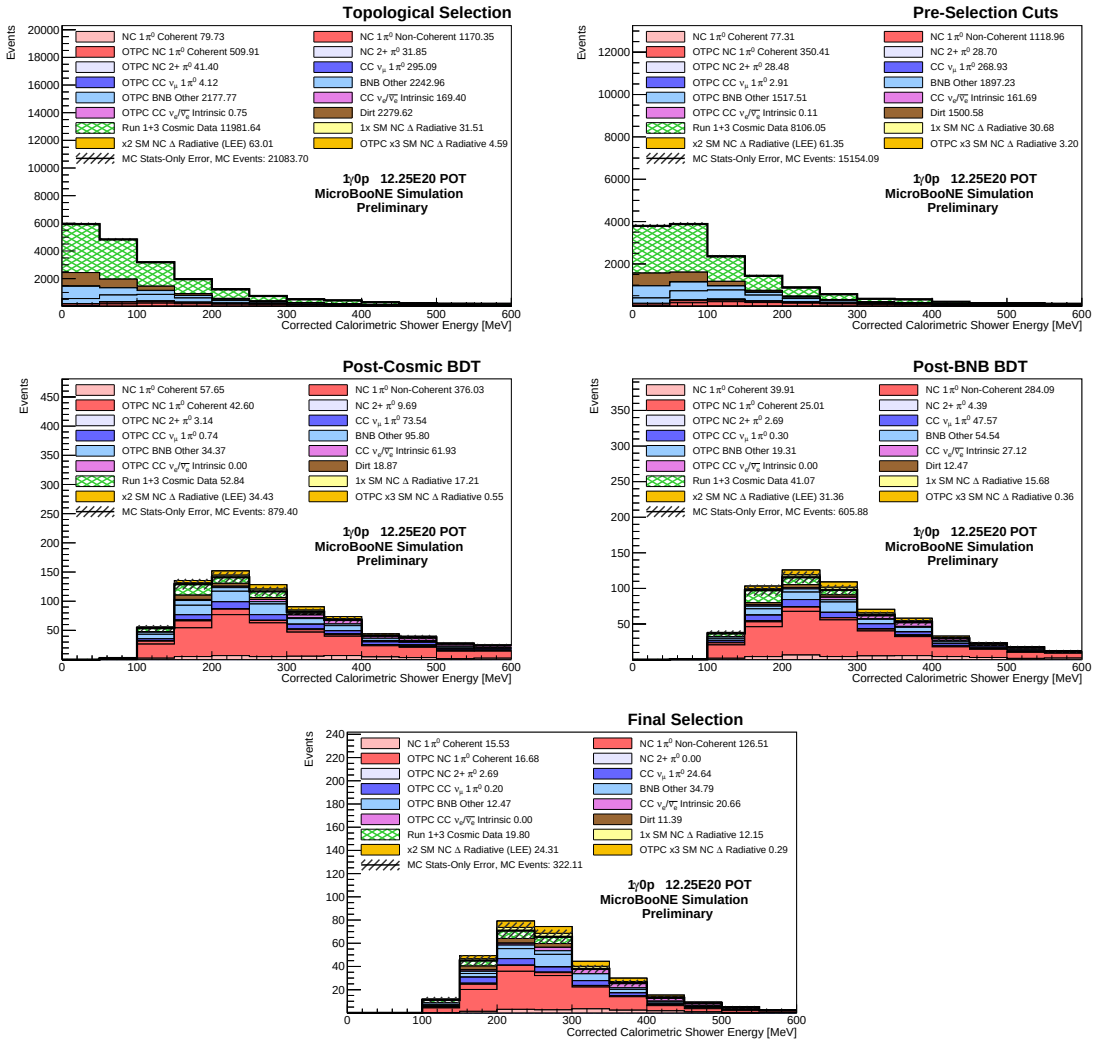

Figure 23: *The 1γ0p sample, starting with topological selection stage (top left), and as a function of subsequent selection stages, showing contribution from "dirt" events, in brown. From left to right, and top to bottom: topological selection stage, preselection stage, cosmic BDT, BNB BDT, and NC π^0 BDT (final selection) stage. OTPC signifies the true neutrino interaction took place outside of the active TPC volume, but inside of the cryostat, and is another source of "dirt" events. By final selection stage, the number of predicted dirt events in the final selected sample is small but not negligible. The distributions are scaled to 12.25×10^{20} POT, corresponding to MicroBooNE Runs 1-5. Shown are only Monte Carlo intrinsic statistical uncertainties.*

At topological selection stage, the total dirt contribution breakdown is as shown in Fig. 24. Dirt backgrounds to both $1\gamma 1p$ and $1\gamma 0p$ topological selections are dominated by cosmogenic background-contaminated reconstructed showers, shown in bright green. Dirt backgrounds to the $1\gamma 1p$ topological selection are also dominated by electrons from muon decay. Those are removed at pre-selection cut stage with a shower energy cut. An example of a simulated dirt Monte Carlo event which passes final $1\gamma 1p$ selection is shown in Fig. 25.

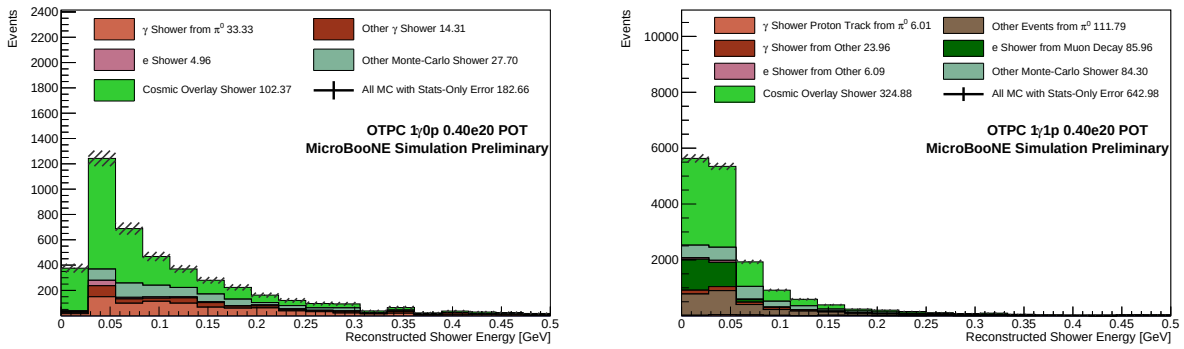

Figure 24: *True composition breakdown of* $1\gamma 0p$ *(left) and* $1\gamma 1p$ *(right) dirt events at topological selection level. Dirt backgrounds to both* $1\gamma 1p$ *and* $1\gamma 0p$ *topological selections are dominated by cosmogenic background-contaminated reconstructed showers, shown in bright green. Dirt backgrounds to the* $1\gamma 1p$ *topological selection are also significantly contributed from electrons from muon decay. Those are removed at pre-selection stage with a shower energy cut.*

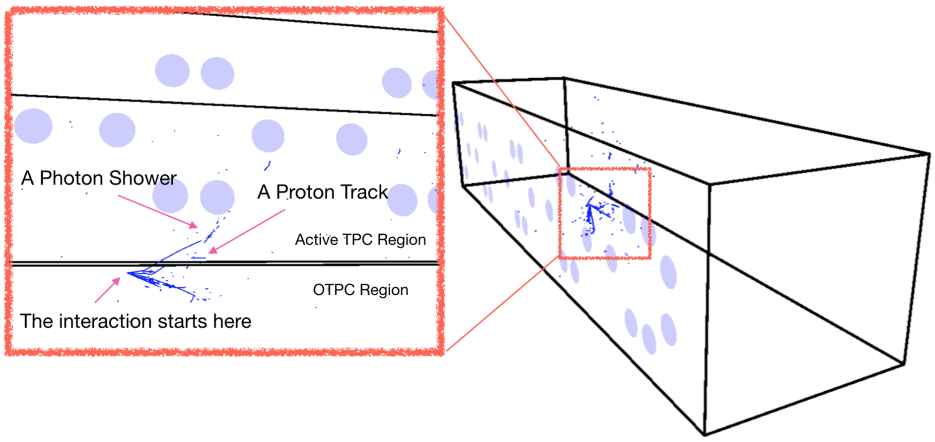

Figure 25: *Argo [14] event display for a true dirt Monte Carlo event which passes final* $1\gamma 1p$ *selection. Right: full detector view, with the ionization charge deposition 3D spacepoints highlighted in blue; the light blue circles represent PMTs above certain activity. Left: zoom-in view near the TPC boundary, showing the interaction vertex outside the rectangular active TPC volume.*

To verify the accuracy of the dirt background predictions, a targeted selection has been developed, which makes use of directional vectors to preferentially select events originating near the active TPC boundary, which point inward toward the detector, and/or opposite to the beam-forward direction. Specifically, the following variables are considered:

- Geometrical Variables:
  1. Start point and orientation (θ_{yz}, ϕ_{yx}) of the reconstructed shower.
  2. End points (both start and end point) and orientation (θ_{yz}, ϕ_{yx}) of the reconstructed track (applicable to the $1\gamma 1p$ topological selection, only).
- Vertex reconstruction:
  1. Distance of the reconstructed shower start point to the reconstructed vertex.
  2. Distance of the reconstructed track end points to the reconstructed vertex.
- Reconstructed visible energy:
  1. The maximum reconstructed shower energy among three wire planes.
  2. The reconstructed track kinetic energy assuming the track is a proton.
- Inner products of reconstructed object (track or shower) directional vectors, with the latter illustrated in Fig. 26. Directional vectors are defined by the reconstructed shower cone or track, pointing from the shower cone or track start point to the end point. Inner products are then constructed from the normalized directional vectors and the following vectors that start from the reconstructed shower start point or reconstructed vertex (for track object) and end at different physical points of the detector geometry as described below:
  1. Radial Vector (RV or tRV, where "t" denotes a track-related variable) points to the center of the TPC.
  2. Unit Radial vector is the same radial vector as above, but with its modulus normalized to 1. This is referred to as UR or tUR.
  3. Vertical Vector Y (VY or tVY) points to the plane $y = 0$ and is parallel to the y-axis.
  4. Horizontal Vector X (VX or tVX) points to the plane $x = 128.2$cm and is parallel to the x-axis.
  5. Central axis Vector Z (VZ or tVZ) points to the central axis along the beam direction.
  6. Vector TPC Tip (VTT or tVTT), points to the TPC downstream tip, where the tip is the center of the TPC wall that is furthest away from the beam origin (furthest downstream point from BNB target)

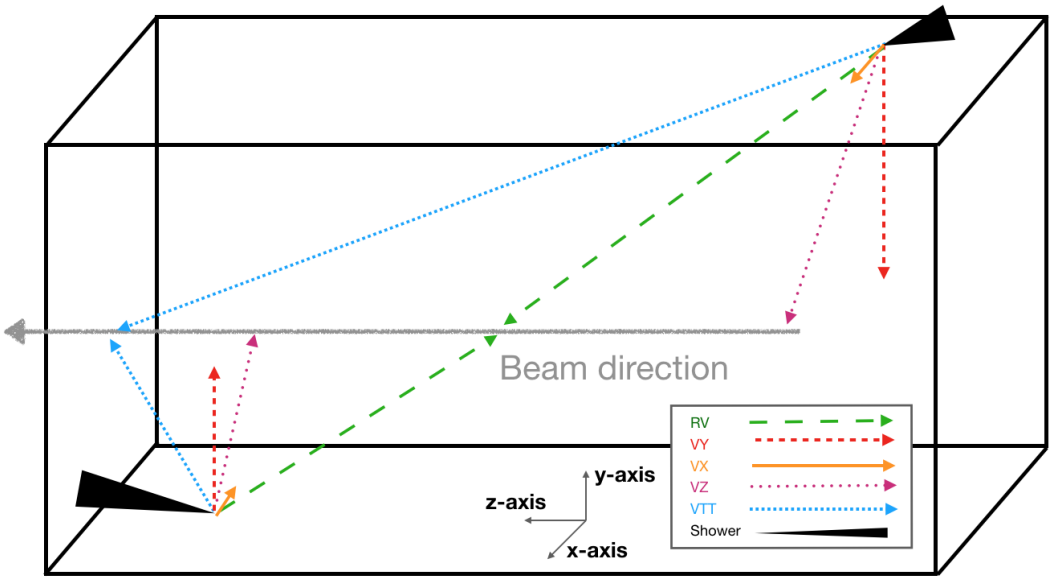

Figure 26: *Examples of RV, VY, VX, VZ, and VTT are shown in this diagram for the case of two different showers reconstructed at different positions in the detector and with different orientations.*

A combination of cuts based on the above variables is applied, after topological selection, to obtain a sample of events with an enhanced dirt fraction. The cuts have been optimized so as to minimize NC Δ radiative events that enter the dirt-enhanced sample, exploiting powerful correlations among different variables, which are different for signal events and dirt events. Examples that illustrate this are provided in Fig. 27.

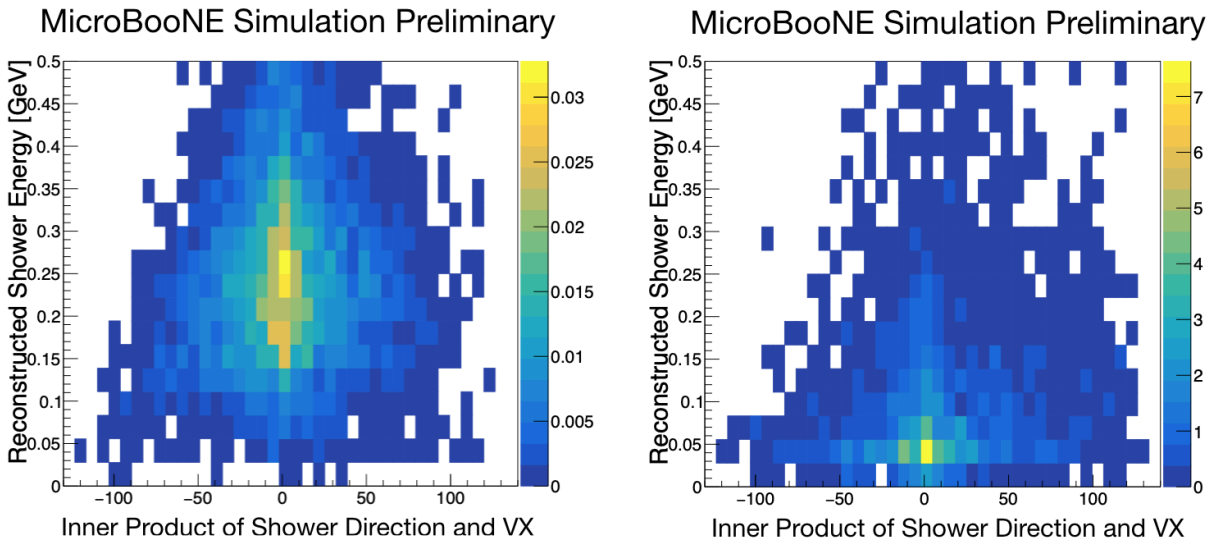

Figure 27: *2D histograms for true NC Δ radiative signal (left) and true dirt (right) events, at $1\gamma 0p$ topological selection stage, illustrating correlations between the VX and reconstructed shower energy variables, used to select a dirt-enhanced sample.*

Figures 28 and 29 show $1\gamma 1p$ and $1\gamma 0p$ event distributions, respectively, before and after the optimized set of dirt-enhancing cuts are applied, both after topological selection stage. As shown in the figures, good data to Monte Carlo agreement is observed, including in regions of small reconstructed distance back to SCB, which is where dirt events contribute most dominantly. This provides confidence that dirt events are well modeled in the Monte Carlo.

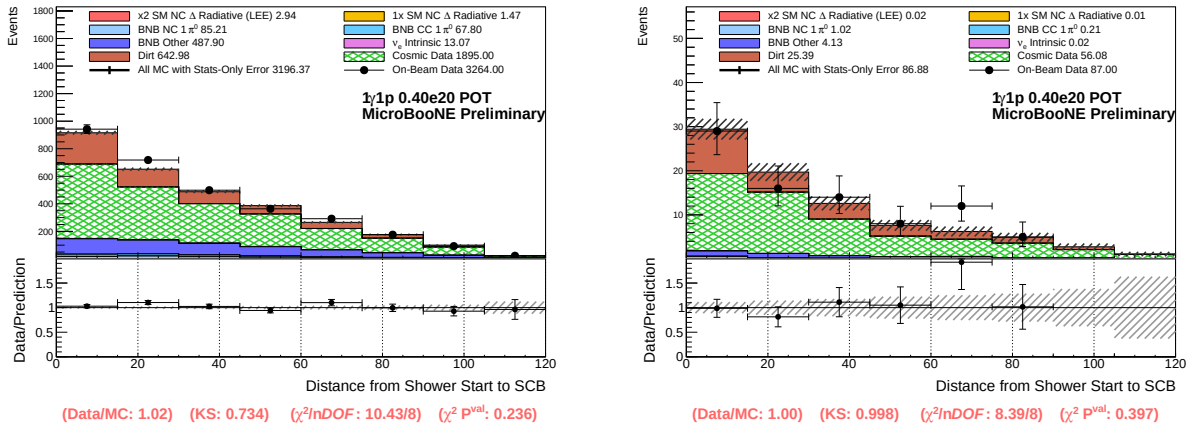

Figure 28: *Distribution of $1\gamma 1p$ topologically-selected events without (left) and with (right) dirt-enhancing cuts applied. Shown are only intrinsic Monte Carlo statistical uncertainties.*

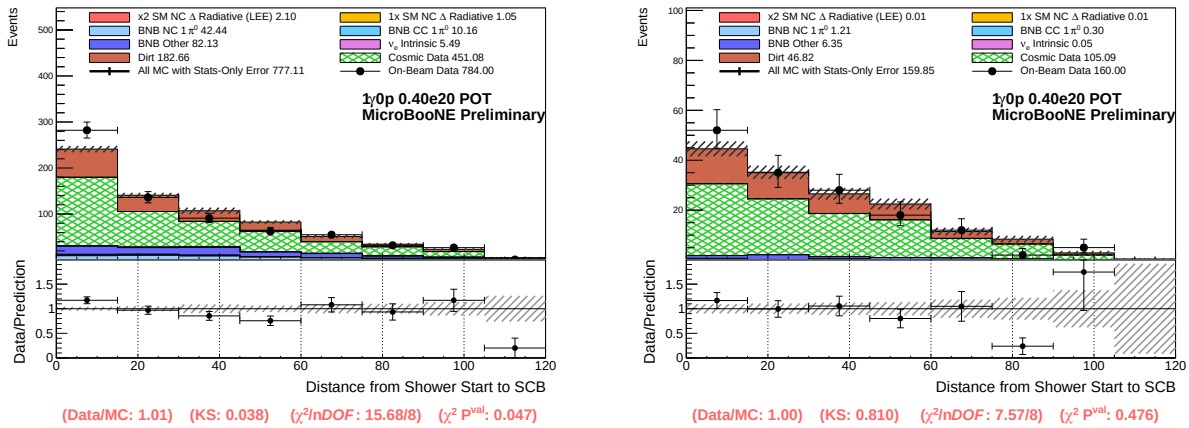

Figure 29: *Distribution of* $1\gamma 0p$ *topologically-selected events without (left) and with (right) dirt-enhancing cuts applied. Shown are only intrinsic Monte Carlo statistical uncertainties.*

4 NC π^0 Selection for In Situ Constraint

It is very clear from the results of the single shower selections that NC π^0 are by far the most dominant background to the NC Δ radiative decay search. In order to ensure that our simulation of these is reliable and validate the predictions of the NC π^0 background to the 1γ selections, a dedicated $2\gamma 1p$ and $2\gamma 0p$ measurement has been performed, providing access to a high-purity, high-statistics sample of NC π^0 events. In addition to this, the high-statistics NC π^0 sample can constrain the exact rate of expected π^0 events and allow us to perform a combined single-photon and NC π^0 fit in order to reduce the systematic uncertainty on the NC π^0 background flux and cross-section.

Through the dedicated $2\gamma 1p$ and $2\gamma 0p$ selections, described in the following subsections, we find that the data is inconsistent with the GENIE central value prediction for NC π^0 production, at the level of $\sim 20\%$, consistent with GENIE cross-section normalization uncertainty. This has led us to perform a data-driven correction to the coherent and non-coherent NC π^0 rate normalizations, as described in Sec. 6.

4.1 Event Selection

The first stage of selection for both the 2γ1p and 2γ0p selections consists of initial topological and low-level pre-selection cuts that are run over MicroBooNE data. This stage eliminates sufficient NC Δ signal events so blindness is maintained. This is accomplished via the use of dedicated filters, providing a total of $\sim 5.8 \times 10^{20}$ POT available for further study. The $2\gamma 1p$ filter and pre-selection consists of six total cuts,

- The reconstructed event topology consists of two showers and one track.
- The conversion distances for both showers is greater than 1 cm.
- The reconstructed neutrino vertex is at least 5 cm away from any TPC wall.
- The reconstructed leading shower energy is > 30 MeV.
- The reconstructed subleading shower energy is > 20 MeV.
- The 3D distance between the event vertex and the track starting point is < 10 cm. For events with a proton track, we expect the vertex to be within a few centimeters of the track start point.

As with the $2\gamma 0p$ we no longer have a proton candidate track from which to calculate variables such as the conversion distance, the pre-selection cuts are instead defined with a simpler subset of cuts, alongside the different topology:

- The reconstructed event topology consists of two showers and zero tracks
- The reconstructed leading shower energy is > 30 MeV.
- The reconstructed subleading shower energy is > 20 MeV.
- The reconstructed neutrino vertex is at least 5 cm away from any TPC wall.

Data to Monte Carlo comparisons of the selections after these initial pre-selection cuts can be found in Fig. 30. We show the reconstructed invariant mass of the two photons, which for true NC π^0 events should peak at the π^0 mass of 135 MeV. As can be seen, even at this stage, the majority of events do contain a CC or NC π^0. However, as we are specifically targeting NC π^0 events, the remaining cosmic contaminated events, as well as the CC π^0, need to be further rejected.

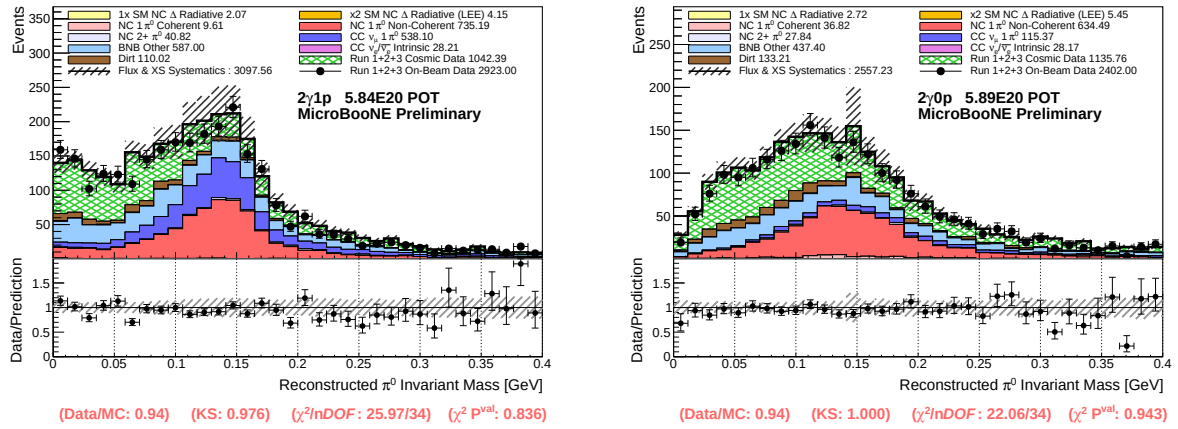

(a) $2\gamma 1p$ *Selection*

(b) $2\gamma 0p$ *Selection*

Figure 30: *The invariant mass of the reconstructed NC* π^0 *sample for both the* $2\gamma 1p$ *and* $2\gamma 0p$ *selections, after pre-selection cuts. At this stage, while* π^0 *(CC and NC combined) make up the largest single contribution of the* $2\gamma 1p$*, there is still a significant amount of cosmic events that are selected. For* $2\gamma 0p$*, the situation is different as the demand of no track like objects removes almost all CC* π^0 *(which often has a long muon track), leaving the NC* π^0 *as the largest BNB driven contribution. Note: detector systematic uncertainties have been evaluated but are omitted in these distributions.*

4.2 BDT Training

In order to reject the remaining backgrounds, a boosted decision tree (BDT) is trained to select NC π^0 events by utilizing a set of 10 calormetric and geometric variables in the $2\gamma 1p$ π^0 selection:

- Leading and subleading shower conversion distances.
- Leading and subleading shower impact parameters. The impact parameter is the distance of closest approach between the back-projection of the reconstructed shower direction and the neutrino interaction candidate.
- Reconstructed leading shower energy (taken as the maximum value among the three wire planes).
- Reconstructed track length.
- Reconstructed track angle θ_{yz}.
- Distance from track end point to nearest TPC wall in 3D.
- Track mean dE/dx over the whole track.
- Ratio of track end-half dE/dx to track start-half dE/dx. This variable helps select stopping protons.

See Fig. 31 for an example of the separation power of one of the more powerful BDT variables, the track mean dE/dx variable, for selecting highly ionizing protons over both cosmic and BNB ν_μ CC. The resulting BDT response can be seen in Fig. 32a, with the NC π^0 piling up on the right (note that the small amount of signal on the left hand side tends to be cosmic contaminated events). A cut at 0.854 maximizes NC π^0 efficiency times purity.

The analogous training variables for the $2\gamma 0p$ NC π^0 selection BDT must be somewhat modified as we no longer have a track like-object with which to reject cosmic muons and ν_μ CC events. The 10 variables utilized are:

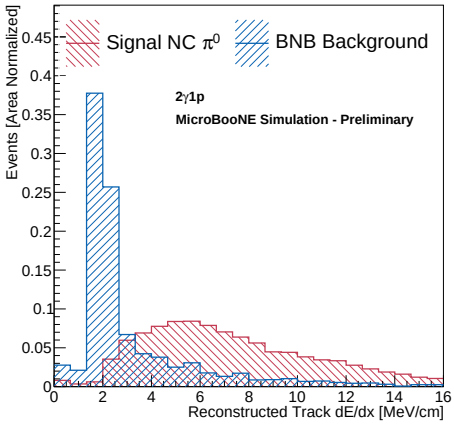

(a) MC-only Distributions (area normalized)

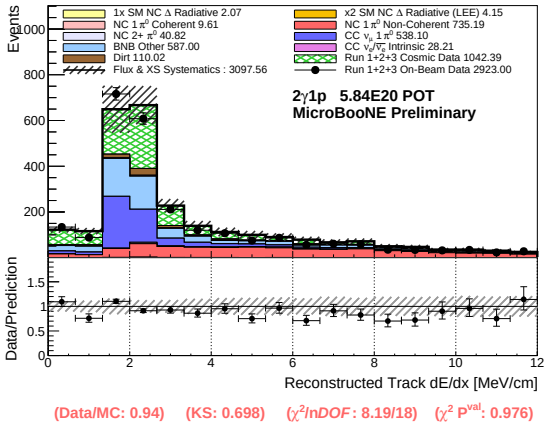

(b) Data and MC Distributions

Figure 31: *(a) Monte Carlo predicted distribution of reconstructed track (mean truncated) dE/dx, separated between signal and BNB backgrounds. (b) Data to Monte Carlo distribution comparison for the same variable. Note: detector systematic uncertainties have been evaluated but are omitted in these distributions.*

- Both shower conversion distances
- Both shower impact parameters.
- Both shower energies (maximum among the three wire planes).
- Both ratios of shower length to shower energy.
- Leading shower θ_{yz}.
- Neutrino score of the slice containing the leading shower.

with the resulting BDT response shown in Fig. 32. A cut at 0.95 maximizes the purity times efficiency of the selected NC π^0 events.

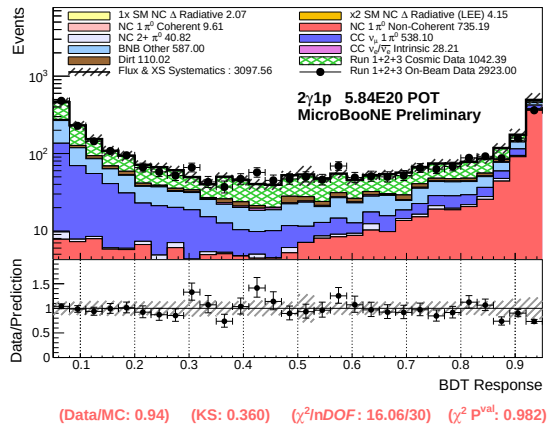

(a) $2\gamma 1p$ *BDT response*

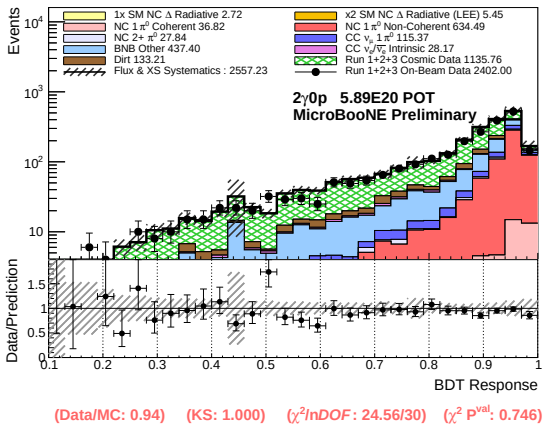

(b) $2\gamma 0p$ *BDT response*

Figure 32: *Data to Monte Carlo comparisons for the* $2\gamma 1p$ *BDT response (left). To maximize efficiency times purity in the final selection, we place a cut on this distribution at 0.854. Shown on the right is the Data to Monte Carlo comparison for the* $2\gamma 0p$ *BDT response, where to maximize efficiency times purity, we place a cut on this distribution at 0.950. Note: detector systematic uncertainties have been evaluated but are omitted in these distributions.*

4.3 Final Selection

Figure 33a shows the final reconstructed π^0 invariant mass of the $2\gamma 1p$ selection. A Gaussian fit to the data points gives a mean of 137.6 ± 2.1 MeV with a width of 44.4 ± 1.8 MeV, summarized in Tab. 6. Figure 34a shows the π^0 momentum, while the reconstructed cosine of the center-of-mass (CM) decay angle is shown in Fig. 34b. This is defined as the angle between the lab-frame π^0 momentum direction and the single photon which has the smallest opening angle w.r.t the π^0 boost direction as calculated in the center of mass (CM) frame. In theory, this quantity should give a flat distribution for signal events, but in reality we see some tapering off at high $\cos(\theta_{cm})$, corresponding to more asymmetric π^0 decays. This is expected, as we are likely to miss the subleading photon shower in highly asymmetric decays. Overall there is a $\approx 20\%$ deficit in observed events in the final selection, which is relatively flat in the observed variables. Although large, this is mostly within the flux and cross-section uncertainties of the NC π^0 production rate. It does, however, suggest that the GENIE central value for NC π^0 production may be too high, motivating the possibility of fitting the rate to the observed data, as is discussed in Sec. 6.

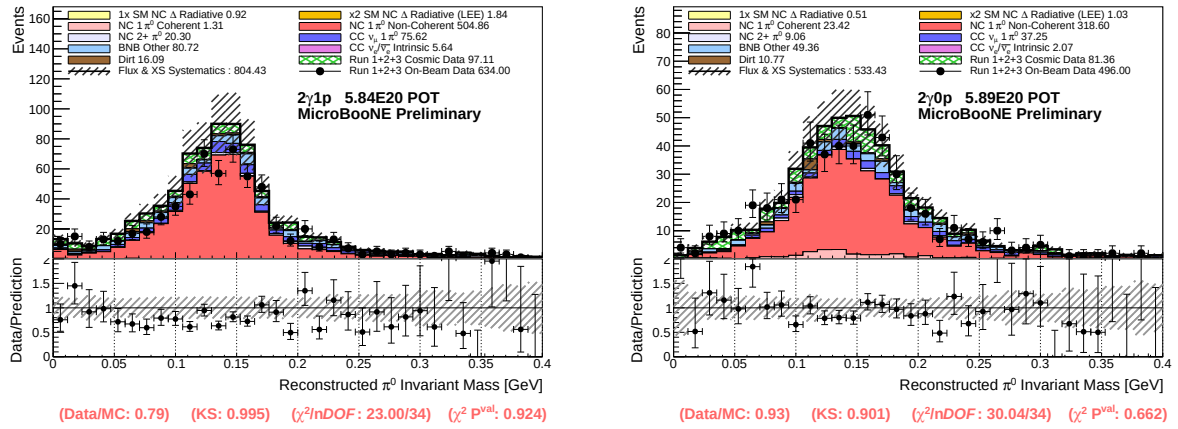

(a) $2\gamma 1p$ ***(b)*** $2\gamma 0p$

Figure 33: *Reconstructed π^0 mass distributions for (a) $2\gamma 1p$ and (b) $2\gamma 0p$. The distributions show predictions scaled to 5.85×10^{20} POT, which correspond to the total POT for filtered Runs 1-3, and corresponding data. These distributions correspond to the GENIE central value (CV) prediction, i.e. no normalization correction has been applied to the NC π^0 production (see Sec. for details on the referenced correction). Note: detector systematic uncertainties have been evaluated but are omitted in these distributions.*

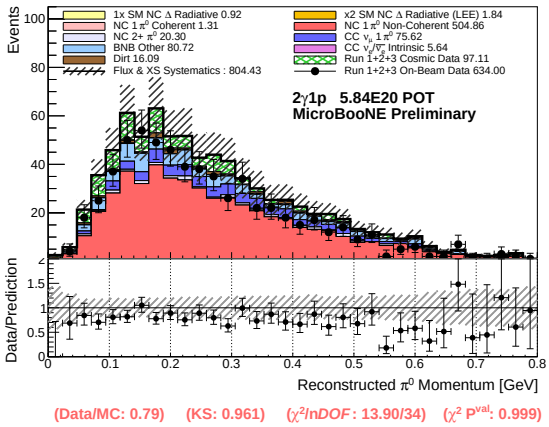

(Data/MC: 0.79) (KS: 0.961) (χ^2/nDOF: 13.90/34) (χ^2 P^{val}: 0.999)

(a) *π^0 Momentum*

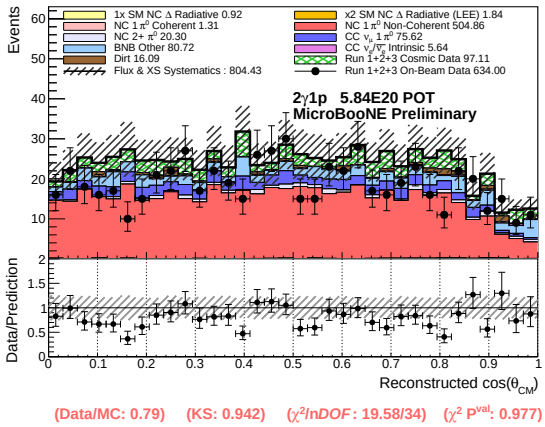

(Data/MC: 0.79) (KS: 0.942) (χ^2/nDOF: 19.58/34) (χ^2 P^{val}: 0.977)

(b) $\cos(\theta_{cm})$

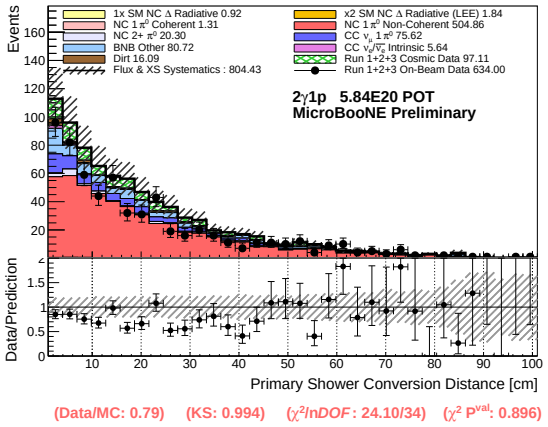

(Data/MC: 0.79) (KS: 0.994) (χ^2/nDOF: 24.10/34) (χ^2 P^{val}: 0.896)

(c) *Leading Shower Conversion Distance*

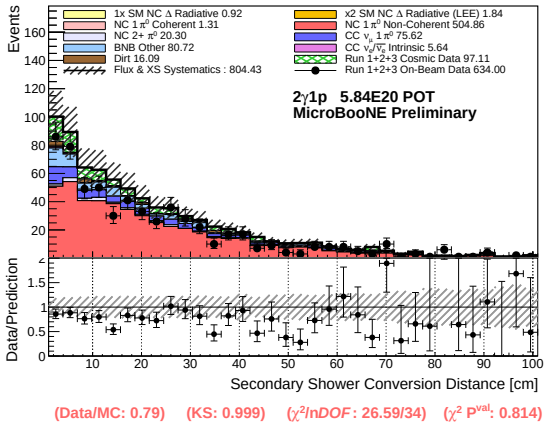

(Data/MC: 0.79) (KS: 0.999) (χ^2/nDOF: 26.59/34) (χ^2 P^{val}: 0.814)

(d) *Subleading Shower Conversion Distance*

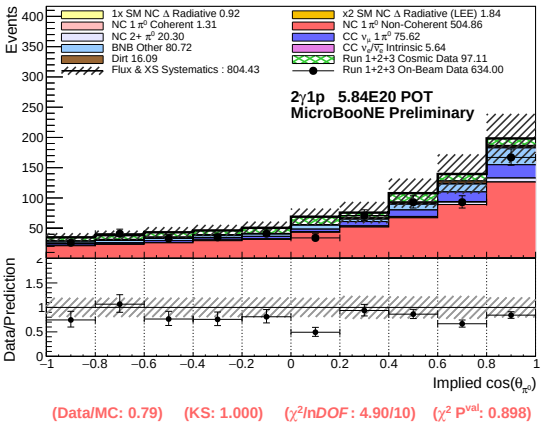

(Data/MC: 0.79) (KS: 1.000) (χ^2/nDOF: 4.90/10) (χ^2 P^{val}: 0.898)

(e) *Implied $\cos\theta_\pi$*

Figure 34: *Some select Data to Monte Carlo comparisons for the $2\gamma1p$ final selection. Uncertainties shown include all flux and cross-section systematics. Shape agreement is good across all variables, with an overall $\sim$20% discrepancy in data that is on the lower edge of the 1σ flux and cross-section systematic error band. Note: detector systematic uncertainties have been evaluated but are omitted in these distributions.*

Table 4 breaks down the signal events in the $2\gamma 1p$ final selection in terms of interaction type. As expected, the majority of selected events are resonant. Deep inelastic scatterig (DIS) events comprise ∼10% of the selection, while quasi-elastic, coherent, and meson exchange current (MEC) events each account for ∼1% or less of the final selection.

Finally, Figs. 37 and 36 show two example event display of a candidate NC π^0 interaction that passes the final $2\gamma 1p$ selection.

	Resonant	**DIS**	**QE**	**Coherent**	**MEC**
Pre-Selection	81.3%	16.3%	1.3%	1.31%	0.06%
Final Selection	85.2%	13.2%	1.2%	0.28%	0.07%

Table 4: *Breakdown of interaction types in the $2\gamma 1p$ selection, both at the pre-selection stage and final selection stage.*

Final selection distributions for $2\gamma 0p$ are shown in Fig 35. Unlike in the $2\gamma 1p$ case, the data to Monte Carlo normalization difference is less than 10%, within flux and cross-section uncertainties. The $2\gamma 0p$ selection is 64.1% pure and 41.6% efficient in NC π^0 events, relative to the topological selection. A Gaussian fit to the data points in the invariant mass distribution gives a mean of 140.2 ± 2.8 MeV and a width of 49.9 ± 2.7 MeV, summarized in Tab. 5. A breakdown of interaction types at the pre-selection stage, and final selection stage can be seen in Tab. 5.

	Resonant	**DIS**	**QE**	**Coherent**	**MEC**
Pre-Selection	79.1%	14.9%	0.52%	5.5%	0.02%
Final Selection	79.2%	13.5%	0.45%	6.8%	0.00%

Table 5: *Breakdown of interaction types in the $2\gamma 0p$ NC π^0 selection, both at the pre-selection stage and final selection stage.*

Selection	**Fit Mean (MeV)**	**Fit Width (MeV)**	**Fit Resolution (%)**
$\mathbf{2\gamma 1p}$	137.6 ± 2.1	44.4 ± 1.8	32.2 ± 5.7
$\mathbf{2\gamma 0p}$	140.2 ± 2.8	49.9 ± 2.7	35.6 ± 5.7

Table 6: *Gaussian fit parameters for the $2\gamma 1p$ and $2\gamma 0p$ Run 1-3 selections, using the $2\gamma 1p$ and $2\gamma 0p$ filtered data sets.*

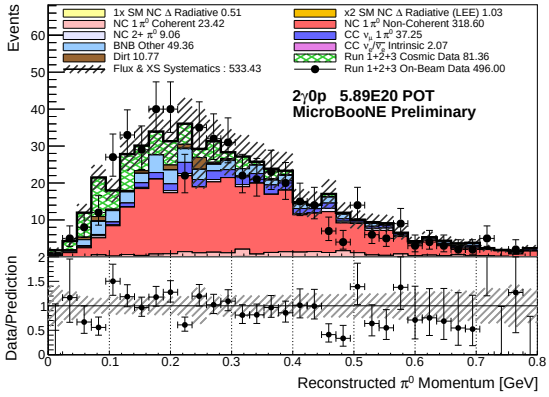

(Data/MC: 0.93) (KS: 0.437) (χ^2/nDOF: 31.16/34) (χ^2 P^{val}: 0.608)

(a) π^0 *Momentum*

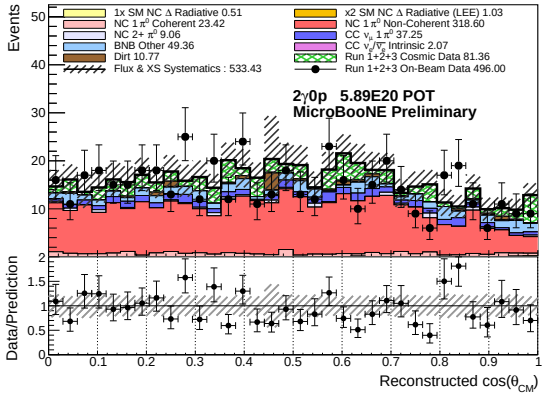

(Data/MC: 0.93) (KS: 0.550) (χ^2/nDOF: 31.78/34) (χ^2 P^{val}: 0.577)

(b) $\cos(\theta_{cm})$

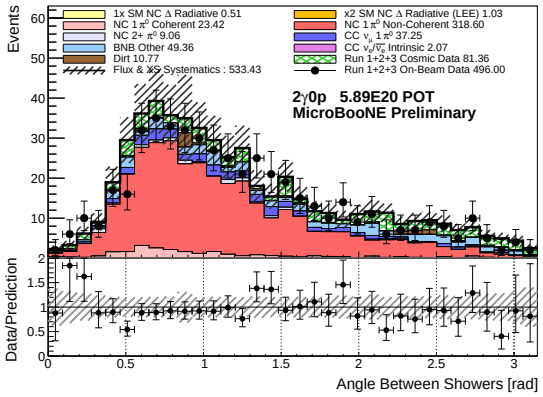

(Data/MC: 0.93) (KS: 0.996) (χ^2/nDOF: 16.25/34) (χ^2 P^{val}: 0.996)

(c) *Angle Between Showers*

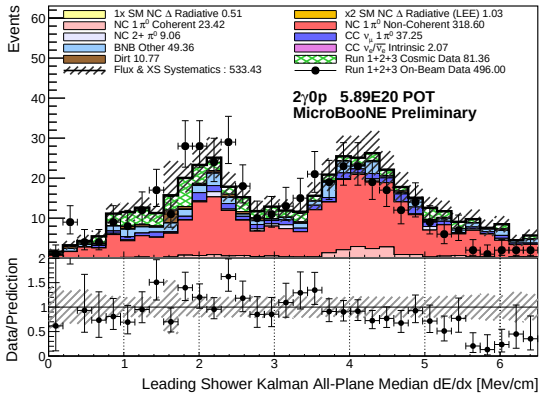

(Data/MC: 0.93) (KS: 0.006) (χ^2/nDOF: 40.55/34) (χ^2 P^{val}: 0.204)

(d) *Leading Photon dE/dx*

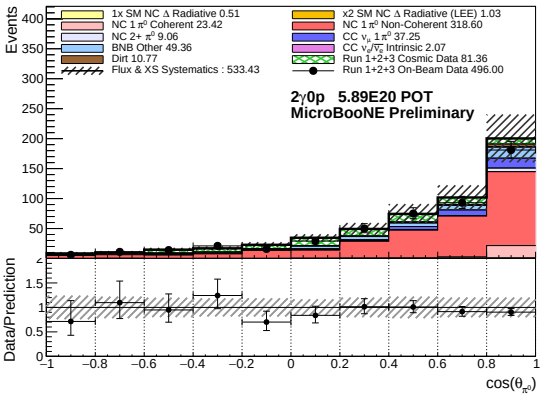

(Data/MC: 0.93) (KS: 1.000) (χ^2/nDOF: 2.74/10) (χ^2 P^{val}: 0.987)

(e) $\cos\theta_\pi$

Figure 35: *Some select Data to Monte Carlo comparisons for the* $2\gamma0p$ *final selection. Agreement is reasonable across all variables, within flux and GENIE cross-section uncertainties. Note: detector systematic uncertainties have been evaluated but are omitted in these distributions.*

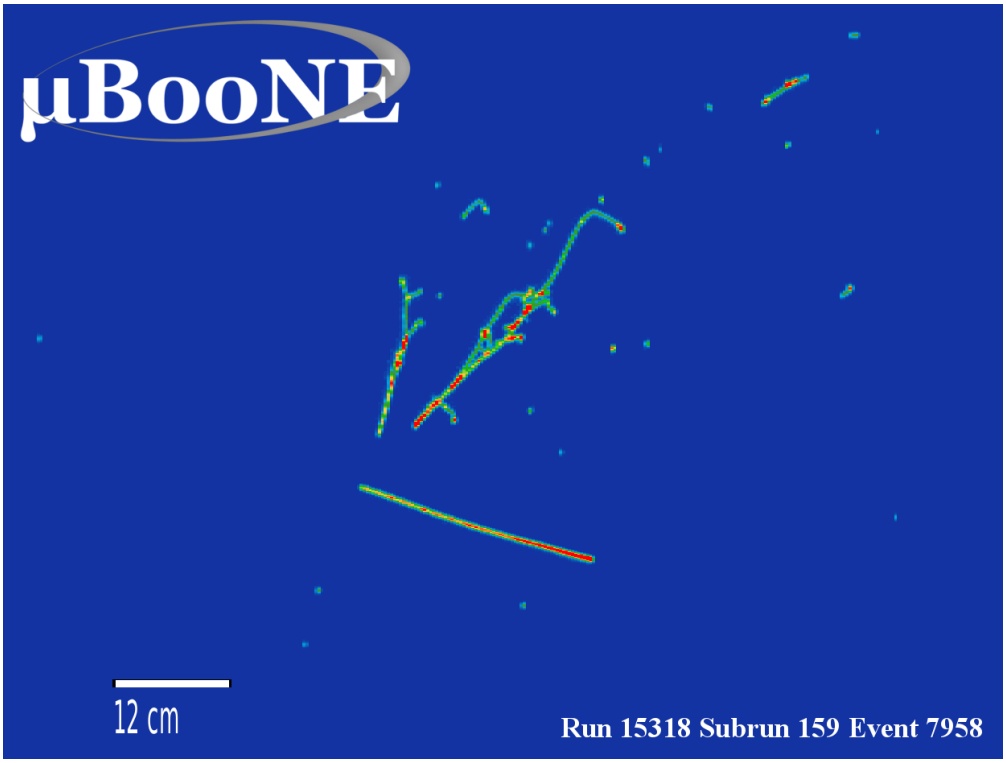

Figure 36: *Event display for an NC π^0 candidate event which survives the final $2\gamma 1p$ selection, recorded during Run 3 of MicroBooNE. Leading shower energy was reconstructed as 332 MeV with a subleading shower energy of 98 MeV, and a corresponding invariant mass of 158.2 MeV.*

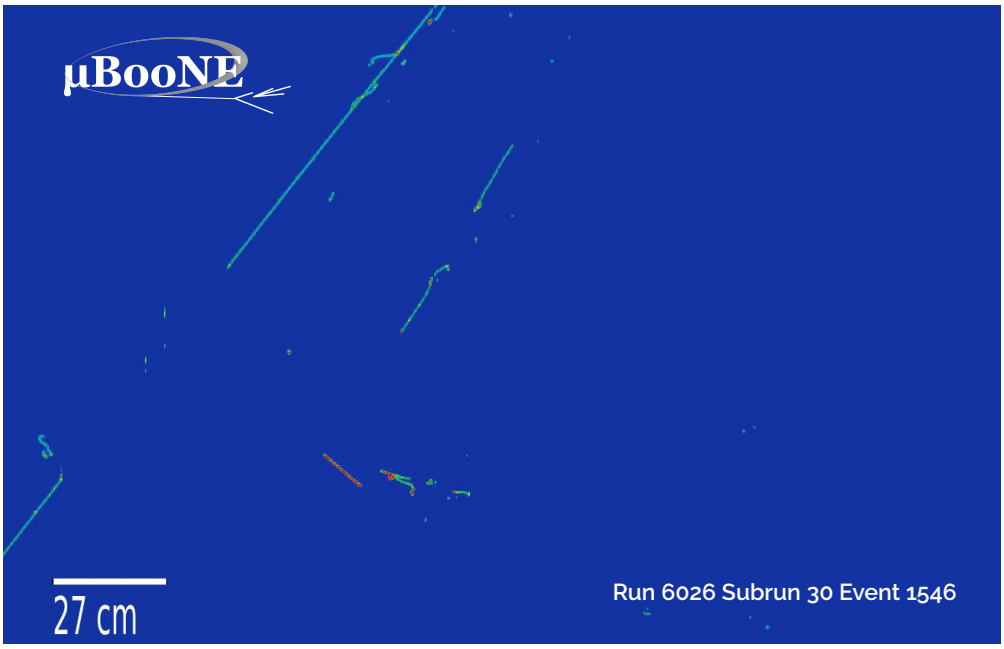

Figure 37: *Event display for an NC π^0 candidate event which survives the final $2\gamma 1p$ selection, recorded during Run 1of MicroBooNE. The reconstructed invariant mass is 146.2 MeV.*

5 Evaluation of Systematic Uncertainties

The systematic uncertainties taken into account in this analysis can be grouped into three categories:

1. Re-weightable BNB flux uncertainties
2. Re-weightable neutrino cross-section and interaction GENIE uncertainties
3. Detector systematic uncertainties

Both the flux and cross-section uncertainties are estimated using re-weighting in which the central value (CV) Monte Carlo events are assigned weights that scale and shift the events depending on some underlying systematic variation. We construct an individual covariance matrix M^k corresponding to each one of the underlying sources of systematic uncertainty we are studying, k. To construct this matrix we consider a large number (N, usually > 100) separate varied distributions V_n^k of the final selected $1\gamma 1p$, $1\gamma 0p$, $2\gamma 1p$ and $2\gamma 0p$ spectra, where $n = 1, .., N$. The varied distributions are calculated each time by varying the underlying source of uncertainty k within its associated error band, and re-weighting the CV spectra according to a corresponding pre-parameterized shift. The deviations of those varied distributions relative to the central value prediction, P, are then mapped onto the covariance matrix, constructed from the distributions as follows:

$$M_{ij}^k = \frac{1}{N}\sum_{n=1}^{N}(P_i - V_{i,n}^k) \times (P_j - V_{j,n}^k), \tag{1}$$

where i, j are bin numbers. The total covariance matrix encompassing all these uncertainties is then the linear sum of the covariance matricies for all individual systematic variations, k, under investigation.

5.1 Flux and Cross-section Systematic Uncertainties

We use "event reweighting" as the basis of evaluation of flux and cross-section systematic uncertainties. The approach is to consider a given physics parameter P that goes into our simulation and create a random or Gaussian fluctuation x_p such that changing this parameter changes P into P' as follows:

$$P \to P' = P(1 + x_p * (\delta P/P)), \tag{2}$$

where δP is the standard deviation of P [15]. P can be a configurable parameter or a function or any prediction. In the case of cross-section uncertainties, instead of re-simulating entire samples with this new parameter P', the GENIE response is predicted for each generated event and events are assigned a new weight based on whether the change increases or decreases their likelihood of occurring. Each variation knob has a calculator that estimates this (knob being the term referring to a variation parameter). The MicroBooNE flux [16] and GENIE [15] technical notes provide more details. This method has a limitation in that events cannot be weighted into existence, but sufficiently large in statistics simulated samples should negate this, and this method is optimal given limited allocated computing resources.

The covariance matrices generated via reweighting make use of the final selections for $2\gamma 1p$, $2\gamma 0p$, $1\gamma 1p$, and $1\gamma 0p$, from previous sections. For systematics evaluation, 41 parameters of underlying neutrino interaction uncertainties in GENIE are studied together, alongside 13 systematic effects coming from the BNB flux modeling.

The flux systematics included in the analysis are listed and described in Tab. 7. Two dominant systematics for the analysis are skin depth and π^+ production. The skin-depth flux unisim refers to the effect of time varying electric currents penetrating into the horn conductor. In the case of π^+ production, the majority of neutrino flux at MicroBooNE comes from π^+ production in proton-Be target interactions. As this affects the majority of events in final selection, this source of uncertainty is necessarily an important one for all our signal and backgrounds. The effect of π^+ production variations on the NC π^0 non-coherent component of the 2γ and 1γ final selected samples is illustrated in Figs. 39 and 38, respectively.

Variation Label	Description
expskin_FluxUnisim	Skin Depth for electric currents penetrating conductor
horncurrent_FluxUnisim	Horn Current in magnetic focusing horn
kminus_PrimaryHadronNormalization	K^- Production Normalization
kplus_PrimaryHadronFeynmanScaling	K^+ Sanford Wang Central Spline Variation
kzero_PrimaryHadronSanfordWang	K^0 Sanford Wang
nucleoninexsec_FluxUnisim	Nucleon Total Inelastic Cross-section on Be
nucleonqexsec_FluxUnisim	Nucleon Total Quasi-elastic Cross-section on Be
nucleontotxsec_FluxUnisim	Nucleon Total cross-section on Be
piminus_PrimaryHadronSWCentralSplineVariation	π^- Sanford Wang Central Spline Variation
pioninexsec_FluxUnisim	Pion Total Inelastic Cross-section on Be
pionqexsec_FluxUnisim	Pion Total Quasi-elastic Cross-section on Be
piontotxsec_FluxUnisim	Pion Total Cross-section on Be
piplus_PrimaryHadronSWCentralSplineVariation	π^+ Sanford Wang Central Spline Variation

Table 7: *List of sources of flux systematic uncertainties, evaluated using the reweighting method.*

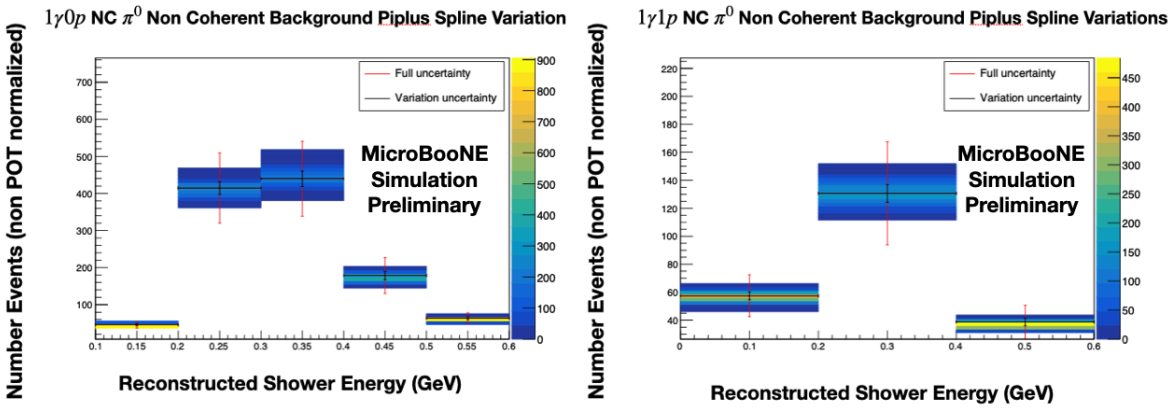

Figure 38: *A variation plot illustrating the central Sanford Wang π^+ flux uncertainty effect on the $NC\pi^0$ non-coherent background in the final $1\gamma1p$ (right) and $1\gamma0p$ (left) selection. The color scale represents the density of "multisims" or reweighted iterations that land in that particular bin thus giving a visual representation of the spread of prediction created by this underlying systematic uncertainty.*

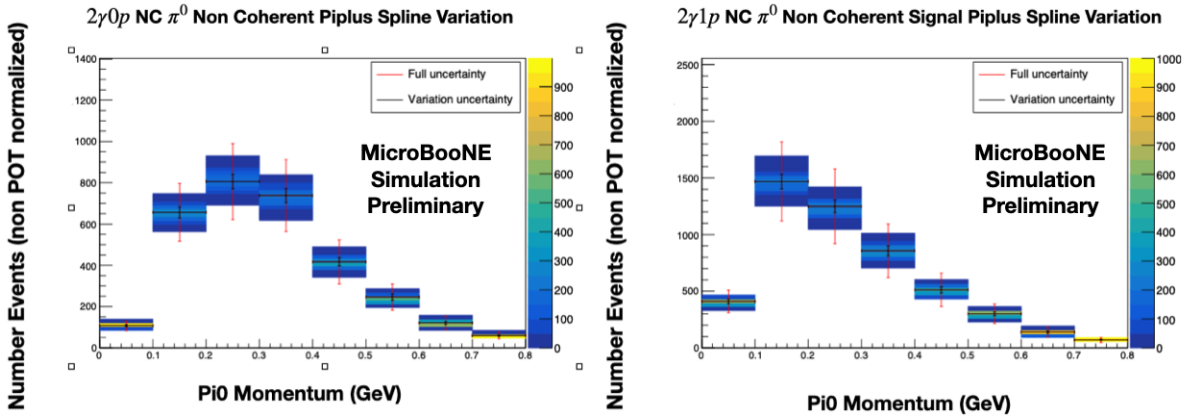

Figure 39: *A variation plot illustrating the central Sanford Wang π^+ flux uncertainty effect on the $NC\pi^0$ non-coherent signal in the final $2\gamma 1p$ (right) and $2\gamma 0p$ (left) selections. The color z scale represents the density of "multisims" or reweighted iterations that land in that particular bin thus giving a visual representation of the spread of prediction created by this underlying systematic uncertainty.*

Cross-section systematics are evaluated using the GENIE reweight package. There are a total of 34 systematics that are defined by a continuous parameter which we study together under the umbrella term "genie_all" to assess their effect in our analysis. The "genie_all" set of variations runs a suite of variations for a number of GENIE systematic knobs simultaneously, accounting for all correlations between the different variations. Table 15 in Appendix A summarizes the sources of (input) GENIE systematic uncertainties. Because "genie_all" accounts for correlations between individual knobs, it is more appropriately used for the calculation of final uncertainties and production of covariance matrices, instead of looking at each variation individually. It is run with 400 total multisims. Nonetheless, it is instructive to study each variation in isolation as well for the purpose of better understanding which underlying systematic uncertainties are the largest for our various selections. The effect of cross-section variations from "genie_all" is illustrated in Fig. 40 and Fig. 41, for the $NC\pi^0$ non-coherent component of the 2γ and 1γ final selection stages, respectively.

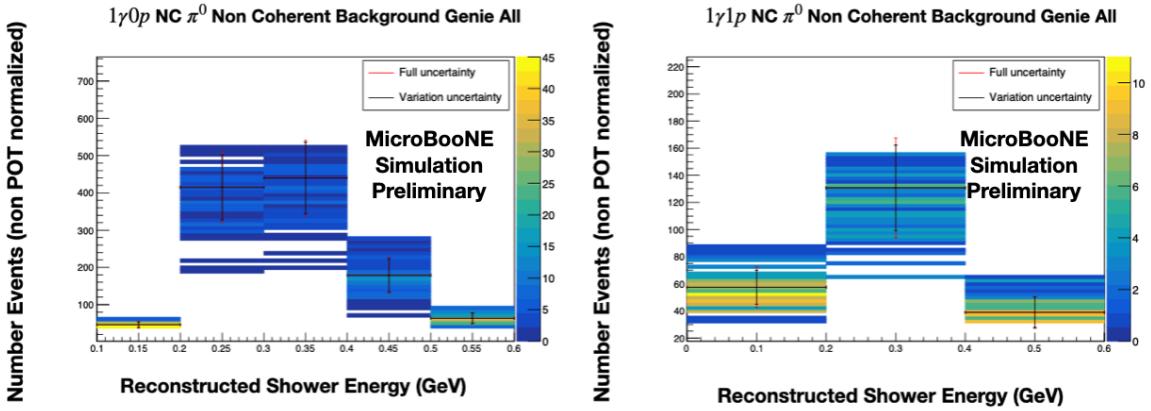

Figure 40: *A variation plot illustrating the "genie_all" uncertainties' effect on the $NC\pi^0$ non-coherent component in the final 1γ selections. The color z scale represents the density of "multisims" or reweighted iterations that land in that particular bin thus giving a visual representation of the spread of prediction created by this set of underlying systematic uncertainties.*

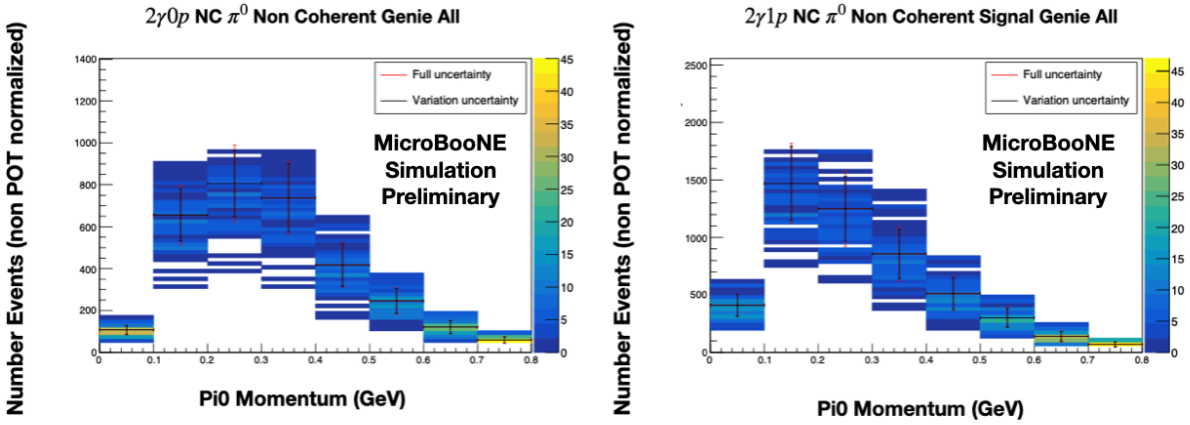

Figure 41: *A variation plot illustrating the "genie_all" uncertainties' effect on the $NC\pi^0$ non coherent component in the final 2γ selections. The color z scale represents the density of "multisims" or reweighted iterations that land in that particular bin thus giving a visual representation of the spread of prediction created by this set of underlying systematic uncertainties.*

Alongside "genie_all", there are an additional seven other cross-section modelling uncertainties whose underlying physics is not defined by continuous parameters, but are more in line with switching between two binary interaction models, and the representative uncertainty is then given by the absolute difference between two extreme ranges (these are referred to as the "min/max" variations. An example of this is "Theta Delta2Npi" knob, which varies the pion angular distribution for $\Delta \rightarrow N\pi$ events between the default Rein-Sehgal model and an isotropic distribution, with the full difference being the uncertainty. The fractional covariance and correlation matrices constructed for all four samples ($2\gamma 1p$, $2\gamma 0p$, $1\gamma 1p$, and $1\gamma 0p$) for "genie_all" are shown in Figs. 42 and 43, respectively.

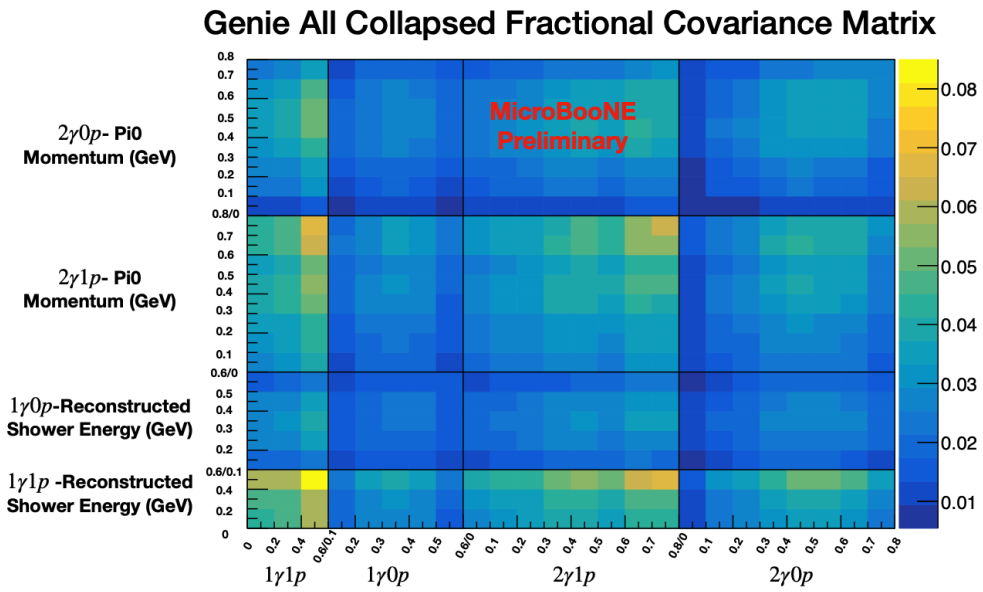

Figure 42: *The fractional covariance matrix for "genie_all" cross-section systematic uncertainties, constructed for the four final selected samples side by side. The "genie_all" covariance matrix more properly accounts for correlations among different systematic knobs. The single-photon samples are each binned in 5 and 3 bins of shower energy, for $1\gamma 0p$ and $1\gamma 1p$, respectively, and the NC π^0 samples are each binned in 8 bins of NC π^0 momentum.*

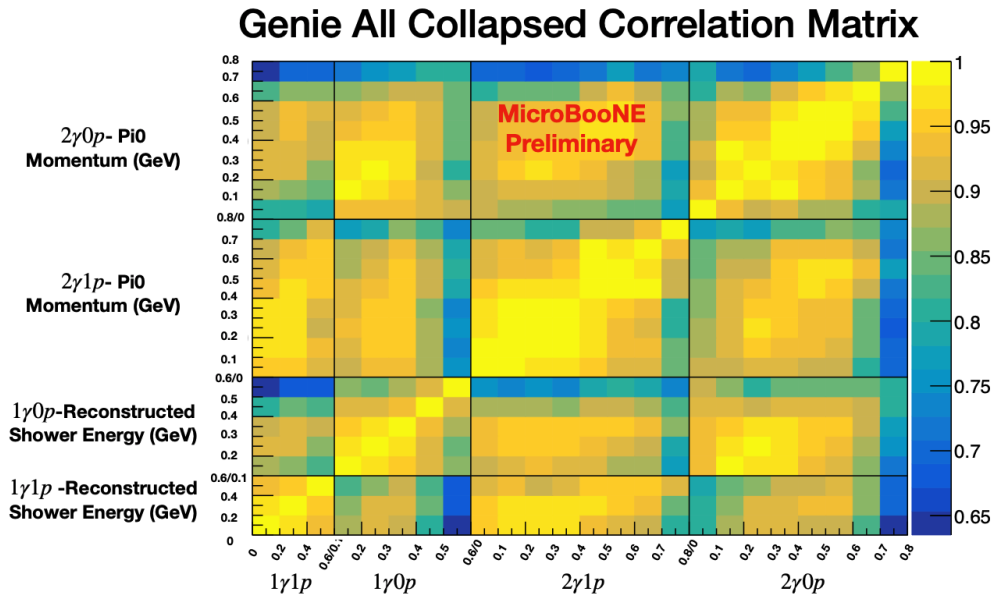

Figure 43: *The correlation matrix for "genie_all" cross-section systematic uncertainties, constructed for the four final selected samples side by side. The "genie_all" correlation matrix properly accounts for correlations among different systematic knobs. The single-photon samples are each binned in 5 and 3 bins of shower energy, for* $1\gamma 0p$ *and* $1\gamma 1p$*, respectively, and the NC* π^0 *samples are each binned in 8 bins of NC* π^0 *momentum.*

Final covariance and correlation matrices are generated using the combination of "genie_all"; the 7 min/max interaction systematics; flux variations attributed to magnetic focusing horn modeling, BNB proton-target interaction and secondary production and interaction uncertainties. These are used to assess overall uncertainty on our predictions and will ultimately be used for our NC π^0 constraint analysis (see Sec. 6), and final fits. The correlation matrix and fractional covariance matrix for all four final selected samples are provided in Figs. 44 and 45 respectively, constructed using the method described before. The plotted variables and binning were chosen to optimize the constraint analysis described in Sec. 6.

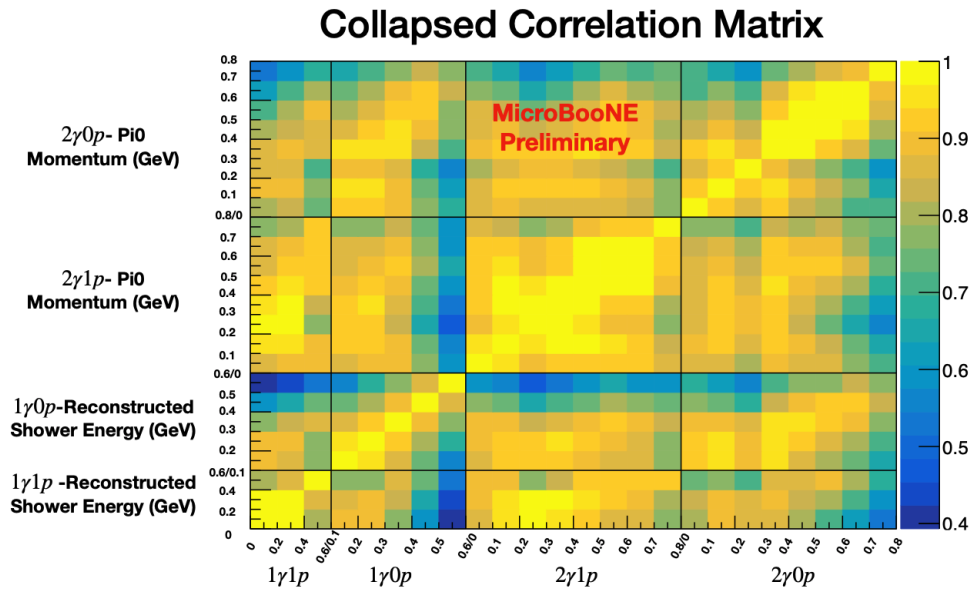

Figure 44: *The correlation matrix for combined cross-section and flux systematics. The single-photon samples are each binned in 5 and 3 bins of shower energy, for* $1\gamma0p$ *and* $1\gamma1p$*, respectively, and the NC* π^0 *samples are each binned in 8 bins of NC* π^0 *momentum.*

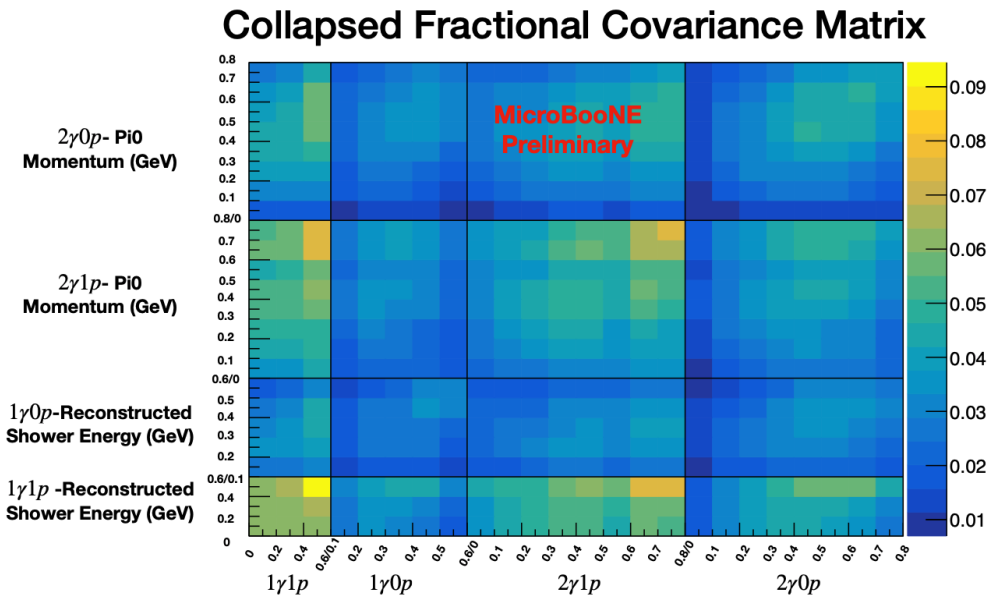

Figure 45: *The fractional covariance matrix for combined cross-section and flux systematics. The single-photon samples are each binned in 5 and 3 bins of shower energy, for* $1\gamma 0p$ *and* $1\gamma 1p$*, respectively, and the NC* π^0 *samples are each binned in 8 bins of NC* π^0 *momentum.*

An estimation of the level of constraint on the uncertainty of the final $1\gamma 1p$ signal measurement can be evaluated using the method described in Ref. [17], by considering the NC π^0 sideband ($2\gamma 1p$) measurement, in a way analogous to how one can constrain ν_e backgrounds using observed ν_μ events in the MiniBooNE or MicroBooNE experiments.

The procedure is as follows: one begins with the total covariance matrix containing statistical and systematic uncertainties (and correlations) for both the 1γ samples (signal and background) and the 2γ signal and background samples:M_{ij}. The matrix is inverted, yielding M_{ij}^{-1}. Given an assumed statistical error on the measured NC π^0 ($2\gamma 1p$ and $20p$) rates, per bin i, given by $\sigma_i^{\text{data}} = \sqrt{N_i^{\text{data}}}$, and assuming that the number of observed data events is equivalent to that of the Monte Carlo, $N_i^{\text{data}} = N_i^{MC}$, we then add the inverted statistical error to the diagonal of the 2γ portion of the inverted matrix, i.e. $(M_{ij}^{-1})^{new} = M_{ij}^{-1} + \delta_{ij}/N_i^{MC}$. After this step, the matrix is re-inverted and this leads to new uncertainties on 1γ samples, which are reduced, relative to the original. Those uncertainties are referred to as "constrained" uncertainties. The level of constraint (i.e. the level of uncertainty reduction) grows with increased $2\gamma 1p$ and $20p$ statistics.

Systematic uncertainties of 25% in the 1γ channels are reduced to under 8% after the 2γ constraint is applied. Further details can be found in Tabs. 8 and 9 which show uncertainties on the total predicted $1\gamma 1p$ and $1\gamma 0p$ samples broken down by each individual systematic uncertainty. This allows us to probe which underlying uncertainties are being constrained and which are not being aided by the 2γ sideband. The level of constraint evaluated using this method suggests one should expect a promising reduction of the systematic uncertainty on the background components of $1\gamma 1p$ and $1\gamma 0p$ samples, which are highly correlated with the $2\gamma 1p$ and $2\gamma 0p$ samples. In all tables, the $2\gamma 1p$ and $2\gamma 0p$ are used to constrain the 1γ samples simultaneously in unison, which is of particular importance as the $1p$ selections are largely insensitive to NC π^0 coherent events.

Variation Name	**Unconstrained Error** $1\gamma 1p$	**Constrained Error** $1\gamma 1p$	**Reduction Factor** $1\gamma 1p$	**Unconstrained Error** $1\gamma 0p$	**Constrained Error** $1\gamma 0p$	**Reduction Factor** $1\gamma 0p$
expskin_FluxUnisim	4.93%	3.41%	1.45	4.01%	2.77%	1.45
horncurrent_FluxUnisim	0.69%	0.68%	1.01	0.54%	0.53%	1.01
π^+ SW CV Spline Var	4.51%	3.23%	1.40	3.86%	2.76%	1.40
π^- SW CV Spline Var	-	-	1.00	0.16%	0.16%	1.00
K^+ FeynmanScaling	0.46%	0.46%	1.00	0.55%	0.55%	1.00
K^0 SanfordWang	0.16%	0.16%	1.00	0.27%	0.27%	1.00
K^- Normalization	-	-	-	-	-	-
nucleoninexsec_FluxUnisim	0.83%	0.82%	1.02	0.77%	0.76%	1.02
nucleonqexsec_FluxUnisim	2.49%	2.17%	1.14	2.37%	2.07%	1.14
nucleontotxsec_FluxUnisim	0.73%	0.72%	1.01	0.66%	0.65%	1.01
pioninexsec_FluxUnisim	1.25%	1.20%	1.04	1.06%	1.02%	1.04
pionqexsec_FluxUnisim	0.84%	0.83%	1.02	0.74%	0.73%	1.02
piontotxsec_FluxUnisim	0.88%	0.86%	1.02	0.78%	0.76%	1.02

Table 8: *Unconstrained and constrained flux uncertainties, broken down by systematic uncertainty source, for the* $1\gamma 1p$ *and* $1\gamma 0p$ *total background predictions. A - value indicates no uncertainty.*

Variation Name	**Unconstrained Error** $1\gamma1p$	**Constrained Error** $1\gamma1p$	**Reduction Factor** $1\gamma1p$	**Unconstrained Error** $1\gamma0p$	**Constrained Error** $1\gamma0p$	**Reduction Factor** $1\gamma0p$
genie_all	22.64%	7.21%	3.14	13.82%	4.48%	3.09
AGKYpT1pi	0.43%	0.43%	1.00	0.36%	0.36%	1.00
AGKYxF1pi	0.34%	0.34%	1.00	0.18%	0.18%	1.01
AhtBY	0.00%	0.00%	1.00	0.23%	0.23%	1.00
BhtBY_UBGenie	0.01%	0.01%	1.00	0.23%	0.23%	1.00
CV1uBY	0.03%	0.03%	1.00	0.23%	0.23%	1.00
CV2uBY_UBGenie	0.03%	0.03%	1.00	0.23%	0.23%	1.00
CoulombCCQE	0.03%	0.03%	1.00	0.22%	0.22%	1.00
EtaNCEL	0.02%	0.02%	1.00	0.21%	0.21%	1.00
FrAbs_N_UBGenie	4.91%	3.21%	1.53	4.61%	3.02%	1.53
FrAbs_pi	5.12%	3.26%	1.57	3.33%	2.13%	1.57
FrCEx_N	9.58%	6.69%	1.43	1.58%	1.10%	1.43
FrCEx_pi	9.32%	4.36%	2.14	4.18%	1.96%	2.13
FrInel_N_UBGenie	1.11%	0.74%	1.50	5.39%	3.60%	1.50
FrInel_pi	3.14%	2.78%	1.13	0.30%	0.28%	1.07
FracDelta_CCMEC	0.05%	0.05%	1.00	0.32%	0.32%	1.00
FracPN_CCMEC	0.03%	0.03%	1.00	0.22%	0.22%	1.00
MFP_N	2.47%	2.19%	1.13	1.94%	1.72%	1.13
MFP_pi	1.73%	1.65%	1.05	0.97%	0.93%	1.05
MaCCQE	0.09%	0.09%	1.00	0.34%	0.34%	1.00
MaCCRES	0.66%	0.60%	1.10	2.41%	2.20%	1.10
MaNCEL	0.42%	0.41%	1.02	0.28%	0.28%	1.01
MaNCRES	**18.94%**	**5.45%**	**3.48**	**10.44%**	**3.01%**	**3.47**
MvCCRES	0.68%	0.63%	1.08	2.18%	2.02%	1.08
MvNCRES	8.06%	4.77%	1.69	4.41%	2.61%	1.69
NonRESBGvbarnCC1pi	-	-	-	0.21%	0.21%	1.00
NonRESBGvbarnCC2pi	-	-	-	0.21%	0.21%	1.00
NonRESBGvbarnNC1pi	0.16%	0.16%	1.00	0.21%	0.21%	1.00
NonRESBGvbarnNC2pi	-	-	-	0.21%	0.21%	1.00
NonRESBGvbarpCC1pi	-	-	-	0.21%	0.21%	1.00
NonRESBGvbarpCC2pi	-	-	-	0.21%	0.21%	1.00
NonRESBGvbarpNC1pi	-	-	-	0.27%	0.27%	1.00
NonRESBGvbarpNC2pi	-	-	-	0.21%	0.21%	1.00
NonRESBGvnCC1pi	-	-	-	0.97%	0.96%	1.01
NonRESBGvnCC2pi	0.13%	0.13%	1.00	0.78%	0.78%	1.00
NonRESBGvnNC1pi_UBGenie	3.01%	2.51%	1.20	2.92%	2.44%	1.20
NonRESBGvnNC2pi_UBGenie	-	-	-	0.30%	0.30%	1.00
NonRESBGvpCC1pi	0.35%	0.35%	1.00	0.21%	0.21%	1.00
NonRESBGvpCC2pi	0.13%	0.13%	1.00	0.35%	0.35%	1.00
NonRESBGvpNC1pi	1.04%	1.02%	1.02	0.40%	0.40%	1.01
NonRESBGvpNC2pi	0.55%	0.52%	1.04	0.79%	0.76%	1.04
Min/Max Variations						
NormCCCOH	-	-	-	0.20%	0.20%	1.00
NormNCCOH	-	-	-	3.90%	3.48%	1.12
RPA_CCQE	0.04%	0.04%	1.00	1.29%	1.29%	1.00
Theta_Delta2Npi	7.83%	4.91%	1.59	0.98%	0.62%	1.57
VecFFCCQEshape	0.06%	0.06%	1.00	0.24%	0.24%	1.00
AxFFCCQEshape	0.01%	0.01%	1.00	0.30%	0.30%	1.00
DecayAngMEC	0.02%	0.02%	1.00	0.62%	0.62%	1.00

Table 9: *Unconstrained and constrained cross section uncertainties, broken down by systematic uncertainty source, for the* $2\gamma1p$ *and* $2\gamma0p$ *total background predictions. Note that only "genie_all" and the 7 Min/Max variations are used to build the final covariance matrices, with the individual variations that make up "genie_all" being shown for illustrative effects to inform which underlying physics is driving the size of the total uncertainty. The* M_A *NC Resonant variation is highlighted as it is one of the primary uncertainties on the NC* π^0 *backgrounds and is reduced by a factor of 3.5.*

5.2 Detector Systematic Uncertainties

Detector systematic uncertainties are assessed as described in detail in Ref. [18]. For the latest MicroBooNE Monte Carlo simulation, an innovative method [19], called wire-modification (or waveform-modification), was adopted to produce detector variation samples for a number of sources of detector systematic uncertainties [18]. This method characterizes the detector's response in terms of the charge (Q_{hit}) and width (σ_{hit}) of Gaussian hits of reconstructed ionization charge deposits as a function of time and TPC wire (see Fig. 46). By measuring the values of Q_{hit} and σ_{hit} for relevant variables of both data and Monte Carlo, the continuous ratio functions $R_Q^{(data/MC)}$ and $R_\sigma^{(data/MC)}$ can be obtained, which are used to produce varied Monte Carlo samples.

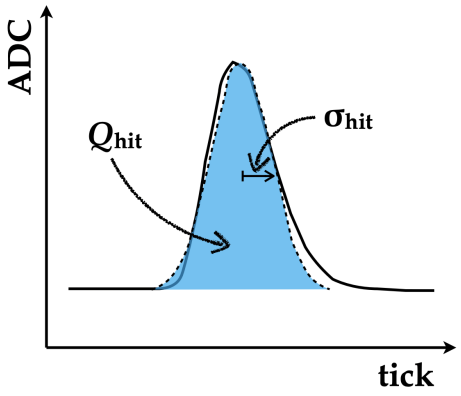

Figure 46: *Schematic of a hit [19]. The blue region represents fitting the hit with a Gaussian function, where Q_{hit} and σ_{hit} are integrated area (charge) and standard deviation from the Gaussian fit, respectively. The X axis is a time-tick, a unit of time analogous to time of readout.*

The majority of detector systematic effects are either related to the TPC wire response or PMT light yield systematics, with a small amount of additional systematics that do not fall into these categories. For each category, there are several sub-categories. For example, within the wire response systematics, there is one named "wire-modification X" (WireX) which includes all detector effects that affect the variables associated with the detector drift coordinate. Similarly, there are "wire-modification YZ" (WireYZ), "wire-modification track angles θ_{XZ} and θ_{YZ}" (AngleXZ and AngleYZ), and "wire-modification dE/dx" (dEdx) in this category which correspond to all detector effects that affect the variables associated with detector YZ (Y is vertical plane and Z is beam direction) coordinate plane, the track angles, and the charge deposited per unit length (dE/dx), respectively. For the Light Yield category, there are samples for 25% light yield reduction (LY), light yield attenuation (LYAtt) and light yield Rayleigh scattering length (LYRay). The other detector effects include space charge effects (SCE) and recombination effects (Recom2). For the single-photon analysis, five different final state Monte Carlo sub-samples are used to evaluate the uncertainties on the signal and background. These sub-samples are: NC Δ Radiative Decay (signal), NC π^0 (including $1\pi^0$ Coherent and $1\pi^0$ Non-Coherent), BNB intrinsic ν_e and $\bar{\nu}_e$ CC, ν_μ CC $1\pi^0$, and other BNB backgrounds.

The analysis process is exactly the same as that of single-photon selections and NC π^0 selections described in the previous sections but applied to detector variation samples. Figures 47 and 48 show area normalized shape comparisons of reconstructed shower energy spectra ($1\gamma 1p$ selection) and reconstructed π^0 momentum spectra ($2\gamma 1p$ selection) at the final selection stage, corresponding to the different variation.

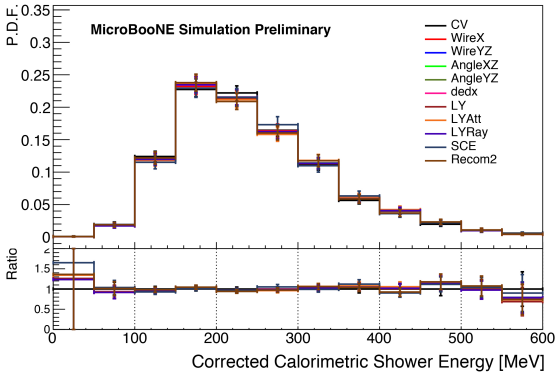

(a) Sub-sample: NC Δ Radiative

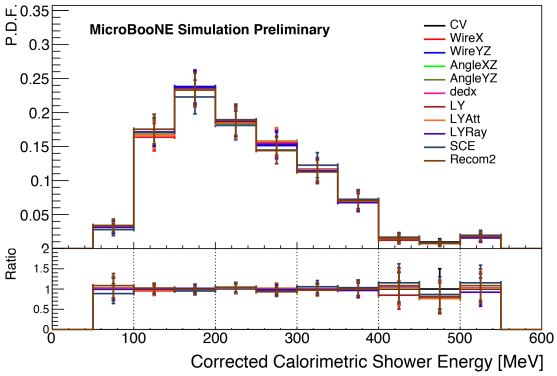

(b) Sub-sample: NC $1\pi^0$ (Non-Coherent)

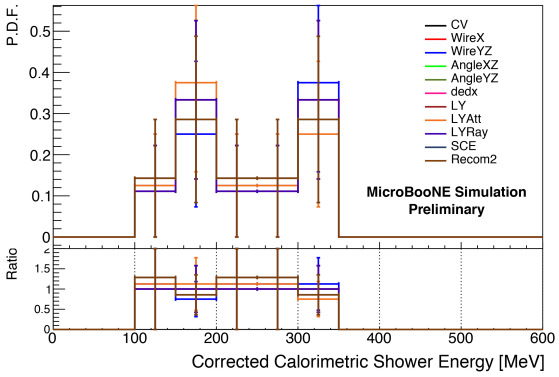

(c) Sub-sample: ν_μ CC $1\pi^0$

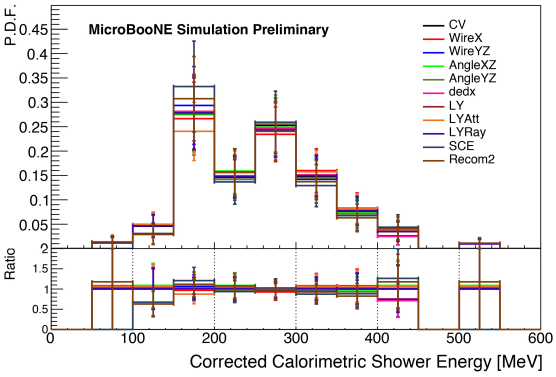

(d) Sub-sample: ν_e and $\bar{\nu}_e$ CC

Figure 47: *Area-normalized shape comparisons of shower energy spectra for CV and for all detector systematics variations, shown for each sub-sample in the $1\gamma 1p$ selected sample, at final selection stage. The lower part of each plot is the ratio of various detector systematic effects to the CV.*

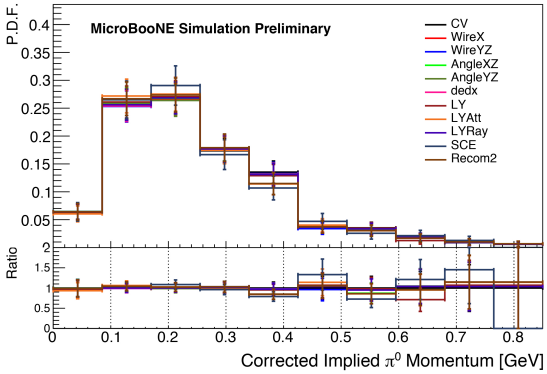

(a) Sub-sample: NC Δ Radiative

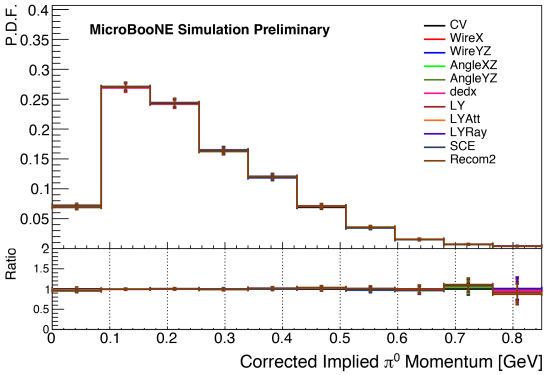

(b) Sub-sample: NC $1\pi^0$ (Non-Coherent)

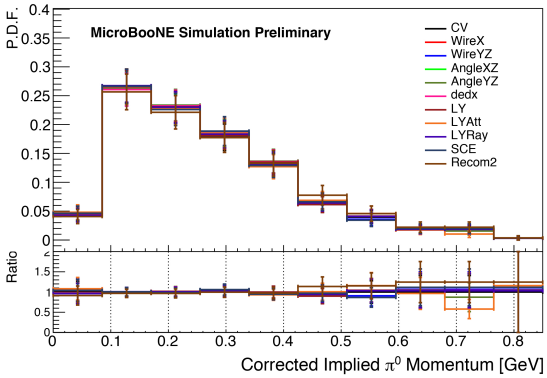

(c) Sub-sample: ν_μ CC $1\pi^0$

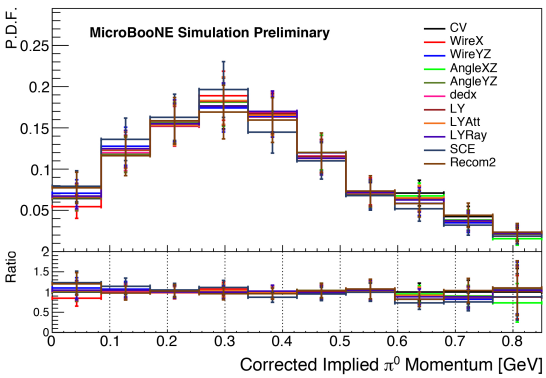

(d) Sub-sample: ν_e and $\bar{\nu}_e$ CC

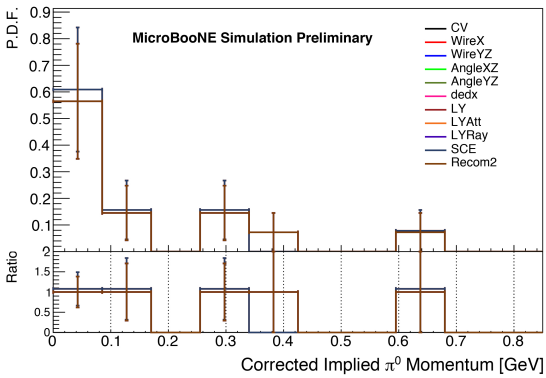

(e) Sub-sample: BNB Other

Figure 48: *Area-normalized shape comparisons of π^0 momentum spectrum between CV and detector systematics for $2\gamma 1p$ at final cut stage. The lower part of each plot is the ratio of various detector systematic effects to the CV.*

Table 10 summarizes the percent uncertainties assessed on each sub-sample at final selection stage. As can be seen in the table, the detector variations again have little effect for the NC Δ signal. They have up to $\sim$3.5% variations for NC π^0 induced backgrounds which form the largest background for this channel. The "BNB Other" sample comprises an almost-negligible background, but there are still residual events yielding large uncertainties in a few detector variation samples. For CC π^0 and intrinsic ν_e CC backgrounds, even though the variations are relatively large in percentage, because these backgrounds are relatively small, the contributing absolute systematic uncertainty is comparable to that of NC π^0. Table 11 summarizes the percent uncertainties assessed on each sub-sample at final selection stage. Figure 49 shows the total effects from the detector systematics on the reconstructed shower spectrum ($1\gamma 1p$) and reconstructed π^0 momentum spectrum ($2\gamma 1p$).

Sub-sample	**WireX**	**WireYZ**	**AngleXZ**	**AngleYZ**	**dEdx**	**LY**	**LYAtt**	**LYRay**	**SCE**	**Recom2**	**Sum**
NC Δ	0.9	0.2	0.9	0.2	3.5	0.5	1.8	0.9	1.0	1.4	3.0
NC $1\pi^0$ Not Coh	3.5	2.2	1.5	1.7	0.2	1.5	1.7	1.0	1.4	2.9	6.2
NC $1\pi^0$ Coh	100	50	50	50	50	0.0	50	0.0	50	100	180
NC Multi-π^0	-	-	-	-	-	-	-	-	-	-	-
CC ν_μ $1\pi^0$	33.3	25.0	36.1	11.1	11.1	11.1	12.5	11.1	42.9	0.0	73.5
Intrinsic $\nu_e/\bar{\nu}_e$ CC	28.3	6.7	3.8	0.8	1.9	1.2	2.6	0.2	33.7	12.3	46.4
BNB Other	-	0.0	0.0	0.0	0.0	-	-	-	0.0	0.0	0.0

Table 10: *Percent (%) shifts in number of events for each $1\gamma 1p$ sub-sample, for each systematic variation, defined as $(N^{var} - N^{CV})/N^{CV} \times 100\%$, at final selection stage. As noted before, the first two samples, NC Δ and NC π^0 Non-Coherent are both the primary components and also the only two high statistics detector variation samples that would be most robust to statistical variations. The combined (summed in quadrature) detector normalization uncertainties are given in the final column. For the purposes of this sum, the wire modified dEdx is not included; this is because both wire modified dEdx and the "Recombination 2" systematics cover the same underlying physics and including both would be double counting. "Recombination2" was chosen as it had the largest impact on our primary background, the NC π^0.*

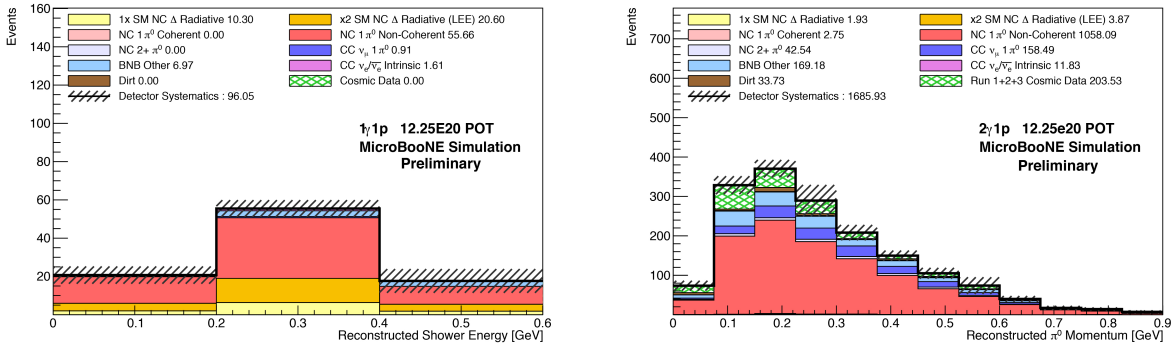

(a) *$1\gamma 1p$ selection final stage.* ***(b)*** *$2\gamma 1p$ selection final stage.*

Figure 49: *Final selected $1\gamma 1p$ and $2\gamma 1p$ distributions projected to Run 1-5 statistics of 12.25×10^{20} POT, shown with detector systematic uncertainties.*

Sub-sample	**WireX**	**WireYZ**	**AngleXZ**	**AngleYZ**	**dEdx**	**LY**	**LYAtt**	**LYRay**	**SCE**	**Recom2**	**Sum**
NC Δ	5.2	0.6	0.9	4.6	4.9	2.2	0.7	0.3	6.4	12.2	15.6
NC $1\pi^0$ Not Coh	1.8	0.9	1.0	0.4	1.6	0.0	0.6	0.4	1.1	2.2	3.4
NC $1\pi^0$ Coh	8.8	3.0	14.3	2.9	20.0	0.0	2.9	3.0	16.1	17.6	29.8
NC Multi-π^0	50	50	100	50	0.0	0.0	0.0	0.0	0.0	50	141
CC ν_μ $1\pi^0$	3.8	1.9	5.8	7.6	0.3	4.6	6.9	0.3	1.7	8.2	15.8
Intrinsic $\nu_e/\bar{\nu}_e$ CC	4.3	6.5	10.5	0.6	4.5	2.1	4.1	2.2	1.0	23.8	27.0
BNB Other	2.9	31.9	7.3	14.5	39.1	0.0	7.8	0.0	18.8	45.9	61.7

Table 11: *Percent (%) shifts in number of events for each $2\gamma 1p$ sub-sample, for each systematic variation, defined as $(N^{var} - N^{CV})/N^{CV} \times 100\%$, at final selection stage. The combined (summed in quadrature) detector normalization uncertainties are given in the final column. For the purposes of this sum, the wire modified dEdx is not included, this is because both wire modified dE/dx and the "Recombination 2" systematics cover the same underlying physics and including both would be double counting. "Recombination 2" was chosen as it had the largest impact on our primary background, the NC π^0.*

6 Final Sensitivities and Preliminary Results

6.1 Fit Method

The final $1\gamma 1p$, $1\gamma 0p$, $2\gamma 1p$, and $2\gamma 0p$ selected distributions obtained following the methodology presented in Secs. 3 and 4, summarized in Fig. 50, along with their statistical and systematic uncertainties and systematic correlations, are used in a final fit to excess NC $\Delta \to N\gamma$ events.

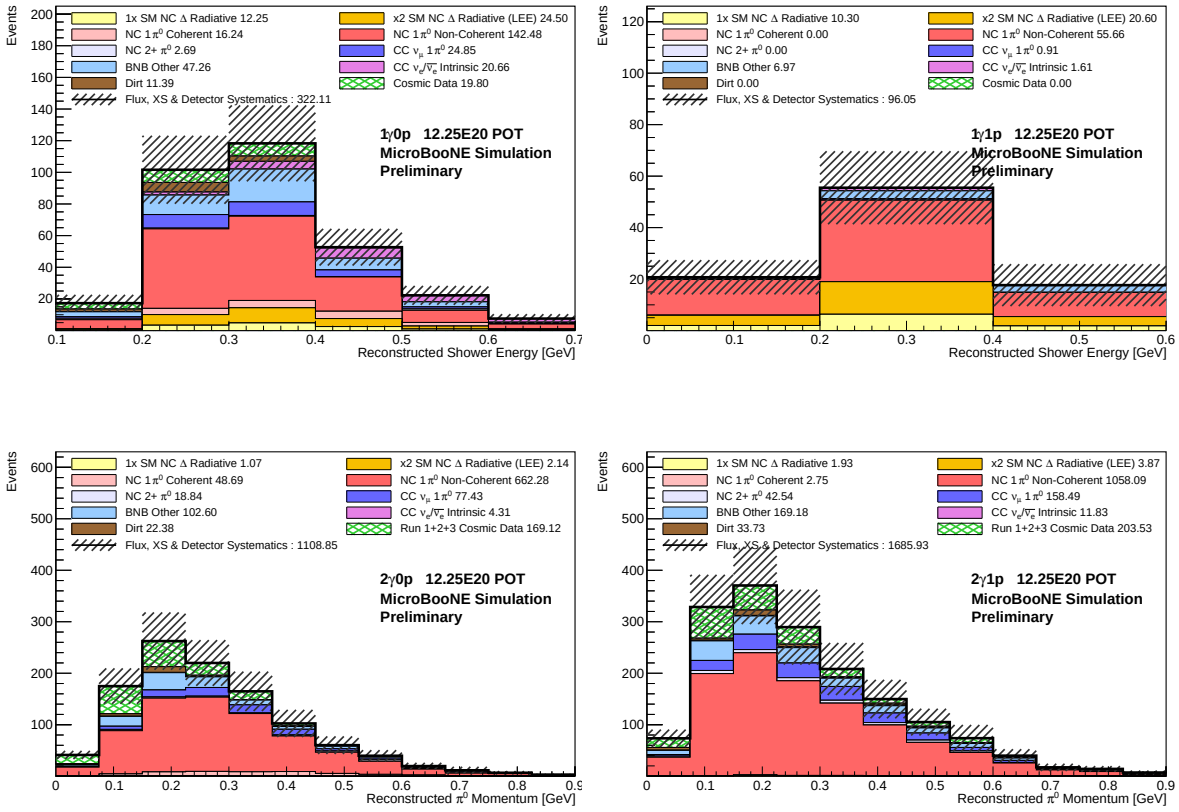

Figure 50: *Final selection distributions for 1-shower (top), 2-shower (bottom), 0-proton (left) and 1-proton (right) topologies. The distributions show predictions scaled to* 12.25×10^{20} *POT, which corresponds to the total POT for Runs 1-5. These distributions correspond to the GENIE central value (CV) prediction, i.e. no normalization correction has been applied to the coherent and non-coherent NC* π^0 *rates.*

Prior to the fit, the 2γ selections are used to extract normalization correction factors to the GENIE-predicted NC π^0 coherent and non-coherent rates. The extraction of these correction factors is carried out via a side-by-side fit to $2\gamma 1p$ and $2\gamma 0p$ data and Monte Carlo distributions, each provided in terms of three (3) bins of reconstructed cosine of the π^0 angle relative to the neutrino beam direction. During the fit, the normalizations of the coherent and non-coherent NC π^0 components (N_{coh} and $N_{non-coh}$) in the $2\gamma 1p$ and $2\gamma 0p$ distributions are allowed to vary, and their best fit parameters are determined by minimizing the following χ^2:

$$\chi^2 = \sum_{i,j}(MC_{scaled,i} - D_i)\left(\frac{3}{1/D_i + 2/MC_i}\delta_{ij} + M_{ij}^{syst}\right)^{-1}(MC_{scaled,j} - D_j), \quad (3)$$

where D refers to data, MC_{scaled} refers to the total Monte Carlo prediction appropriately scaled by N_{coh} and $N_{non-coh}$ factors, and M_{syst} represents a systematic covariance matrix iteratively updated to the best fit prediction, MC. This χ^2 is the Combined Neyman-Pearson (CNP) χ^2 [20], which is an approximation of the Poisson-likelihood built from a linear combination of the Neyman and Pearson χ^2's which leads to a significantly smaller bias on the best-fit model parameters compared to those using either the individual Neyman's or Pearson's chi-square. The fit accounts for statistical and full systematic uncertainties, including systematic correlations between the two distributions, except GENIE normalization uncertainties on the coherent and non-coherent components of the NC π^0 prediction, and associated correlations, which are purposefully removed from the fit. The resulting allowed parameter space is shown in Fig. 51.

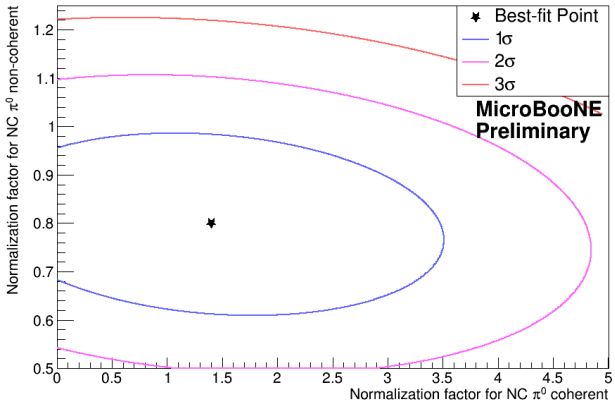

Figure 51: *1, 2, and 3σ C.L. contours obtained from the 3-bin NC π^0 fit of the normalization of the coherent and non-coherent components of NC π^0 production in the $2\gamma 1p$ and $2\gamma 0p$ samples, using data collected in the first Runs 1-3 of MicroBooNE data. Included in the fit are flux, cross-section, and detector systematic uncertainties and correlations, as well as statistical uncertainties.*

We have verified that, once the resulting correction factors from the fit, $N_{coh} = 1.4$ and $N_{non-coh} = 0.8$, are applied to the $2\gamma 1p$ and $2\gamma 0p$ final selections, the agreement between data and Monte Carlo generally improves in all kinematic variables. This is illustrated in Figs. 52 and 53, for several kinematic variables.

The predicted signal and background events corresponding to 12.25×10^{20} POT are tabulated in Tabs. 12 and 13, without and with the coherent and non-coherent NC π^0 corrections applied. For the full data set of 12.25×10^{20} POT, corresponding to data collected by MicroBooNE during Runs 1-5, a statistical significance of 2.8σ (3.0σ) is expected for an excess of NC Delta Radiative events amounting to $2\times$ SM contribution above the SM (corrected) prediction; such excess, if observed, would be consistent with an NC Δ interpretation of the MiniBooNE observed low-energy excess.

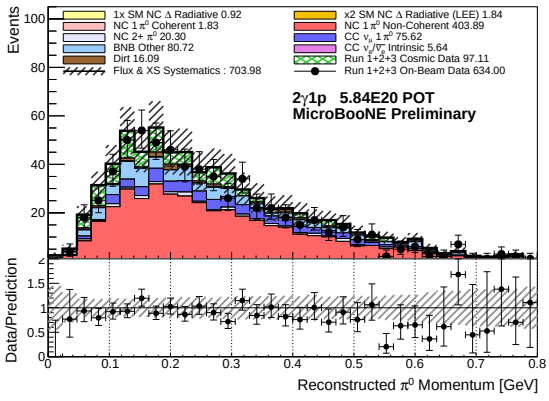

(Data/MC: 0.90) (KS: 0.962) (χ^2/nDOF: 15.65/34) (χ^2 P^{val}: 0.997)

(a) π^0 *Momentum*

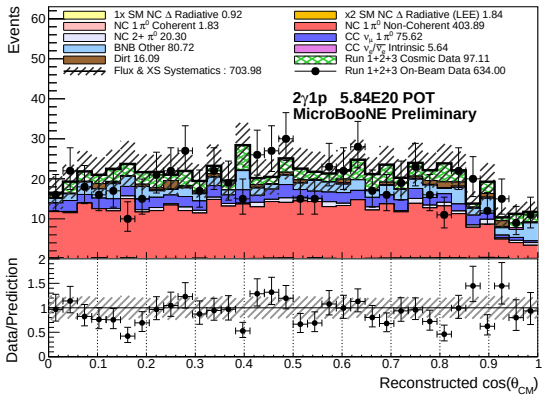

(Data/MC: 0.90) (KS: 0.951) (χ^2/nDOF: 23.33/34) (χ^2 P^{val}: 0.916)

(b) $\cos(\theta_{cm})$

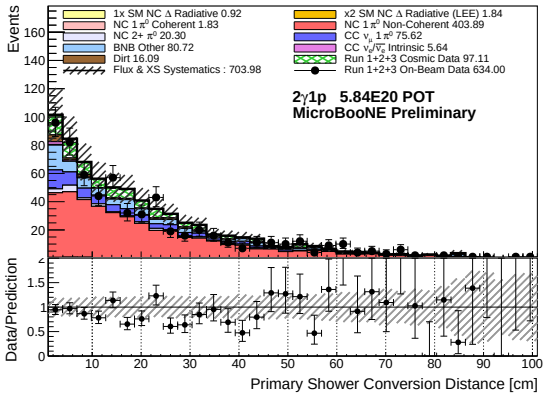

(Data/MC: 0.90) (KS: 0.990) (χ^2/nDOF: 28.36/34) (χ^2 P^{val}: 0.740)

(c) Leading Shower Conversion Distance

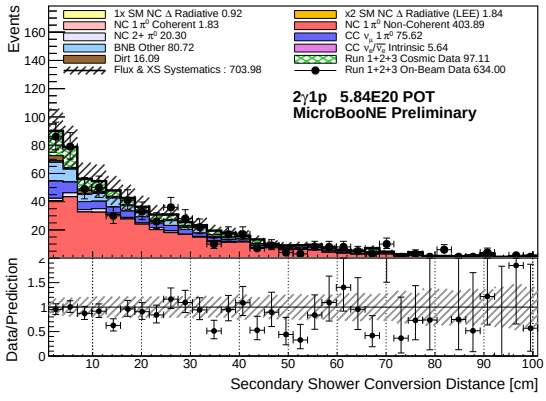

(Data/MC: 0.90) (KS: 1.000) (χ^2/nDOF: 30.30/34) (χ^2 P^{val}: 0.650)

(d) Subleading Shower Conversion Distance

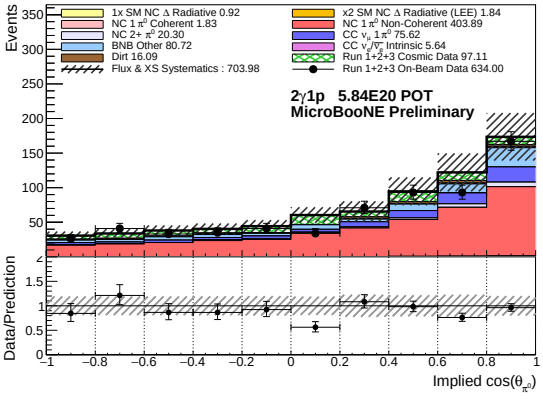

(Data/MC: 0.90) (KS: 1.000) (χ^2/nDOF: 5.23/10) (χ^2 P^{val}: 0.875)

(e) $\cos\theta_\pi$

Figure 52: *Some select Data to Monte Carlo comparisons for the 2γ1p final selection, after correction of the coherent and non-coherent NC π^0 normalization. Uncertainties shown include flux and cross-section systematics. To be compared with Fig. 34, which does not have the correction applied. Note: detector systematic uncertainties have been evaluated but are omitted in these distributions.*

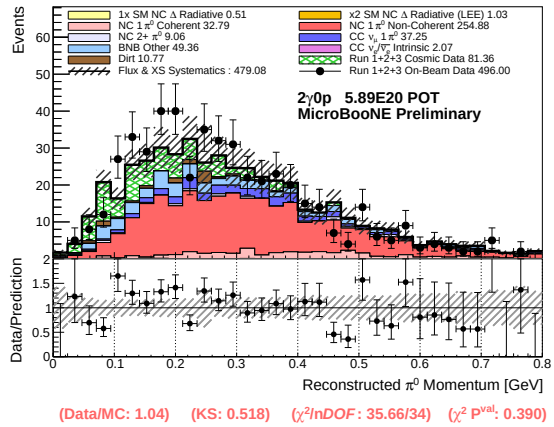

(Data/MC: 1.04) (KS: 0.518) (χ^2/nDOF: 35.66/34) (χ^2 P^{val}: 0.390)

(a) *π^0 Momentum*

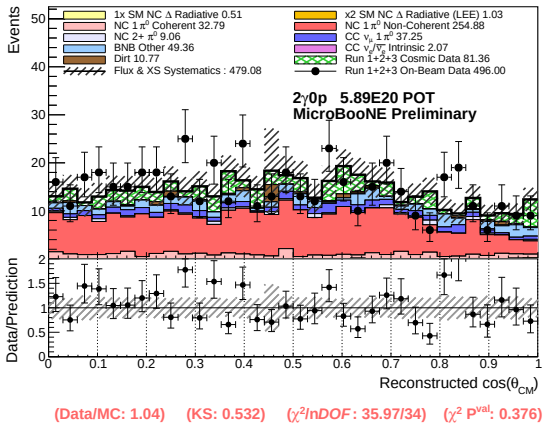

(Data/MC: 1.04) (KS: 0.532) (χ^2/nDOF: 35.97/34) (χ^2 P^{val}: 0.376)

(b) *$\cos(\theta_{cm})$*

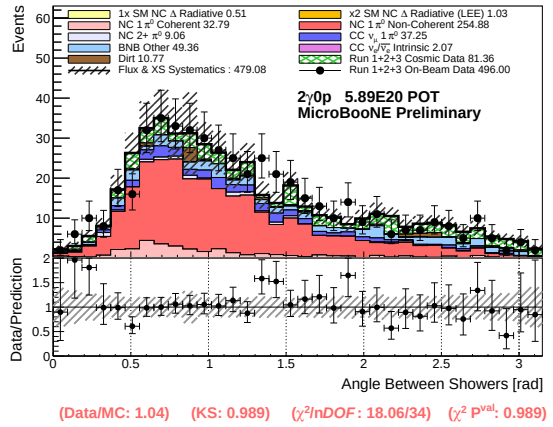

(Data/MC: 1.04) (KS: 0.989) (χ^2/nDOF: 18.06/34) (χ^2 P^{val}: 0.989)

(c) *Angle Between Showers*

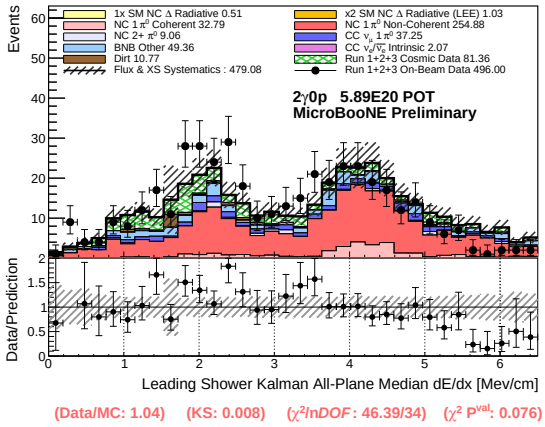

(Data/MC: 1.04) (KS: 0.008) (χ^2/nDOF: 46.39/34) (χ^2 P^{val}: 0.076)

(d) *Leading Photon dE/dx*

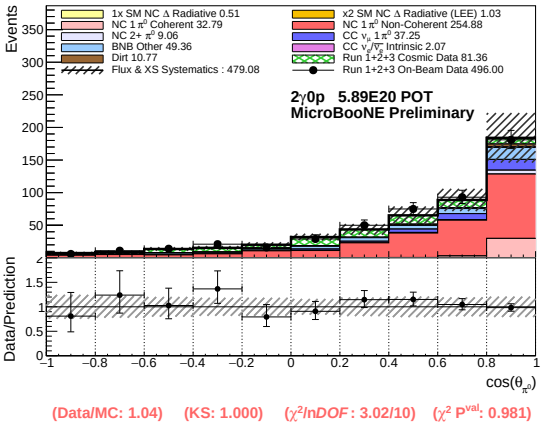

(Data/MC: 1.04) (KS: 1.000) (χ^2/nDOF: 3.02/10) (χ^2 P^{val}: 0.981)

(e) *$\cos\theta_\pi$*

Figure 53: *Some select Data to Monte Carlo comparisons for the 2γ0p final selection, after correction of the coherent and non-coherent NC π^0 normalization. Uncertainties shown include all flux and cross-section systematics. To be compared with Fig. 35, which does not have the correction applied. Note: detector systematic uncertainties have been evaluated but are omitted in these distributions.*

The application of the resulting correction factors from the fit, $N_{coh} = 1.4$ and $N_{non-coh} = 0.8$, to GENIE-predicted central values in the single-photon analysis yields the corrected distributions shown in the following subsection (specifically, in Fig. 54). Sensitivity projections are also provided in the following subsection, with and without this correction applied.

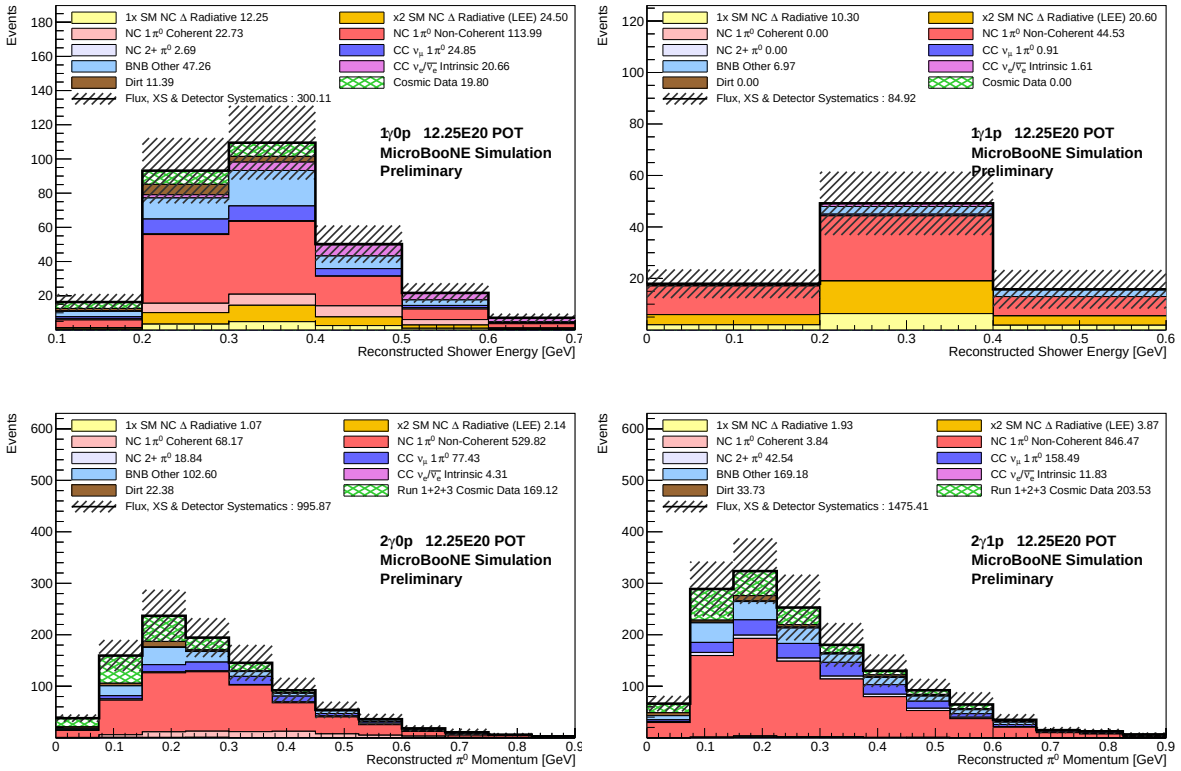

Figure 54: *Final selection distributions for 1-shower (top), 2-shower (bottom), 0-proton (left) and 1-proton (right) topologies. The distributions show predictions scaled to* 12.25×10^{20} *POT, which corresponds to the total POT for Runs 1-5. These distributions correspond to the corrected GENIE prediction, i.e. normalization corrections of* $N_{coh} = 1.4$ *and* $N_{non-coh} = 0.8$ *have been applied to the coherent and non-coherent NC* π^0 *fractions, respectively.*

To assess sensitivity either to a hypothesized signal consistent with the MiniBooNE observed low-energy excess, or to any enhancement x_Δ to the SM predicted NC $\Delta \to N\gamma$ cross-section, a full fit is performed simultaneously to the 1γ and 2γ selections. The data and Monte Carlo predictions are fit as a function of reconstructed shower energy in the case of the 1γ selections and reconstructed π^0 momentum in the case of the 2γ selections, minimizing the following χ^2:

$$\chi^2 = (MC_{scaled,i} - D_i)(M_{ij}^{syst} + M_{ij}^{stat})^{-1}(MC_{scaled,j} - D_j) \tag{4}$$

where

$$M_{ij}^{stat} = \frac{3}{1/D_i + 2/MC_i}\delta_{ij} \ . \tag{5}$$

Here, MC_{scaled} is the Monte Carlo predicted spectrum modulated according to three fit parameters: x_Δ, N_{coh}, and $N_{non-coh}$. For a sensitivity estimate, D is typically the *null* spectrum with NC π^0 coherent and non-coherent components corresponding to either the GENIE central value or the corrected central value according to $N_{coh,bf}$ and $N_{non-coh,bf}$; MC is the central value spectrum corresponding to either the GENIE central value or the corrected central value; M^{syst} is the full systematics covariance matrix evaluated at the best fit point, which includes flux, cross-section, and detector uncertainties and correlations; M^{stat} is the CNP statistical covariance matrix evaluated at the best fit point, arrived at after an iterative fit, following the method in [21].

The final fractional covariance and correlation matrices corresponding to the GENIE CV (uncorrected) predictions are shown in Figs. 55 and 56, respectively. The order of fitted channels (left to right) correspond to $1\gamma 1p$ (3 bins from 0 to 600 MeV), $1\gamma 0p$ (6 bins from 100 to 700 MeV), $2\gamma 1p$ (12 bins from 0 to 900 MeV) and $1\gamma 0p$ (12 bins from 0 to 900 MeV). Those matrices include "genie_all", flux, and detector systematics the selections are subject to. They correspond to the collapsed background plus no signal prediction (i.e. the NC Δ radiative rate is set to its $1\times$SM value) central values for 1γ and 2γ selections.

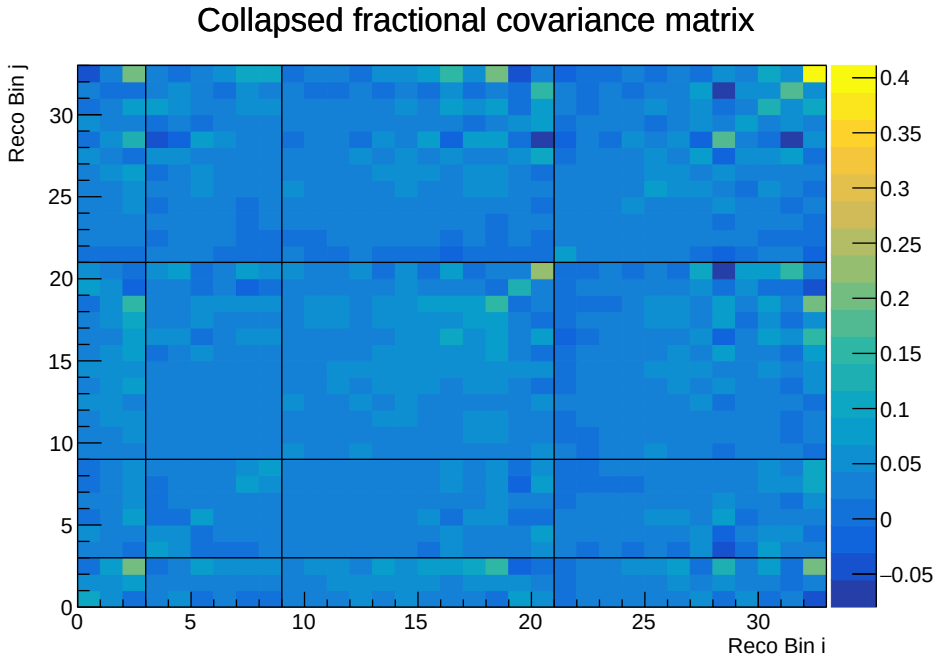

Figure 55: *Final collapsed fractional covariance matrix for the $1\gamma 1p$, $1\gamma 0p$, $2\gamma 1p$ and $2\gamma 0p$ samples used in the final fits, with full flux, cross section and detector systematics included.*

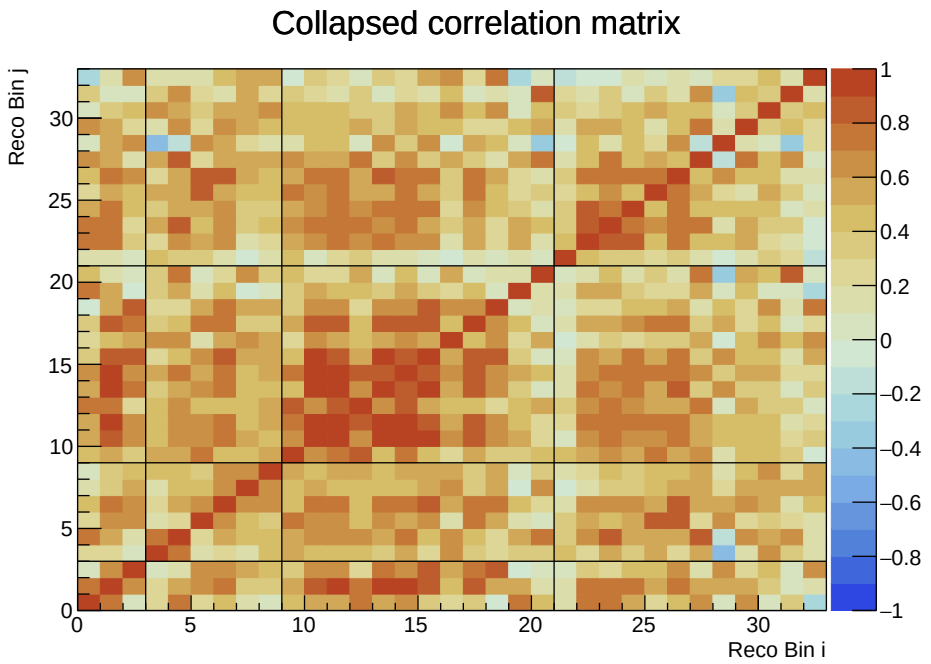

Figure 56: *Final collapsed correlation matrix for the 1γ1p, 1γ0p, 2γ1p and 2γ0p samples used in the final fits, with full flux, cross section and detector systematics included. Correlation factors between the most relevant bins in the 2γ1p and 1γ1p samples are in the range of 50-90%, allowing for a strong constraint of the NC π^0 backgrounds via the simultaneous 1γ and 2γ fit method.*

6.2 Projected Sensitivity to NC $\Delta \to N\gamma$

The sensitivities to an enhanced NC $\Delta \to N\gamma$ rate are shown in Figs. 60 (uncorrected NC π^0 rates) and 61 (corrected NC π^0 rates), left, for 12.25×10^{20} POT, which corresponds to the full set of MicroBooNE collected data, from Runs 1-5. The current sensitivity projections for the presently analyzed data from Runs 1-3 are shown in the same figures, on the right. As shown in the figures, which are Feldman-Cousins-corrected [22] using 10,000 fake experiments drawn from the underlying systematic and statistical covariance matrix, MicroBooNE will be able to measure an excess consistent with the MiniBooNE low energy excess interpretation as an underestimate of the NC $\Delta \to N\gamma$ by a factor of 3 at well above 99% confidence level, with its full data set of 12.25×10^{20} POT.

Fake data studies of sensitivities for two-hypothesis testing are provided in Fig. 57. Those are evaluated using 250,000 fake experiments, allowing accurate extrapolation to significance levels of up to 4σ. As shown by the median sensitivity in these figures, the MiniBooNE low-energy excess (LEE) interpreted as NC $\Delta \to N\gamma$ events can be rejected by MicroBooNE in favor of the SM prediction at 2.1σ, assuming a measurement consistent with the SM prediction. For these studies we have focused on three scenarios, the LEE ($x_\Delta = 3$), the No-Δ ($x_\Delta = 0$) and the SM ($x_\Delta = 1$) hypothesis. In particular, the figures highlight the following:

- The median significance of rejecting the No-Δ hypothesis ($x_\Delta = 0$) in favor of LEE hypothesis ($x_\Delta = 3$), assuming LEE is true is $\mathbf{3.6\sigma}$ (68% of experiments range: $2.4\sigma \to 4.6\sigma$)
- The median significance of rejecting SM hypothesis ($x_\Delta = 1$) in favor of LEE hypothesis ($x_\Delta = 3$), assuming LEE is true is $\mathbf{2.3\sigma}$ (68% of experiments range: $1.2\sigma \to 3.3\sigma$)
- The median significance of rejecting LEE hypothesis ($x_\Delta = 3$) in favor of the No-Δ hypothesis ($x_\Delta = 0$), assuming the No-Δ is true is $\mathbf{3.2\sigma}$ (68% of experiments range: $2.2\sigma \to 4.3\sigma$)
- The median significance of rejecting LEE hypothesis ($x_\Delta = 3$) in favor of SM hypothesis ($x_\Delta = 1$), assuming SM is true is $\mathbf{2.1\sigma}$ (68% of experiments range: $1.2\sigma \to 3.1\sigma$)

It is worth noting that by fitting to 1γ and 2γ samples simultaneously, systematic uncertainties on the 1γ selections are effectively reduced, as illustrated in Tab. 14, Fig. 58 and Fig. 59. This demonstrates the importance of the NC π^0 selection to the analysis, and showcases how powerful is the ability of the MicroBooNE LArTPC to provide measurements for a wide variety of exclusive interaction final states.

Sub-sample	$1\gamma1p$ **Selection**	$1\gamma0p$ **Selection**	$2\gamma1p$ **Selection**	$2\gamma0p$ **Selection**
NC $1\pi^0$ Coherent	0.00	16.24	2.75	48.69
NC $1\pi^0$ Non-coherent	55.66	142.48	1058.09	662.28
NC $\geq 2\pi^0$	0.00	2.69	42.54	18.84
CC ν_μ $1\pi^0$	0.91	24.85	158.49	77.43
BNB Other	6.97	47.26	169.18	102.60
CC $\nu_e/\bar{\nu}_e$ Intrinsic	1.61	20.66	11.83	4.31
Dirt	0.00	11.39	33.73	22.38
Cosmic Data	0.00	19.80	203.53	169.12
1×SM NC Δ Radiative	10.30	12.25	1.93	1.07
Total (1×SM) Prediction	75.45	297.61	1682.07	1106.71
2×SM NC Δ Radiative	20.60	24.50	N/A	N/A

Table 12: *Event breakdown of final selections for the $1\gamma1p$, $1\gamma0p$, $2\gamma1p$, $2\gamma0p$ samples, for 12.25×10^{20} POT,* ***without*** *coherent and non-coherent NC π^0 correction.*

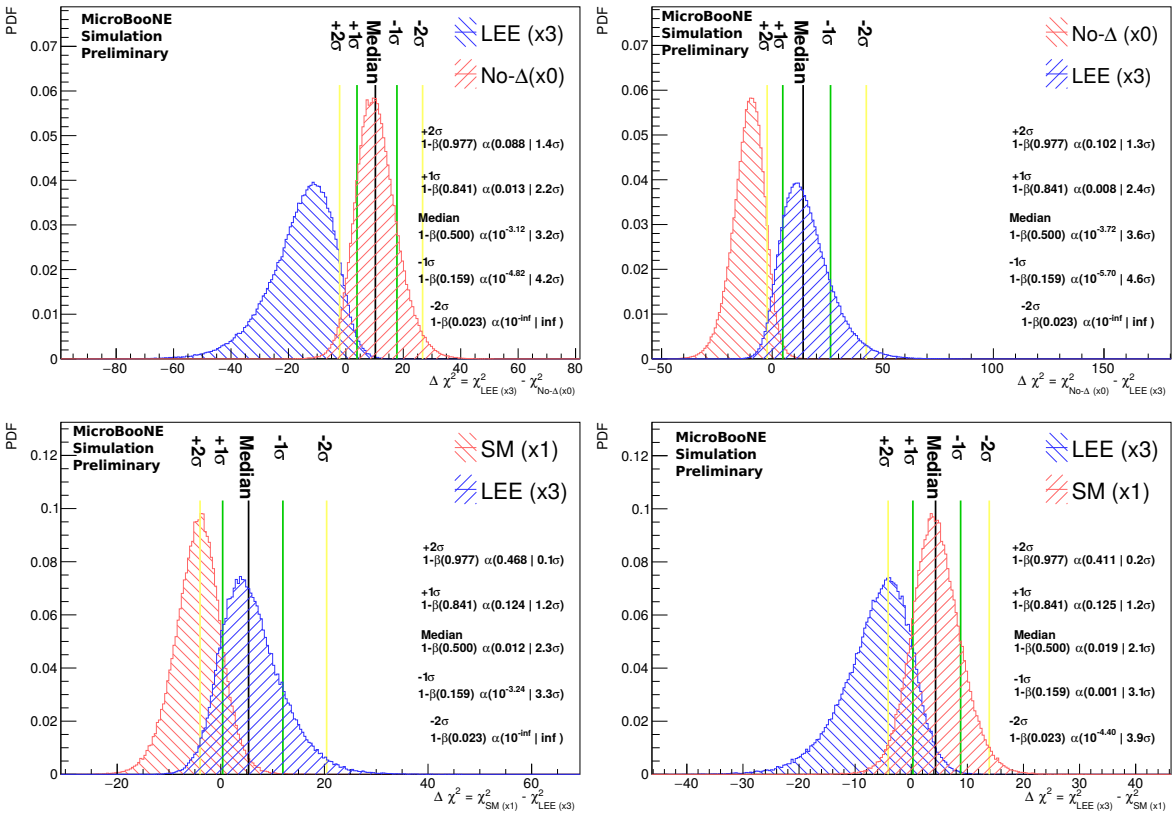

Figure 57: *Two-hypothesis test frequentist studies for a variety of hypotheses of* Δ *radiative rates including the SM rate (*$\times 1$ *expected), the LEE rate (*$\times 3$ *expected) and the No-*Δ *rate (*$\times 0$ *expected, i.e. no* Δ *radiative decay), for the full MicroBooNE Run 1-5 data set corresponding to* 12.25×10^{20} *POT.*

Sub-sample	$1\gamma 1p$ **Selection**	$1\gamma 0p$ **Selection**	$2\gamma 1p$ **Selection**	$2\gamma 0p$ **Selection**
NC $1\pi^0$ Coherent	0.00	22.73	3.84	68.17
NC $1\pi^0$ Non-coherent	44.53	113.99	846.47	529.82
NC $\geq 2\pi^0$	0.00	2.69	42.54	18.84
CC ν_μ $1\pi^0$	0.91	24.85	158.49	77.43
BNB Other	6.97	47.26	169.18	102.60
CC $\nu_e/\bar{\nu}_e$ Intrinsic	1.61	20.66	11.83	4.31
Dirt	0.00	11.39	33.73	22.38
Cosmic Data	0.00	19.80	203.53	169.12
$1\times$SM NC Δ Radiative	10.30	12.25	1.93	1.07
Total ($1\times$SM) Prediction	75.45	297.61	1682.07	1106.71
$2\times$SM NC Δ Radiative	20.60	24.50	N/A	N/A

Table 13: *Event breakdown of final selections for the* $1\gamma 1p$, $1\gamma 0p$, $2\gamma 1p$, $2\gamma 0p$ *samples, for* 12.25×10^{20} *POT,* ***with*** *coherent and non-coherent NC* π^0 *corrections applied (corresponding to* $N_{coh} = 1.4$, $N_{non-coh} = 0.8$*).*

Sample (bin)	$\sigma_{unconstrained}$ (%)	$\sigma_{constrained}$ (%)	Reduction Factor
$1\gamma 0p$ (100-200 MeV)	28.7	26.0	1.10
$1\gamma 0p$ (200-300 MeV)	20.6	12.3	1.68
$1\gamma 0p$ (300-400 MeV)	21.6	11.6	1.91
$1\gamma 0p$ (400-500 MeV)	18.9	9.40	2.01
$1\gamma 0p$ (500-600 MeV)	23.4	13.7	1.71
$1\gamma 0p$ (600-700 MeV)	22.2	14.5	1.54
$1\gamma 1p$ (0-200 MeV)	25.6	9.41	2.73
$1\gamma 1p$ (200-400 MeV)	25.5	8.26	3.09
$1\gamma 1p$ (400-600 MeV)	30.0	13.5	2.22

Table 14: *The total (flux, cross-section, and detector) constrained fractional uncertainties, and factor-reduction, for each bin of the $1\gamma 1p$ and $1\gamma 0p$ selections, assuming full Run1-5 12.25×10^{20} POT. Note: The total uncertainty ignores photonuclear absorption uncertainty, which is effectively negligible.*

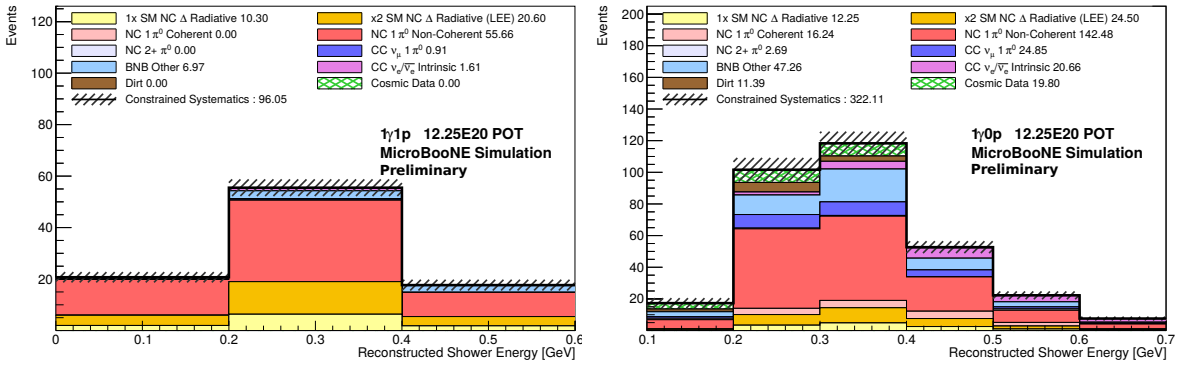

Figure 58: *Final selection distributions for the $1\gamma 1p$ (left) and $1\gamma 0p$ (right) topologies. The distributions show predictions scaled to 12.25×10^{20} POT, as in Fig. 50, but with the effective anticipated systematic uncertainty reduction after applying the $2\gamma 1p$ and $2\gamma 0p$ constraint reflected in the reduced uncertainty bands.*

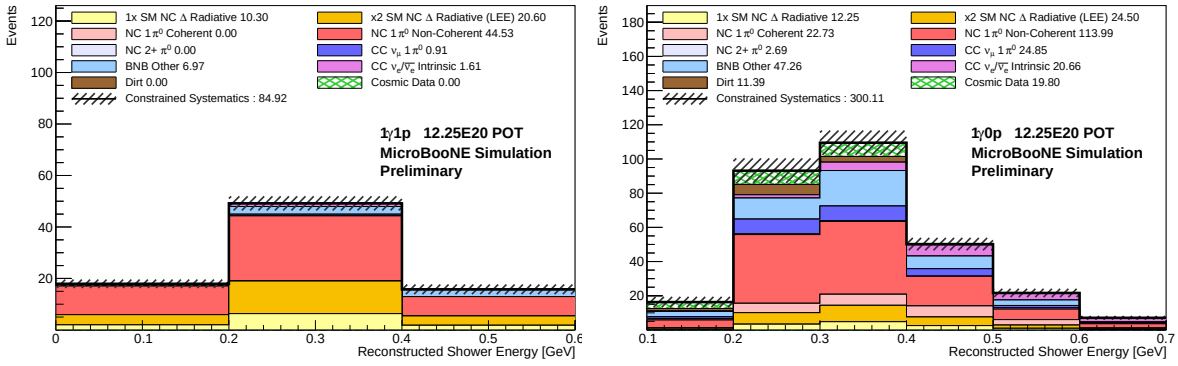

Figure 59: *Final selection distributions for the $1\gamma 1p$ (left) and $1\gamma 0p$ (right) topologies. The distributions show predictions scaled to 12.25×10^{20} POT, as in Fig. 50, but with the NC 1 π^0 Coherent and NC 1 π^0 Non-Coherent corrections applied (corresponding to $N_{coh} = 1.4$, $N_{non-coh} = 0.8$) and effective anticipated systematic uncertainty reduction after applying the $2\gamma 1p$ and $2\gamma 0p$ constraint reflected in the reduced uncertainty bands.*

To further improve the sensitivity studies from looking at simple 2-hypothesis tests, we elevate the Δ radiative scale factor (x_Δ) to a continuous parameter and follow the Feldman-Cousins method to construct classical confidence intervals as a function of observed Δ radiative scale factor (x_Δ). The results of this are shown in Fig. 60 for both the full MicroBooNE dataset of Runs 1-5 (12.5×10^{20} POT) and Fig. 60 for a first partial result with Runs 1-3 (6.9×10^{20} POT).

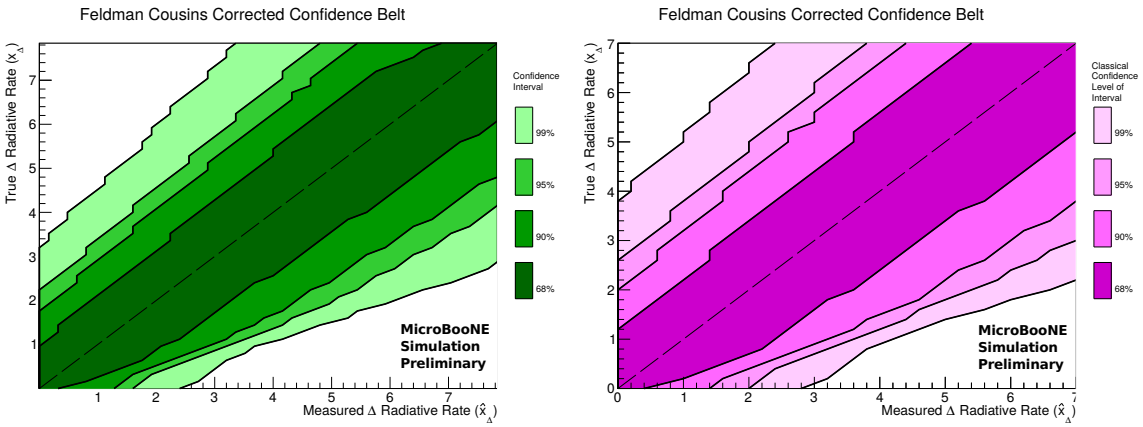

Figure 60: *Feldman-Cousins calculated classical confidence belt for a combined* $1\gamma1p$, $1\gamma0p$, $2\gamma1p$ *and* $2\gamma0p$ *fit with full flux, cross-section and detector systematic uncertainties, fitting only for* x_Δ *with the non-coherent and coherent* π^0 *rates fixed at the GENIE CV. The left plot shows the confidence belts assuming the full MicroBooNE dataset of Runs 1-5 POT (*12.25×10^{20} *POT), whereas the right plot shows the results for a partial data set of Runs 1-3 (*6.9×10^{20} *POT). To construct a classical confidence interval of a given confidence (e.g. 90%) one draws a vertical line up from the assumed observed best-fit* Δ *radiative decay rate, with the intersection of this line and the appropriate contour giving the confidence interval.*

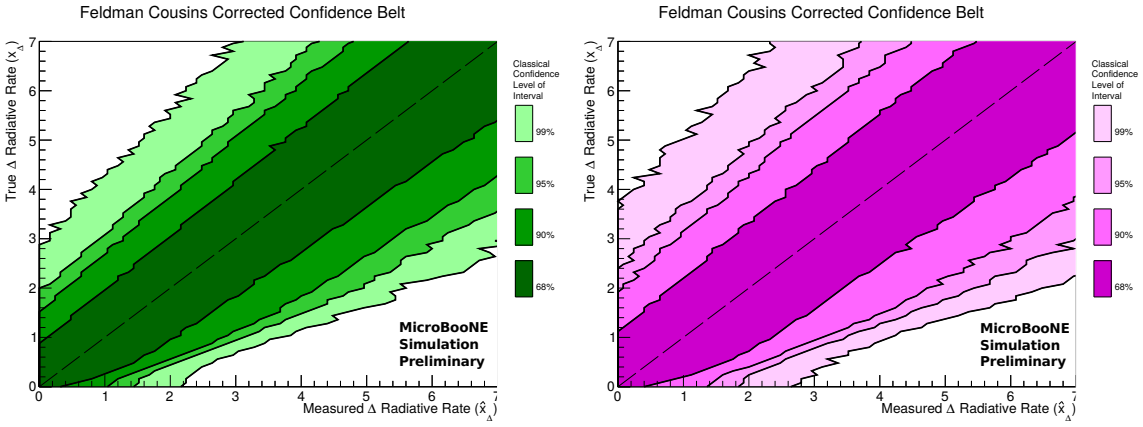

Figure 61: *Feldman-Cousins calculated classical confidence belt for a combined* $1\gamma 1p$, $1\gamma 0p$, $2\gamma 1p$ *and* $2\gamma 0p$ *fit with full flux, cross-section and detector systematic uncertainties, fitting only for* x_Δ *with the non-coherent and coherent* π^0 *rates fixed at the values obtained in the* 2γ *angular fit, corresponding to* $N_{coh} = 1.4$, $N_{non-coh} = 0.8$. *The left plot shows the confidence belts assuming the full MicroBooNE data set of Runs 1-5 POT (*12.25×10^{20} *POT), whereas the right plot shows the results for a partial data set of Runs 1-3 (*6.9×10^{20} *POT). To construct a classical confidence interval of a given confidence (e.g. 90%) one draws a vertical line up from the assumed observed best-fit* Δ *radiative decay rate, with the intersection of this line and the appropriate contour giving the confidence interval.*

A subset of the information shown in Fig. 60, for hypothetical data measurements of $\hat{x}_\Delta = 0$ and $\hat{x}_\Delta = 1$ is highlighted in Fig. 62 where the allowed regions on x_Δ have been mapped to the underlying GENIE cross-section on argon in units of σ (10^{-42}cm^2/nucleon). Both of these produce one-sided intervals bounding the cross-section from above.

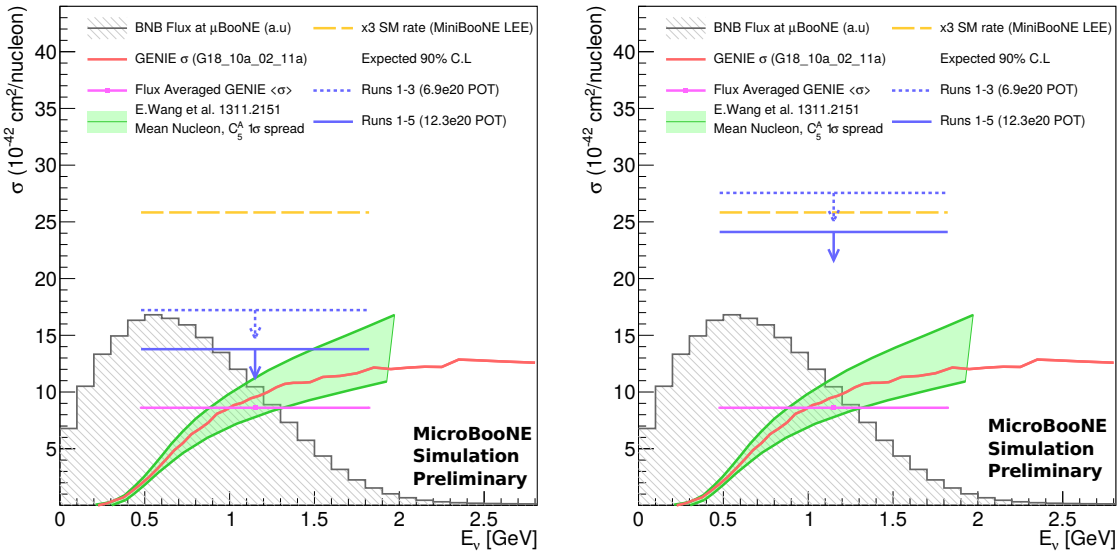

Figure 62: *The expected classical 90% confidence intervals assuming observation of data consistent with no Δ radiative decay ($\hat{x}_\Delta = 0$, left) and consistent with the GENIE CV prediction ($\hat{x}_\Delta = 1$, right). The GENIE v3 cross-section prediction is shown in red, alongside a leading theoretical calculation of the full single photon emission rate on argon in green [23], showing excellent agreement with GENIE. The all-flavor BNB neutrino flux is shown as the hashed gray histogram, as well as the total flux averaged GENIE cross section as the single point in magenta. The width of the horizontal errors bars represents 68% of the flux-times-cross-section distribution. The bound is placed on this flux-averaged cross section as, due to the neutral current nature of the process, we are not sensitive to parent neutrino energy at the level required to extract an energy dependent cross-section. Highlighted in yellow is the 3× the flux-averaged GENIE cross-section—the approximate enhancement to the Δ radiative decay rate in order for it to be the sole explanation of the MiniBooNE LEE. The NC π^0 rate is kept at the GENIE CV prediction.*

7 Summary and Conclusions

We have presented the MicroBooNE search for excess neutrino-induced NC single-photon events, which has been optimized specifically for a signal topology consistent with NC Δ resonance production followed by Δ radiative decay. This search is being carried out by MicroBooNE in order to directly constrain the SM-predicted rate of the neutrino-induced NC $\Delta \to N\gamma$ process on argon, at neutrino energies below 1 GeV, as well as to directly test the NC Δ radiative decay interpretation of the previously observed and still unexplained MiniBooNE "low energy excess".

Through four exclusive, targeted single-photon and NC π^0 selections, the MicroBooNE single-photon analysis is projected to yield world-leading constraints to the SM-predicted NC $\Delta \to N\gamma$ cross section on argon, as shown in Fig. 62. It is also projected to provide a 2.1σ (statistical and systematics) test of the interpretation of the observed MiniBooNE low energy excess as an underestimate of NC single-photon production that is generally consistent with the NC $\Delta \to N\gamma$ signature; this projected sensitivity is the

median significance of rejecting the low energy excess hypothesis in favor of the SM hypothesis, assuming the SM is true, for Runs 1-5.

At the same time, the analysis has produced the world's highest-statistics measurement of NC π^0 interactions on argon in the exclusive $2\gamma 1p$ and $2\gamma 0p$ final state topologies. This is allowing information that is relevant to the single-photon search to be meaningfully extracted, such as corrections to the GENIE-predicted coherent and non-coherent NC π^0 event rates.

The analysis demonstrates the challenge of low-energy shower reconstruction in LArTPCs, but at the same time highlights the wealth of topological and calorimetric information that can be successfully extracted from recorded LArTPC data. Preliminary data to Monte Carlo comparisons with statistics-limited and blinded 1γ data sets show reasonable data to Monte Carlo agreement, within fully assessed systematic uncertainties, including flux, cross-section, and detector systematics.

Further improvements to the MicroBooNE single-photon low energy excess search are possible with (ongoing) improvements in reconstruction, which are needed in order to enhance signal efficiency at the topological selection stage. Inclusion of information recorded by MicroBooNE's cosmic ray tagger (CRT), a veto detector enveloping the MicroBooNE LArTPC that was intended to provide further rejection of detector-crossing cosmic ray muons and brought online at the end of Run 2, may also be considered to provide further cosmic rejection while preserving signal efficiency.

References

[1] A. A. Aguilar-Arevalo *et al.*, "Unexplained Excess of Electron-Like Events From a 1-GeV Neutrino Beam," *Phys. Rev. Lett.*, vol. 102, p. 101802, 2009.

[2] K. Abe *et al.*, "Search for neutral-current induced single photon production at the ND280 near detector in T2K," *J. Phys.*, vol. G46, no. 8, p. 08LT01, 2019.

[3] M. Collaboration, "MicroBooNE low-energy excess signal prediction from unfolding," *MicroBooNE Public Note 1043.*

[4] G. S. Karagiorgi, *Searches for New Physics at MiniBooNE: Sterile Neutrinos and Mixing Freedom.* PhD thesis, 2010.

[5] R. Acciarri *et al.*, "Design and Construction of the MicroBooNE Detector," *JINST*, vol. 12, no. 02, p. P02017, 2017.

[6] J. Conrad, B. Jones, Z. Moss, T. Strauss, and M. Toups, "The Photomultiplier Tube Calibration System of the MicroBooNE Experiment," *JINST*, vol. 10, no. 06, p. T06001, 2015.

[7] R. Acciarri *et al.*, "Noise Characterization and Filtering in the MicroBooNE Liquid Argon TPC," *JINST*, vol. 12, no. 08, p. P08003, 2017.

[8] M. Collaboration, "The microboone search for single photon events," *MicroBooNE Public Note 1041.*

[9] R. G. Murrells, *The Search for Low Energy Single Photons in MicroBooNE.* PhD thesis.

[10] R. Acciarri, C. Adams, R. An, J. Anthony, J. Asaadi, M. Auger, L. Bagby, S. Balasubramanian, B. Baller, C. Barnes, *et al.*, "The pandora multi-algorithm approach to automated pattern recognition of cosmic-ray muon and neutrino events in the microboone detector," *The European Physical Journal C*, vol. 78, no. 1, p. 82, 2018.

[11] X. Ji, "Space charge boundary of position dependence." MicroBooNE DocDB: 26423, 2019.

[12] M. Collaboration, "Event selection in the microboone deep learning based low energy excess analysis using two-body scattering criteria," *MicroBooNE Public Note 1086.*

[13] M. Collaboration, "Search for electron neutrinos in multiple topologies with the microboone experiment," *MicroBooNE Public Note 1085.*

[14] N. Tagg, "Argo event display." "https://argo-microboone.fnal.gov/".

[15] C. Andreopoulos, "Genie physics & users manual v3 prelim." https://genie-docdb.pp.rl.ac.uk/DocDB/0000/000002/006/man.pdf, 2019.

[16] J. Zennamo and Z. Pavlovic, "Microboone flux and flux uncertainties." MicroBooNE DocDB: 8622, 2017.

[17] M. H. Shaevitz, "Constraining the ν_e background uncertainties with the observed ν_μ events." BooNE Technical Note: 221, 2007.

[18] M. S. W. Group, "Mcc9 detector systematic uncertainties." MicroBooNE DocDB: 27009, 2020.

[19] L. Yates, "Detector systematics with waveform modification." MicroBooNE DocDB: 26195, 2019.

[20] X. Ji, W. Gu, X. Qian, H. Wei, and C. Zhang, "Combined Neyman–Pearson chi-square: An improved approximation to the Poisson-likelihood chi-square," *Nucl. Instrum. Meth. A*, vol. 961, p. 163677, 2020.

[21] A. Aguilar-Arevalo, C. Anderson, S. Brice, B. Brown, L. Bugel, J. Conrad, R. Dharmapalan, Z. Djurcic, B. Fleming, R. Ford, *et al.*, "Event excess in the miniboone search for $\nu_\mu \to \nu_e$ oscillations," *Physical Review Letters*, vol. 105, no. 18, p. 181801, 2010.

[22] G. J. Feldman and R. D. Cousins, "A Unified approach to the classical statistical analysis of small signals," *Phys. Rev. D*, vol. 57, pp. 3873–3889, 1998.

[23] E. Wang, L. Alvarez-Ruso, and J. Nieves, "Photon emission in neutral current interactions at intermediate energies," *Phys. Rev. C*, vol. 89, no. 1, p. 015503, 2014.

A Appendix I: GENIE Cross section Systematics

Variation Label	Description
All_UBGenie	All multisim mode GENIE variables combined
AGKYpT1pi_UBGenie	Pion transverse momentum for Nπ states in AGKY
AGKYxF1pi_UBGenie	Pion Feynman x for Nπ states in AGKY
AhtBY_UBGenie	A_HT higher twist param in BY model scaling variable ξ_w $\pm$25 %
BhtBY_UBGenie	B_HT higher twist param in BY model scaling variable ξ_w
CV1uBY_UBGenie	C_V1u u valence GRV98 PDF correction param in BY model
CV2uBY_UBGenie	C_V2u u valence GRV98 PDF correction param in BY model
CoulombCCQE_UBGenie	Changes angular distribution of nucleon cluster
EtaNCEL_UBGenie	Strange axial form factor η for NC elastic
FrAbs_N_UBGenie	Nucleon absorption probability.
FrAbs_pi_UBGenie	pi absorption probability
FrCEx_N_UBGenie	Fractional cross section for nucleon charge exchange
FrCEx_pi_UBGenie	Fractional cross section for π charge exchange
FrInel_N_UBGenie	Nucleon charge exchange probability
FrInel_pi_UBGenie	π charge exchange probability
FracDelta_CCMEC_UBGenie	Nucleon pi-minus production probability
FracPN_CCMEC_UBGenie	π-production probability
MFP_N_UBGenie	Nucleon mean free path (total rescattering probability)
MFP_pi_UBGenie	π mean free path (total rescattering probability)
MaCCQE_UBGenie	Axial Mass for CCQE
MaCCRES_UBGenie	Axial mass for CC resoce neutrino production
MaNCEL_UBGenie	Axial mass for NC elastic
MaNCRES_UBGenie	Axial mass for NC resoce neutrino production
MvCCRES_UBGenie	Vector mass for CC resoce neutrino production
MvNCRES_UBGenie	Vector mass for NC resoce neutrino production
NonRESBGvbarnCC1pi_UBGenie	Non-Res background normalization $\bar{\nu}$ neutron $CC1\pi$ scattering
NonRESBGvbarnCC2pi_UBGenie	Non-Res background normalization $\bar{\nu}$ neutron $CC2\pi$ scattering
NonRESBGvbarnNC1pi_UBGenie	Non-Res background normalization $\bar{\nu}$ neutron $NC1\pi$ scattering
NonRESBGvbarnNC2pi_UBGenie	Non-Res background normalization $\bar{\nu}$ neutron $NC2\pi$ scattering
NonRESBGvbarpCC1pi_UBGenie	Non-Res background normalization $\bar{\nu}$ proton $CC1\pi$ scattering
NonRESBGvbarpCC2pi_UBGenie	Non-Res background normalization $\bar{\nu}$ proton $CC2\pi$ scattering
NonRESBGvbarpNC1pi_UBGenie	Non-Res background normalization $\bar{\nu}$ proton $NC1\pi$ scattering
NonRESBGvbarpNC2pi_UBGenie	Non-Res background normalization $\bar{\nu}$ proton $NC2\pi$ scattering
NonRESBGvnCC1pi_UBGenie	Non-Res background normalization ν neutron $CC1\pi$ scattering
NonRESBGvnCC2pi_UBGenie	Non-Res background normalization ν neutron $CC2\pi$ scattering
NonRESBGvnNC1pi_UBGenie	Non-Res background normalization ν neutron $NC1\pi$ scattering
NonRESBGvnNC2pi_UBGenie	Non-Res background normalization ν neutron $NC2\pi$ scattering
NonRESBGvpCC1pi_UBGenie	Non-Res background normalization ν proton $CC1\pi$ scattering
NonRESBGvpCC2pi_UBGenie	Non-Res background normalization ν proton $CC2\pi$ scattering
NonRESBGvpNC1pi_UBGenie	Non-Res background normalization ν proton $NC1\pi$ scattering
NonRESBGvpNC2pi_UBGenie	Non-Res background normalization ν proton $NC2\pi$ scattering
Min/Max Mode	Variations
NormCCCOH_UBGenie	Normilization for CC Coherent Processes (in developement)
NormNCCOH_UBGenie	Normilization for NC Coherent Processes (in developement)
RPA_CCQE_UBGenie	Strength of RPA correction for central tune
Theta_Delta2Npi_UBGenie	Variation of angle of pion with respect to detector z axis
TunedCentralValue_UBGenie	Tunes CCQE model based on central value MC
VecFFCCQEshape_UBGenie	VecFFCCQEshape UBGenie
DecayAngMEC_UBGenie	Changes angular distribution of nucleon cluster
AxFFCCQEshape_UBGenie	Varies CCQE axial form factor model between dipole (CV) and z-expansion.

Table 15: *Description of GENIE cross-section reweightable systematics. Note that Min/Max variations are not included in Genie_ALL*